# AFM manipulation of damping in nanomechanical resonators

Dissertation der Fakultät für Physik der
Ludwig-Maximilians-Universität München

vorgelegt von
Johannes Rieger
geboren in Garmisch-Partenkirchen

München, Juni 2013

Erstgutachter: Prof. Jörg Kotthaus
Zweitgutachter: Prof. Hermann Gaub
Tag der mündlichen Prüfung: 17. Juli 2013

# Zusammenfassung

Ein bedeutender Teilbereich der Nanomechanik beschäftigt sich mit der Erforschung kleiner, schwingender Systeme, welche aufgrund ihrer geringen Massen auf minimale Umgebungseinflüsse reagieren. Dies macht derartige nanoskalige Resonatoren zu äußerst empfindlichen Sensoren. Die fortschreitende Miniaturisierung nanomechanischer Systeme erfordert nun einerseits die Weiterentwicklung von Antriebs- und Detektionsmechanismen, andererseits spielt die Verbesserung der mechanischen Güte eine zentrale Rolle für die Erhöhung der Empfindlichkeit möglicher sensorischer Anwendungen. Hierfür ist die Untersuchung der Mechanismen, welche die mechanische Dämpfung der Resonatoren verursachen, erforderlich.

Um das Dämpfungsverhalten eines beidseitig eingespannten nanomechanischen Siliziumnitridresonators zu untersuchen und zu kontrollieren wird in dieser Arbeit ein Rasterkraftmikroskop (AFM) eingesetzt. Dessen Spitze wird mit dem Resonator in Kontakt gebracht und beeinflusst als lokale Störung kontrolliert das nanomechanische System. Das AFM bildet hierbei einen mechanischen Punktkontakt mit der Aufhängung des Resonators aus, wodurch Schwingungsenergie vom Resonator in die AFM-Spitze abgeleitet wird. Aufgrund der hervorragenden räumlichen Auflösung des Rasterkraftmikroskops ist es somit möglich den ortsaufgelösten Energiefluss zwischen den beiden Systemen zu untersuchen. Hierfür wird die mechanische Resonanz der Siliziumnitridsaite im Radiofrequenzbereich mittels eines heterodynen Überlagerungsverfahrens elektrisch ausgelesen. Die Bewegung des zwischen zwei Goldelektroden platzierten Resonators ruft eine Kapazitätsänderung des durch die Elektroden gebildeten Kondensators hervor. Durch Kopplung an einen Mikrowellenschwingkreis kann diese Kapazitätsänderung ausgelesen werden. Zudem können Gleich- und Wechselspannungen an die Elektroden angelegt werden, wodurch einerseits die Resonanzfrequenz des Resonators verstimmt und andererseits die mechanische Bewegung angetrieben werden kann.

Das derart angetriebene nanomechanische System kann nun unter Einfluss der lokalen Störung durch das AFM in positions- und kraftabhängigen Messungen untersucht werden. Es zeigt sich, dass der Energietransfer durch den mechanischen Punktkontakt einen äußerst starken Einfluss auf die mechanische Güte des Siliziumnitridbalkens hat, seine Resonanzfrequenz jedoch nur geringfügig beeinflusst wird. Dies kann durch eine Änderung der mechanischen Impedanzanpassung des Resonators an seine Umgebung erklärt werden. Die Impedanzänderung durch den mechanischen Punktkontakt ermöglicht den Übergang eines stark fehlangepassten nanomechanischen Systems hoher Güte zu einem angepassten System niedriger Güte auf einem einzigen Resonator. Hierbei bleibt die intrinsische Dämpfung des Resonators unverändert und die zusätzlich induzierte Dämpfung kann der Abstrahlung von Vibrationsenergie in die Umgebung zugeschrieben werden. Resonatoren hoher Güte ergeben sich somit als Systeme mit möglichst großer Fehlanpassung der mechanischen Impedanz.

Desweiteren kann mit dieser Methode das in den Aufhängepunkt des Resonators hineinreichende Verzerrungsfeld abgebildet werden. Dies ermöglicht die Untersuchung gekoppelter Moden des Resonators sowie deren Modenform.

# Contents

**Zusammenfassung** **iii**

**1 Introduction** **1**

**2 Experimental setup** **5**
2.1 The atomic force microscope (AFM) . . . . . 5
2.1.1 Working principle . . . . . 5
2.1.2 Constant force mode . . . . . 6
2.1.3 Force distance curves . . . . . 10
2.1.4 Vibration isolation, vacuum, and microwave cabling . . . . . 12
2.2 High-Q silicon nitride string resonators . . . . . 15
2.2.1 Constant force measurements on silicon nitride nanostrings . . . . 16
2.2.2 Sample fabrication . . . . . 18
2.3 Transduction scheme . . . . . 19
2.3.1 Motivation - state of the art transduction . . . . . 19
2.3.2 Sample geometries . . . . . 20
2.3.3 Frequency tuning . . . . . 22
2.3.4 Dielectric damping . . . . . 25
2.4 Electrical setup and devices . . . . . 27

**3 Nanoscale mechanical impedance mismatch imaging by contact mode AFM** **31**
3.1 Local probe measurements . . . . . 32
3.2 Theoretical modeling of the mechanical impedance . . . . . 35
3.2.1 Assumptions . . . . . 35
3.2.2 General considerations and linearity . . . . . 35
3.2.3 Mechanical impedance . . . . . 37
3.2.4 Interpretation in terms of mechanical impedance matching . . . . 41
3.2.5 Linear model for deflection perpendicular to the surface . . . . . 42
3.2.6 Tip-surface interaction . . . . . 45
3.3 Force dependent measurements . . . . . 47
3.4 Position-dependent impedance mismatch . . . . . 49
3.5 Impedance mismatch and dissipation in nanomechanical systems . . . . . 52

**4 Coupled systems and AFM manipulation** **55**
4.1 Coupling of in- and out-of-plane modes . . . . . 55
4.2 AFM visualization of the mode polarization . . . . . 62
4.3 Nonadiabatic dynamics of the coupled modes . . . . . 64

**5 Conclusion and outlook** **69**

**A Employed cantilevers** **73**

**B Sample fabrication** **75**

**C Modeling of the avoided crossing with mathematica** **77**

**Bibliography** **85**

**List of Publications** **93**

**Vielen Dank** **95**

# Chapter 1

# Introduction

Shortly after the Nobel prize winning invention of the scanning tunneling microscope [Bin82], which enabled imaging of conducting surfaces with atomic resolution, its designers used this very device to construct another type of scanning probe microscope capable of imaging insulating surfaces - the atomic force microscope (AFM) [Bin86]. Since that time, AFMs have become a ubiquitous research tool in surface sciences [Gie03] and biology [Ale05]. Subatomic resolution imaging of insulating surfaces has been demonstrated [Gie95, Hug01]. Further, new operation modes have been developed for AFMs, increasing both their resolution and their imaging speed [Sul02, Gie03], as well as acquiring information from the subsurface [Tet10]. Aside from its imaging capabilities, the AFM is a powerful spectroscopic tool [Cap99] which, for example, allows measurement of the strength of covalent bonds [Gra99]. Apart from force measurements, the AFM has been employed as a sensitive detector of mechanical motion with GHz frequencies [Gar07], as a local perturbation in electron transport measurements [Top00] and as a tool for investigating self assembled quantum dots [Ben10].

Alongside these achievements, the development of ever more performant cantilever designs for resonant measurements has led to a cross-fertilization with the field of micro- and nanoelectromechanical systems (M/NEMS) [Cra00, Li07]. M/NEMS systems have proven to be technologically viable in applications such as frequency filtering in cell phones [Bou05] and gyroscopes [Dea09], and have shown great promise for next-generation sensor applications such as mass sensors [Nai09, Li10, Cha12b], resonant bio sensors [Bur07] and ultrasensitive force sensors [Mam01, Reg08].

In fundamental research, the long-sought goal of cooling a mechanical resonator mode to its quantum ground state has recently been achieved [O'C10, Teu11, Cha11] with NEMS devices. These results show great promise for testing quantum theories with macroscopic objects and creating entangled mechanical states [Jos09] for quantum processing.

For all these applications, three areas of development are central to realizing the potential of high performance resonant nanomechanical devices. These are the advancement of resonator geometries and materials exhibiting low mechanical losses; improved readout

schemes of the mechanical oscillations, with an emphasis on compactness and integrability; and increased control of the resonant behavior of the mechanics.

The so-called Q factor (also referred to as quality factor) is the most commonly considered figure of merit in linear, resonating systems and is given as the ratio of the energy stored in the system to the energy dissipated per oscillation, a high Q factor being thus related to small mechanical damping. But that is not the whole story. Resonators fabricated from prestressed silicon nitride thin films have been found to exhibit unusually high mechanical Q factors [Ver06]. A recent study has shown that these high quality factors are a consequence of the increased stored mechanical energy in the system due to the inherent tensile stress, rather than a decrease in damping [Unt10a]. By the reasoning presented in that work, the dominant source of damping is internal friction that can be phenomenologically understood within a Zener model [Zen38]. Another source of damping in nanomechanical systems are so-called clamping losses [WR08]. Here a phonon residing on the resonator is converted into a propagating substrate phonon of equal frequency, which is modeled in the phonon tunneling approach [WR08, Col11].

To gain more insight into the damping behavior of silicon nitride string resonators, this project uses an AFM as a controlled, local, mechanical perturbation of the system. As such, the experiment follows the work presented in ref. [Top00], where an AFM was used in a conceptionally similar way employing an AFM tip as a local perturbation to image the flow of coherent electrons through an electrical quantum point contact. In the present work, the AFM is used to create a mechanical point contact with the support of a vibrating high-Q silicon nitride nanostring, allowing control of the flow of vibrational energy from the resonator into the tip. This approach combines the excellent local resolution of the AFM with the high quality factor of the nanostring to investigate the spatially resolved energy flow between the two systems. To this end, the energy stored in the nanomechanical resonator must be independently probed to quantify the induced energy loss. This is achieved with a transduction scheme that efficiently drives and reads out the nanomechanical motion [Rie12]. It combines a heterodyne microwave cavity-enhanced detection scheme [Fau12a] with a dielectric driving technique [Unt09].

In order to realize nanomechanical measurements with simultaneous AFM manipulation of the system, certain experimental requirements have to be fulfilled. First of all, it is necessary to work in vacuum, since the employed silicon nitride string resonators incur strong viscous damping under ambient conditions [Vig06, Ver08], which reduces the quality factor by orders of magnitude. Secondly, using the microwave detection scheme requires a specialized sample holder as well as cabling. Chapter 2 describes the employed atomic force microscope, as well as the adaptations necessary to investigate nanomechanical resonators with this instrument. The employed transduction scheme is subsequently described in detail. Special emphasis is placed on the fact that the combination of microwave detection and dielectric drive ultimately enables tuning of both the resonance frequency and quality factor of the nanomechanical resonance through the application of a dc voltage. Chapter 2 closes with a description of the automation processes necessary for the AFM measurements.

Position- and force-dependent AFM measurements are presented in Chapter 3. The vibrational modes of the nanoresonator are modeled as localized standing waves caused by the mismatch in mechanical impedance between the support and the suspended region of the string. A large impedance mismatch gives rise to a large wave reflection at the interface and, correspondingly, a highly localized mode with a large Q factor. In the experiments presented here, the AFM tip locally perturbs the flexural modes of the resonator in its clamping region, where the minute oscillation-induced surface deformations allow a transfer of vibrational energy to the AFM cantilever. This energy transfer is investigated by changing the contact position of the AFM tip in constant force mode, or by varying the applied force at a given position. Thus the mechanical impedance mismatch of the resonator to the environment is altered by the action of the AFM tip, and the passage between a highly mismatched, high-Q system to a highly matched, low-Q system can be observed on a single resonator. While this method does not address all relevant intrinsic sources of damping [Lif00, Unt10a, Rem12] it allows local investigation of the contribution coming from vibrational modes radiating into the supports [Cro01, WR08]. To close this section, a theoretical model which was specifically developed by Andreas Isacsson from Chalmers University of Technology in Gothenburg in a collaborative effort is presented and used to fit and analyze the data.

In chapter 4, the here established AFM measurement technique is used to investigate coupled modes of the nanomechanical resonator. These are composed of the fundamental flexural out-of-plane and in-plane modes, i.e. orthogonal modes with oscillation directions perpendicular and parallel to the substrate. With proper electrode design, these modes can be voltage tuned into resonance and a pronounced avoided crossing can be observed [Fau12c]. Chapter 4 starts with a description of the electric field mediated coupling mechanism and a calculation of the mode shapes with experimentally obtained parameters. At the zero detuning point, these mode shapes are diagonal hybrid modes comprised of the in-phase and out-of-phase combinations of the in-plane and out-of-plane mode. This leads to a modified local amplitude in the clamping region of the resonator, which can be mapped out in position-dependent AFM measurements. Lastly, when tuning through the avoided crossing with different tuning speeds, Landau-Zener transitions between the two modes can be observed. These transitions agree very well with a classical theoretical model [Nov10, Fau12c].

A final summary concludes the thesis and an outlook on possible successive measurements is provided.

# Chapter 2

# Experimental setup

## 2.1 The atomic force microscope (AFM)

In order to employ an AFM as a local perturbation of a nanomechanical system certain requirements have to be fulfilled. First of all, it is an absolute necessity to work in vacuum, as the used silicon nitride string resonators are subject to strong viscous damping under ambient conditions [Vig06, Ver08], which reduces the quality factor by orders of magnitude. Secondly, using the microwave cavity enhanced detection scheme that will be explained in detail in chapter 2.3 requires a special microwave sample holder as well as cabling. The following chapter thus describes the employed *attoAFM I* atomic force microscope as well as the modifications that have been made to adapt the system to the specific needs of investigating a nanomechanical resonator in this instrument.

### 2.1.1 Working principle

Two major aspects are essential for designing an AFM. These are precise sample positioning and sensitive read-out of the cantilever deflection. In the *attoAFM I* manufactured by *attocube* which is used here, the cantilever is laterally fixed and the sample is attached to a movable positioning unit, which is subdivided into a coarse xyz-positioner and a piezo scanner that is employed during the actual AFM operation (cf. Fig. 2.1). The coarse positioner allows to adjust the sample position over a range of several millimeters, the scanner unit has a continuos range of $34\times34\,\mu m^2$ in x- and y-direction and a range of $11\,\mu m$ in z-direction.

The cantilever deflection is detected with a fiber interferometric technique [Rug88, Gra00] as depicted in Fig. 2.1b. The light of a 1300 nm diode laser is sent through an optical single mode fiber and gets reflected both at the cleaved fiber end and from the cantilever surface, which thereby form an unbalanced Fabry-Pérot cavity, i.e. a cavity with low finesse. The reflected light is then sent through a fiber coupler and detected with a photodiode.

As the Fresnel reflectivity $R_1$ of the glass-air boundary is only about 4 %, it is sufficient to consider only first order reflections for the field amplitudes. At the fiber end this gives $E_{\mathrm{fib}} = E_0\, r_1$, with $r_1 = \sqrt{R_1}$ and the reflection from the cantilever surface leads to $E_{\mathrm{cant}} = E_0\,(1-r_1)^2\, r_2\, e^{2ikd}$ with $r_2 = \sqrt{R_2}$, the wave vector $k = \frac{2\pi}{\lambda}$ and a phase difference $\phi = 2kd$ between the reflected beams. The photodetector voltage is proportional to the reflected intensity, which is given by the magnitude $|E_{\mathrm{fib}} + E_{\mathrm{cant}}|^2$. The dependence of the intensity on cavity length $d$ is thus given by

$$I = I_0 \left( R_1 + (1 - R_1)^2 R_2 + 2(1 - R_1)\sqrt{R_1 R_2}\cos(2kd) \right). \tag{2.1}$$

This sinusoidal interference pattern is observed when tuning the cavity length via the voltage applied to the piezo that supports the cantilever, as shown in Fig. 2.1c. As the fringes exhibit a periodicity of half a wavelength, the photodetector signal can be readily converted into cantilever displacement. To this end it is convenient to rewrite equation 2.1 in terms of photodetector voltage:

$$U(z) = U_0 \sin(2kz) + U_{\mathrm{off}} \tag{2.2}$$

Where $U_0$ is the peak to peak amplitude of the interference signal, $U_{\mathrm{off}}$ an offset voltage and $z$ the cantilever deflection. Taking the maximum of the derivative of equation 2.2 with respect to $z$ and using $k = \frac{2\pi}{\lambda}$ one obtains, after inverting:

$$\left.\frac{dz}{dU}\right|_{\max} = \frac{\lambda}{2\pi}\frac{1}{U_0} \tag{2.3}$$

With a laser wavelength of $1300$ nm and a typical value for $U_0$ of $4$ V, the displacement per voltage is about $50$ nm/V. Below it is shown that this corresponds to a displacement sensitivity of $0.75\,\mathrm{pm/Hz^{-1/2}}$.

### 2.1.2 Constant force mode

There are numerous modes of AFM operation that can generally be divided into static and dynamic modes [Gie03]. In the static mode, the force $F$ causes a deflection $d$ of the cantilever which is inversely proportional to its spring constant $k_{\mathrm{ca}}$: $d = F/k_{\mathrm{ca}}$. In the dynamic operation modes, the driven cantilever oscillation is monitored and changes in oscillation amplitude or phase allow conclusions on elastic and inelastic interactions of the AFM tip with the sample surface. In most applications this is used to acquire an image of the sample topography. There are however various techniques that allow nanoscale imaging of different properties such as the magnetic structure of a sample surface in magnetic force microscopy [Har99], or the experimental characterization of dissipative tip sample forces in non-contact AFM operation [Gau99].

The instrument employed in this work can principally be operated in both modes, dynamic and static, but in the measurements presented in chapter 3 and chapter 4, only

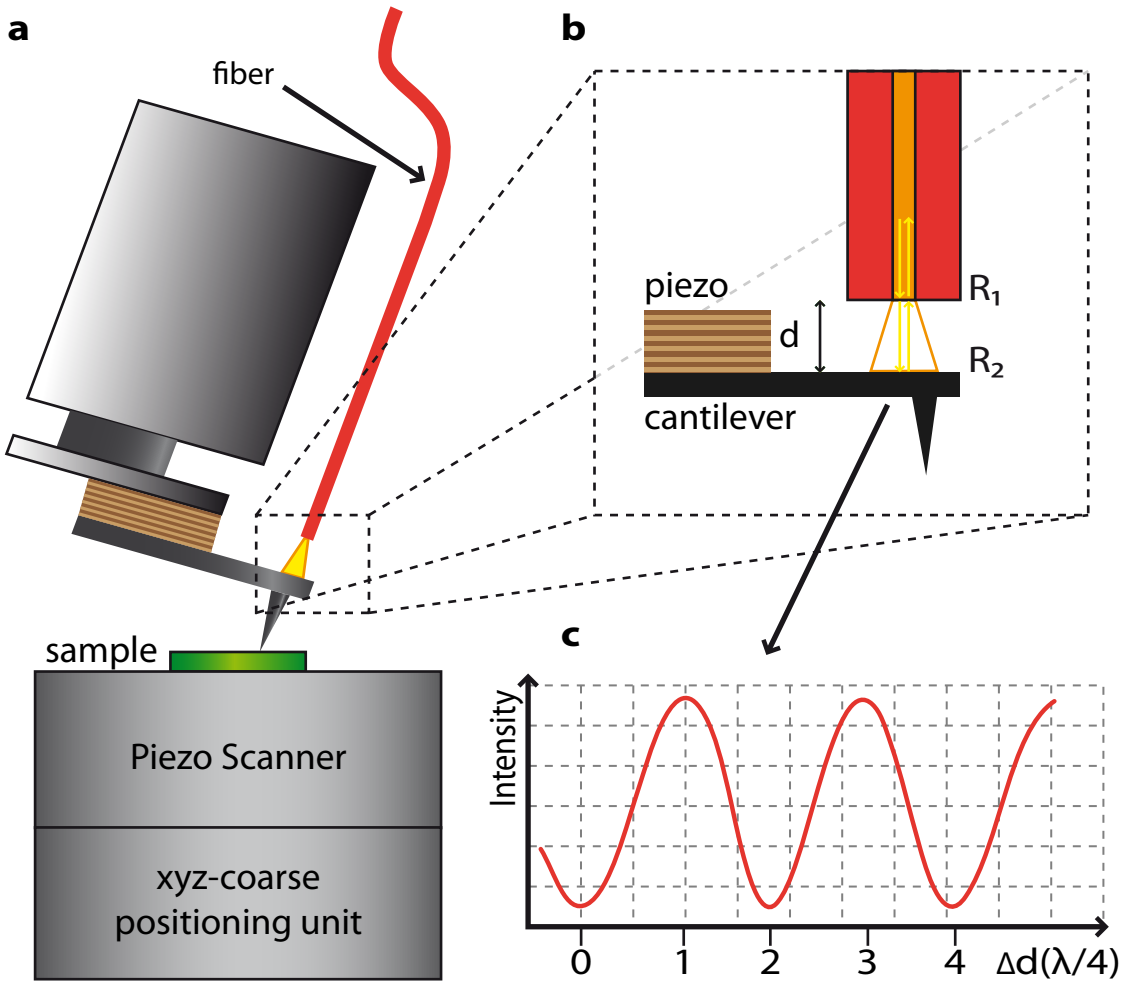


**Figure 2.1:** AFM working principle. **a** Schematic of the cantilever holder with optical fiber, the coarse positioning unit, the piezo scanner and the sample. **b** Illustration of the interferometric detection technique. Laser light gets reflected at the fiber end and at the cantilever surface, leading to a phase difference depending on the distance d. Tuning the voltage applied to the piezo holding the cantilever changes the distance d. Thus one can observe the interference fringes depicted in **c**.

the static constant force mode is used. Therefore, this mode of operation as well as all calibrations that are required to utilize it are described in more detail in the following.

In the constant force mode, as the name already suggests, the AFM is operated with the tip exerting a constant force on the sample surface. To this end, the tip is brought into contact with the sample, and a feedback loop (a PI loop) is used to keep the cantilever deflection and thereby the force at a constant value by varying the voltage applied to the z-scanner. The error signal of the loop is the photodetector voltage difference to the set-point of the feedback loop. It can be chosen anywhere between two extrema of the cavity interference signal, depending on the desired force value, however, the feedback loop is most efficient at the point of maximum slope between two extrema. The actual measurement signal in this mode is the voltage applied to the z-scanner. To translate this into a height information, a calibration grid with steps of known height of 20 nm (Budget Sensors HS-20MG) was measured to find the conversion between height and piezo voltage. This calibration then allows to obtain quantitative data of the sample topography.

Since the samples that are measured here exhibit height conjugations of up to 400 nm, it is very important that the parameters of the feedback loop and the scan speed be well adjusted. To this end, a setpoint modulation is employed to find reasonable PI starting parameters. This modulation emulates a step pattern on the sample surface by abruptly changing the setpoint of the loop with an adjustable period. The parameters of the loop are then tuned such that the response to the sudden change becomes as step-like as possible - without overshooting. After that, the parameters are fine adjusted by slowly scanning the sample with the tip in contact. With the samples under investigation in this work, it has been found that the best results for constant force measurements are obtained by setting the loop time constant to a value that is slower than the starting value found by the set point modulation and using scan speeds of no more than 1 µm/s to account for the increased response time. A slower time constant is also of advantage in point by point measurements with constant force, as the loop will stay stable at points with large height corrugations where the response of cantilever deflection for a given z-scanner voltage change can be drastically different from flat sample regions. At such points, slower loop parameters prevent a feedback oscillation that can otherwise lead to increased tip wear or even the destruction of the sample.

Abrupt changes in the sample topography, i.e. steep features do not only require a very careful adjustment of the feedback parameters, but also lead to a convolution of the tip and the sample shape [Kel91]. This is illustrated in Fig. 2.2, where a sudden step in the imaged surface that can be considered as an infinitely sharp feature, appears broadened in the obtained contour as the tip is scanned over the sample surface. This effect is highly relevant for the measurements using nanomechanical resonators in chapter 3 and chapter 4. The nanomechanical string resonators are 270 nm wide, whereas their distance to the substrate is about 400 nm. The tips of the typically employed silicon AFM probes (Budget Sensors ContAl) exhibit a half cone angle of 25 degrees, so that the beam image is significantly broadened and can appear to be more than 600 nm in width. For a table of all employed cantilevers and their specifications see appendix A.

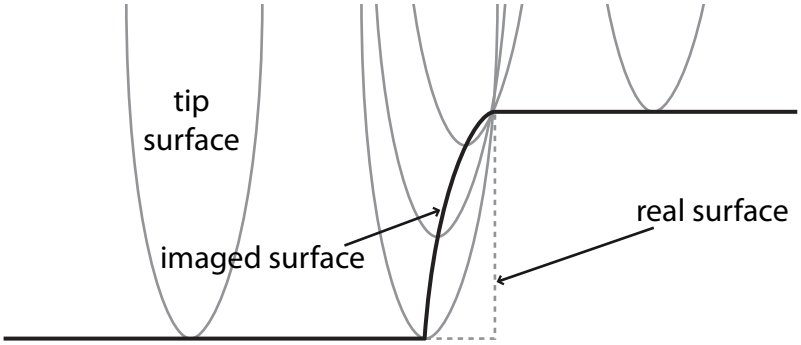


**Figure 2.2:** Illustration of the tip sample convolution. The infinitely sharp step that comprises the imaged feature appears distorted due to the shape of the tip surface (depicted in gray) as the tip is scanned over the sample, and the obtained contour (black, solid line) is broadened with respect to the real surface (gray dashed line).

A very important parameter for constant force measurements is of course the cantilever spring constant. In contact mode, the deflection of the cantilever should be large compared to the deformation of the tip and sample material. As the interatomic force constants in solids range from 10 N/m to about 100 N/m, a reasonable range of force constants for contact mode cantilevers is 0.01-5 N/m [Gie03]. There are numerous ways to calibrate the cantilever spring constant [Hut93, Bur03, Men06, Cli09] by either making use of the cantilever structure's static mechanical properties or investigating its resonant behavior. A convenient method in the employed AFM setup is a calibration via the Brownian motion of the cantilever [Gil96], i.e. the square of the thermal fluctuations in amplitude as a function of frequency. The squared amplitude $x^2$ per unit frequency $\nu$ is given by [Bur03]

$$\frac{x^2(\nu)}{\Delta\nu} = \frac{2k_{\mathrm{B}}T}{\pi\nu_0 Q k_{\mathrm{ca}}} \frac{1}{\left[1-(\frac{\nu}{\nu_0})^2\right]^2 + \left[\frac{\nu}{\nu_0 Q}\right]^2}, \tag{2.4}$$

where $k_{\mathrm{B}}$ is the Boltzmann constant, $T$ the temperature, $Q$ the quality factor, $\nu_0$ the resonance frequency of the fundamental cantilever mode and $k_{\mathrm{ca}}$ the cantilever spring constant. To measure a thermal spectrum, the cavity interference pattern is recorded and the deflection sensitivity is calculated using equation 2.3. Then the cantilever is placed at a point of maximum slope that is between two extrema of the cavity interference and a spectrum of the cantilever's thermal motion is recorded with a spectrum analyzer (Rohde & Schwarz FSP). Here the $\Delta\nu$ in equation 2.4 is the measurement bandwidth the spectrum analyzer is adjusted to. As the deflection per photodetector voltage is given in nm/V, the power spectrum is converted into a voltage spectrum. To this end, it is essential to use an input adapter (HP 41802A) between the spectrum analyzer input and the photodetector, as the spectrum analyzer is normally terminated with $50\,\Omega$, whereas the photodetector has a high impedance output. The adapter transforms the input impedance from the spectrum analyzer's $50\,\Omega$ to a value of $1\,\mathrm{M}\Omega$, and the conversion of power to voltage can still be done as usual for a $50\,\Omega$ system by using $P(\mathrm{W}) = \mathrm{U}^2/50\,\Omega$ for the Power $P$ in Watts.

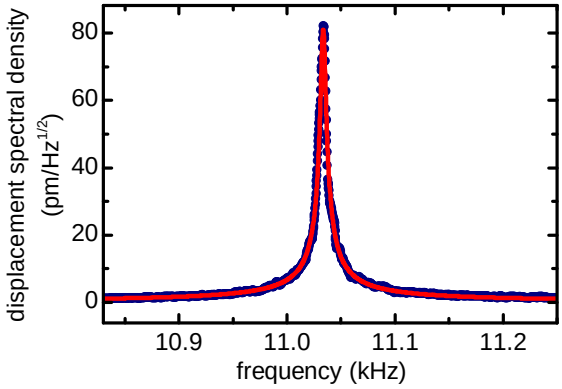


**Figure 2.3:** Frequency spectrum of the Brownian motion of a silicon cantilever (blue dots) with a resonance frequency of 11 kHz and a fit of the square root of equation 2.4 to the data (solid, red line), yielding a cantilever spring constant of 0.07 nN/nm.

This way, one obtains a voltage spectrum in $\mathrm{V/Hz^{-1/2}}$ that can be converted into a displacement spectrum by multiplying with the deflection per voltage given by equation 2.3. The measurement unit of this spectrum is $\mathrm{m/Hz^{-1/2}}$ and corresponds to the spectrum that is obtained by taking the square root of equation 2.4.

Fig. 2.3 shows such a spectrum of a silicon contact mode cantilever (Budget Sensors ContAl) with a fundamental resonance frequency of 11 kHz and a calibrated spring constant of 0.07 nN/nm in accordance with the values given by the manufacturer. The displacement sensitivity obtained from this measurement is $0.75\,\mathrm{pm/Hz^{-1/2}}$.

### 2.1.3 Force distance curves

For force dependent measurements, the sample is moved up and down with the z-scanner while monitoring the cantilever deflection as the tip is brought into contact with the sample and retracted thereafter [But05]. The resulting data are a measure of photodetector voltage versus the position of the z-scanner. A typical curve is plotted in Fig. 2.4a. The sample approaches the cantilever until the latter suddenly jumps into contact with the surface (red line in Fig. 2.4a) and then gets deflected as the sample is pushed further upwards. Then the sample is retracted again (black line in Fig. 2.4a) until the tip jumps out of contact. Note that the sinusoidal deflection signal in Fig. 2.4a is given by the cavity signal as described in chapter 2.1.1. The jump to contact occurs when the derivative of the tip-sample force is equal to the cantilever spring constant [Cap99] (red point marked as “to” in Fig. 2.4b). Conversely, the jump out of contact happens when this situation arises as the tip is retracted again (black point marked as “from” in Fig. 2.4b).

Generally, in a force-distance curve the z-displacement has to be converted into the true tip-sample distance [Cap99] due to long-range forces in the non-contact regime and after contact between tip and sample has been established, it is the indentation and the

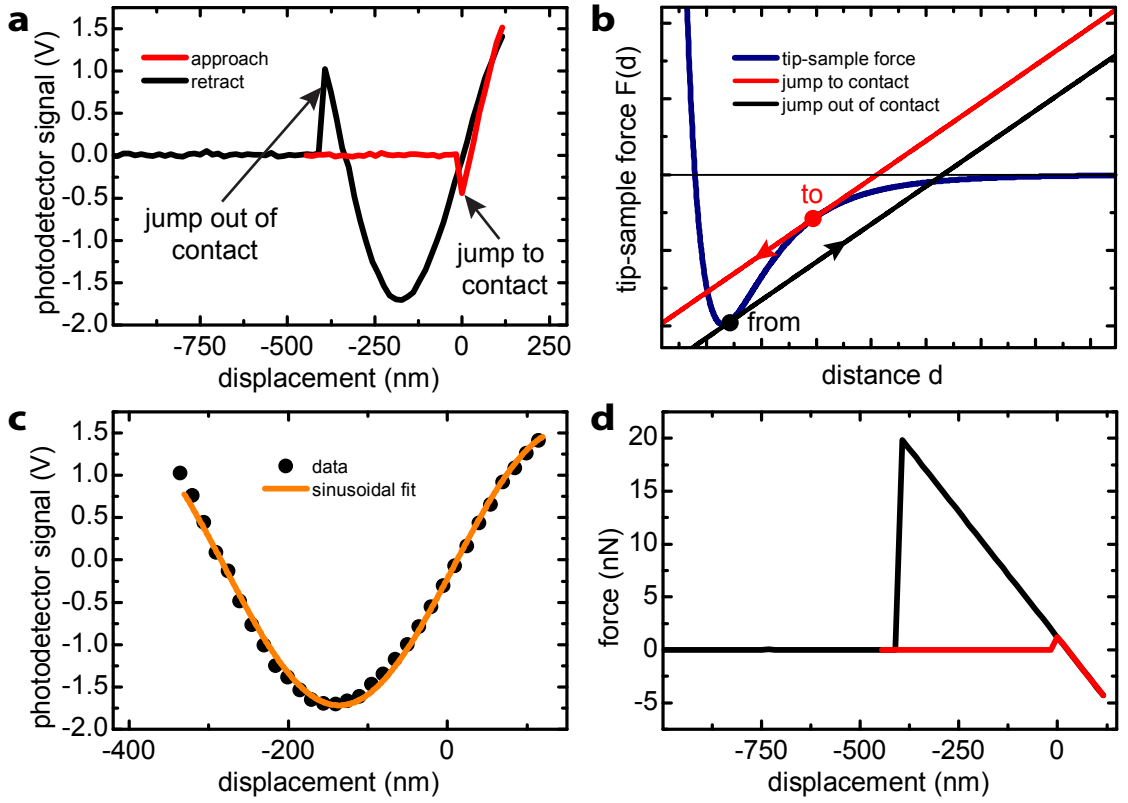


**Figure 2.4:** Force displacement curves and calibration. **a** Photodetector voltage versus displacement of the z-scanner. As the cantilever approaches the sample (red line), it jumps to contact and then gets deflected with z-scanner displacement. In the retraction part of the force displacement curve (black line), the sample is pulled back, until the tip jumps out of contact. The voltage has been normalized in such a way that zero voltage corresponds to zero cantilever deflection. **b** The jump to contact happens when the derivative of the tip-sample force equals the cantilever spring constant (red point marked as "to"). The same applies for the retraction, but at a different point (black, marked as "out"). **c** Sinusoidal fit of the cavity interference signal caused by the cantilever deflection to calibrate the displacement axis. **d** Resulting force displacement curve.

contact area that change with the applied load rather than the distance, which becomes nominally zero (of the order of an interatomic distance). In this work, the important parameter entering the theoretical modeling of the data presented in chapter 3 is the force when the tip is in contact with the sample surface. The true tip-sample distance, especially in the non-contact parts of the force-distance curves is therefore non-significant for the interpretation of the data presented later on and it is sufficient to calibrate the force-displacement curves for the contact part. Here, the tip-sample force $F$ is given by the cantilever deflection multiplied with the cantilever spring constant $F = -k_{\mathrm{ca}} Z_{\mathrm{ca}}$ and the cantilever deflection equals the z-piezo displacement $Z_{\mathrm{ca}} = Z_{\mathrm{piezo}}$. For this assumption to be correct, the cantilever deflection has to greatly exceed the indentation $\delta$ of the tip into the sample surface $Z_{\mathrm{ca}} \gg \delta$. Using Hertz theory [Her81] for $\delta$, one can estimate the indentation to be smaller than $50\,\mathrm{pm}$ for a silicon nitride surface, a silicon tip and a force of $20\,\mathrm{nN}$, whereas the cantilever deflection is of the order of hundreds of nanometers, so

that $Z_{\mathrm{ca}} \gg \delta$ is well justified. For more details on the force dependence of the indentation $\delta$ see chapter 3.

For a force displacement curve measurement, the fiber-cantilever cavity is adjusted such that the photodetector interference signal is at a point of maximum slope between two extrema (cf. equation 2.2). At this point, the cavity signal is linear in cantilever deflection, so that when the jump to contact occurs, the jump in force can be extracted from the cantilever deflection, using the known deflection per voltage given by equation 2.3. This gives the initial force in the contact regime. From this point on, one could in principle just multiply the piezo displacement with the cantilever spring constant to obtain the force values for the curve. To be more precise, and account for slight piezo nonlinearities (the jump to contact happens at different piezo dilatations, depending on the respective measurement and the response to the voltage applied to the piezo can be slightly different at different points), the retract part of the curve is used to fit the sinusoidal cavity interference signal and thereby calibrate the z-axis in every measurement. Note that this cavity interference signal in Fig. 2.4a is created by the cantilever deflection caused by the z-piezo pushing the sample upwards and thereby bending the cantilever, whereas the cavity signal in chapter 2.1.1 is recorded while varying the voltage applied to the piezo holding the cantilever, thereby displacing it. But as the deflection of a few hundreds of nanometers is reasonably small compared to the cantilever length of 450 µm, deflection and displacement are assumed to be equal. A sinusoidal fit of the cantilever deflection interference signal is displayed in Fig. 2.4c. The calibration of the z-axis, i.e. the displacement of the z-piezo and thus the cantilever deflection can then be carried out using equation 2.3 and the known laser wavelength. The z-axis is readjusted such that two adjacent maxima of the cavity signal have a distance of half a wavelength. Then the force values are obtained by multiplying the displacement with the cantilever spring constant (Fig. 2.4d).

### 2.1.4 Vibration isolation, vacuum, and microwave cabling

As a mechanical instrument, the atomic force microscope is very susceptible to environmental disturbances caused by acoustic, building, and vacuum pump vibrations. Hence it is necessary to isolate the system from these noise sources as well as possible. To passively decouple the AFM from building vibrations, the microscope is placed in a home built holder and suspended from the ceiling with bungee cords. The goal here is to attain a suspended system with a very low resonance frequency of below 1 Hz, with all higher frequency components being rejected. To achieve this, the load applied to the bungee cords has to be sufficient to elongate them by more than 25 cm. This can be understood by considering the frequency $2\pi f = \sqrt{k/m}$ of a mass on a spring, Hooke's law $k = F/\Delta l$ where $\Delta l$ is the elongation from the equilibrium position of the spring and the weight of the mass $m$ attached to the spring $F = mg$ with the acceleration of gravity $g$. Transforming these equations, one obtains the frequency that solely depends on the elongation $\Delta l$:

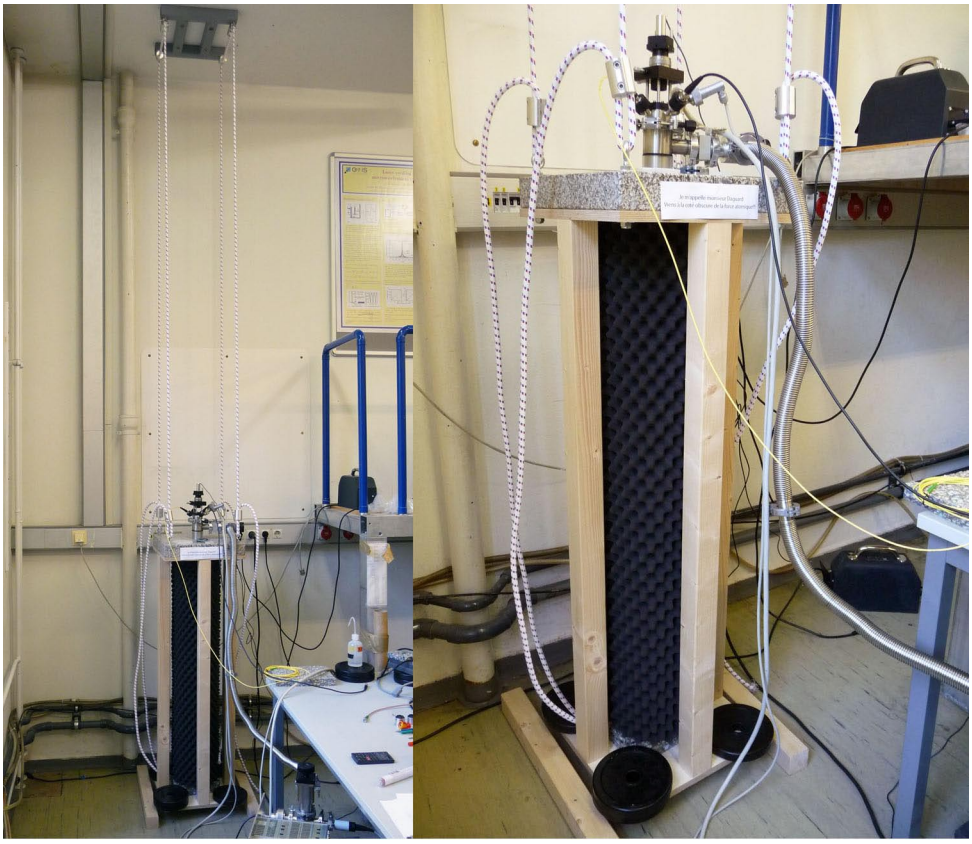

**Figure 2.5:** Left: The home built AFM holder is freely suspended with bungee cords that are attached to a metal frame of matched lateral dimensions (gray) on the ceiling. Right: Close-up of the AFM holder. It consists of a granite plate and a wooden framework that houses a plastic pipe (a polypropylene sewage pipe) which is lined and covered with foam, acting as the acoustic isolation of the instrument. The load of the holder can be varied with weight plates to tune the vibration frequency of the bungee chord system below 1 Hz. The microscope head protrudes from the granite plate and contains all necessary electrical vacuum feedthroughs, as well as vacuum flanges and the metal hose leading to the pump.

$$f = \frac{1}{2\pi}\sqrt{\frac{g}{\Delta l}} \tag{2.5}$$

Thus, a convenient way of adjusting a passive bungee cord vibration isolation is to apply a load such that the resulting elongation is larger than 25 cm, which corresponds to a frequency below 1 Hz.

A photograph of the employed holder is shown in Fig. 2.5. It consists of a granite plate atop a wooden framework that houses the actual instrument in a polypropylene sewage pipe which is lined and covered with foam, thereby working as an acoustic isolation. This isolation provides an acoustic damping of minimally 10 dB in the acoustic frequency range (40 Hz to 16 kHz), which was measured with a Shure SM58 vocal microphone, and the freeware Audacity using a white noise spectrum. The microscope is not entirely embedded in the holder, but protrudes from it to allow access to the electrical feedthroughs

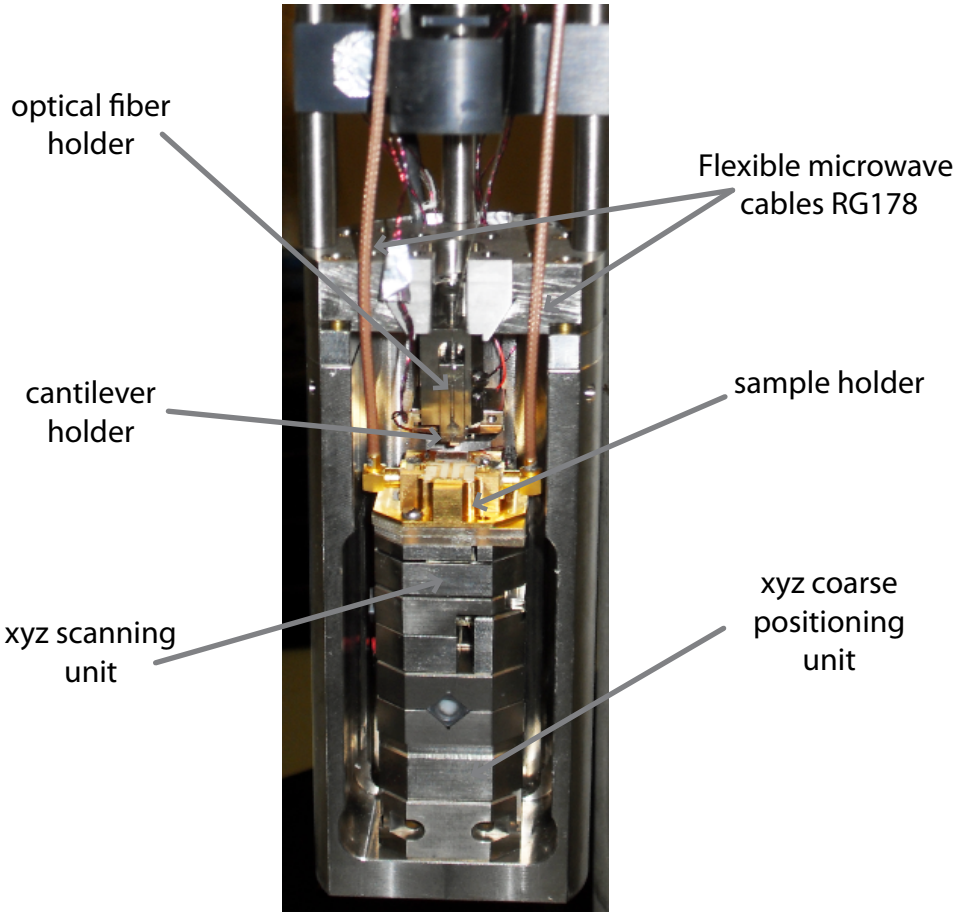


**Figure 2.6:** Photograph showing the fiber holder, the flexible part of the microwave cabling, the cantilever holder, the microwave sample holder as well as the positioning units.

at the microscope head, thus exposing a part of the instrument, where air-borne noise can be converted into structure-borne noise. To further improve the acoustic isolation one could therefore build another foam lined housing around the existing AFM holder, but as the acoustic noise has not proven itself to be a major issue in the measurements presented in the following chapters, the author refrained from doing so.

The vacuum pump setup consists of a turbomolecular pump with a rotary vane pump as the backing pump. This leads to another source of vibrational noise, namely the rocking motion of the vacuum setup (mainly caused by the rotary vane pump) that is transmitted to the instrument via the metallic vacuum hose. To dampen these vibrations, the hose is passed through a box filled with quartz sand. To decouple the hose from the wood that comprises the sandbox, it is fixed at the grommets with silicone.

Employing the presented passive vibration isolations it is possible to acquire very good AFM images under vacuum conditions with pressures below $10^{-4}$ mbar. Additionally, the AFM's active feedback loop has a low-pass characteristic, thus filtering out high frequency components of the vibrational noise spectrum.

A further modification of the AFM is its equipment with microwave cabling, to allow the utilization of a cavity enhanced heterodyne detection scheme to probe the nanomechanical motion. This scheme will be explained in detail in chapter 2.3. Three different kinds of cables are used to transmit the microwave signal from an SMA vacuum feedthrough to the sample holder. A hand-formable cable (Micro-Coax UT-85C-FORM) is used to connect the feedthrough to a semi rigid cable (Micro-Coax UT-85B-SS) via an SMA connector. The semi rigid cable leads to approximately 15 cm above the sample holder. From here, a flexible cable (RG-178/U) is used to transfer the microwave signal to the sample holder (Fig. 2.6) It is connected to the semi rigid cable with MMCX connectors. The flexibility of the cable is necessary, since the AFM positioning unit needs to be able to move the sample holder during AFM operation. The maximum load that may be applied in any direction is 1 N, so the length of the flexible cabling has to be adjusted very carefully, to ensure that only small forces are exerted on the positioning unit.

## 2.2 High-Q silicon nitride string resonators

The nanomechanical resonators employed in this work are taut silicon nitride string resonators [Ver06]. Because of the intrinsic tensile stress of the silicon nitride these resonators exhibit very high Q factors (quality factors) [Unt10a]. The Q factor is a dimensionless parameter used as a figure of merit for linear resonant systems and is defined by the ratio of the energy stored in the resonator to the dissipated energy per oscillation cycle as:

$$Q = 2\pi \frac{\text{Energy stored}}{\text{Energy dissipated per oscillation cycle}}. \tag{2.6}$$

For high Q factors, equation 2.6 can be expressed as the ratio of the resonator resonance frequency $\omega_0 = 2\pi f_0$ to the linewidth $\Delta\omega = 2\pi\Delta f$ of the resonance:

$$Q = \frac{\omega_0}{\Delta\omega} = \frac{f_0}{\Delta f}. \tag{2.7}$$

A high quality factor therefore means a sharp resonance. Thusly defined, for the free oscillation of a damped harmonic oscillator, the Q factor gives the number of oscillation cycles during a ringdown of the energy to a value of $1/\mathrm{e}$. Hence it has become customary to identify the letter Q with the "quality" of the resonance. A high quality means a slow ringdown, or in frequency space a narrow linewidth of the resonance.

Interestingly, at least etymologically, the letter Q was not purposefully assigned to the Q factor by its eponymous inventor K.S. Johnson as an abbreviation. Johnson, who worked on capacitors and inductors (then known as coils and condensers) at Western Electric was simply running out of letters: "His reason for choosing Q was quite simple. He says that it did not stand for "quality factor" or anything else, but since the other letters of the alphabet had already been pre-empted for other purposes, Q was all he had left."[Gre55]

In the reasoning of [Unt10a], the unusually high Q factors in prestressed silicon nitride string resonators are explained by an increase of the stored elastic energy with the tensile stress. In contrast to earlier interpretation [Sou09], the energy dissipation remains nearly constant. The tensile stress therefore does not decrease the damping in the resonating system, but increases the stored energy, thereby leading to a higher quality factor (cf. equation 2.6).

A high Q factor is very desirable in nanoresonators. The higher the Q factor, the more sensitive the device is to external influences. Thus high Q resonators are well suited for various sensor applications such as mass sensors [Nai09, Li10, Cha12b], resonant bio sensors [Bur07] and ultra sensitive force sensors [Mam01, Reg08]. In chapter 3 of this work, the external influence is exerted by an AFM tip. Its presence alters the resonant properties of the nanoresonator by changing the mechanical impedance mismatch of the resonator to its environments will be discussed in chapter 3.2. A high unperturbed quality factor makes the system very perceptive to the local perturbation caused by the AFM tip.

Another important property of the employed silicon nitride string resonators is their mechanical stability. On the one hand, this enables experiments with the AFM perturbing the nanomechanical system without - necessarily - crushing the sample, because the resonator spring constants are of the order of typical contact mode AFM cantilever spring constants ($\approx$ 1 N/m). On the other hand, the stability of the freely suspended structures enables a sample fabrication with high yield and manageable effort in the clean room. Concentrating on these two aspects, the following sections describe a static force measurement of pre-existing silicon nitride string resonator samples as a test of the AFM setup and the fabrication of the samples used for the dynamic measurements presented in chapter 3 and chapter 4.

### 2.2.1 Constant force measurements on silicon nitride nanostrings

As a first test of the AFM setup, constant force measurements on existing silicon nitride nanostring samples that had been fabricated by Thomas Faust for the work presented in [Unt10b] are conducted. The aim of these measurements is to test the capability of the instrument to execute constant force measurements on a nanostring sample and to find the AFM parameters that allow non-destructive experiments. The most important parameter here is of course the cantilever spring constant. If it is too stiff, the string gets pushed down onto the substrate or simply breaks. Another vital parameter is the scanning speed of the AFM. If it is too high, the feedback loop cannot react fast enough to the abrupt steps between substrate and resonator and the string can be broken.

Figure 2.7 shows an illustration of such a constant force measurement with an artist's impression of the AFM tip pressing down on the sample in Fig. 2.7a, and a schematic of the string shape for a given AFM tip position in Fig. 2.7b. The shape is assumed to be triangular, i.e. dominated by the built-in stress $\sigma_0$, rather than by a bending term, as it is expected for a string. This assumption is justified by measurements of resonant properties of the nanoresonators which clearly indicate that they behave like strings (stress

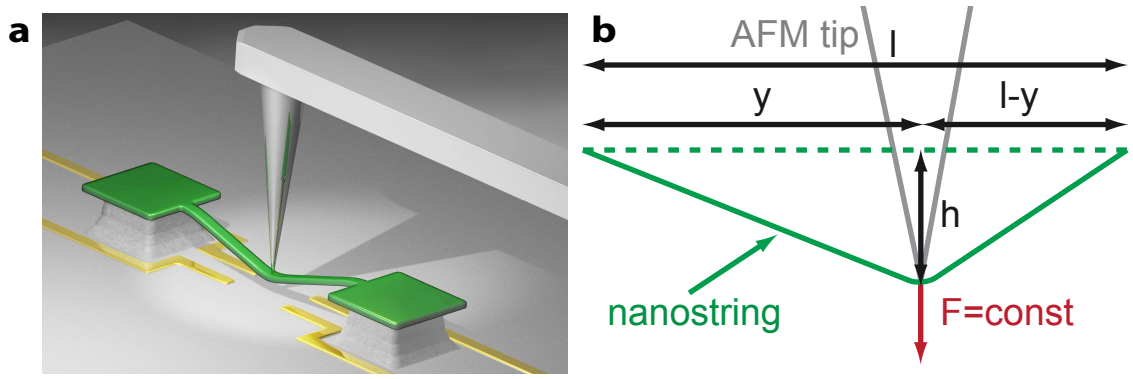


**Figure 2.7:** Illustration of the constant force measurement on a nanostring. **a** artist's impression of the measurement with the silicon nitride string decpicted in green and the AFM cantilever with tip in gray. For reasons of visibility of the individual components, the illustration is not to scale. The gold electrodes were used for the drive and detection of the string dynamics in [Unt10b]. **b** Triangular shape of the string for a given AFM tip position.

dominated) rather than beams (bending dominated) [Unt10a]. For a constant force measurement, this means that the restoring force of the string acting back on the force $F$ exerted by the AFM tip is mainly caused by the elongation of the string. To find out how far the string is pushed down for a lateral tip position $y$ (cf. Fig. 2.7b), it is convenient to first calculate the energy due to the elongation of the string and then take the derivative of this energy with respect to the height $h$ to find out the force acting back on the AFM tip. The elongation $\delta l$ of the string of length $l$ is given by

$$\delta l = \sqrt{h^2 + (l-y)^2} + \sqrt{h^2 + y^2} - l. \tag{2.8}$$

The energy is then calculated by integrating the force $F_{\mathrm{el}}(\delta l) = \sigma_0 A + (\delta l/l) EA$ along the string from zero to $\delta l$. Here, $E$ is the Young's modulus, and $A$ is the cross section of the string. The energy $W_{\mathrm{el}}$ thus reads:

$$W_{\mathrm{el}} = \sigma_0 A \delta l + \frac{1}{2}\frac{\delta l^2}{l} EA. \tag{2.9}$$

Taking the derivative of this expression with respect to $h$ gives the force $F$ in direction of $h$ and thus the force exerted by the string on the AFM cantilever. A series expansion of this force yields

$$F = \frac{Al\sigma_0 h}{(l-y)y} - O(h^3) \tag{2.10}$$

which means that for a constant force $F$, the height $h$ of the triangular string shape as depicted in Fig. 2.7b is approximately quadratic in tip-position $y$:

$$h(F, y, \sigma_0) = \frac{Fy(l-y)}{Al\sigma_0} \tag{2.11}$$

This is confirmed by experimental data taken on a 10 µm long string with a cross section

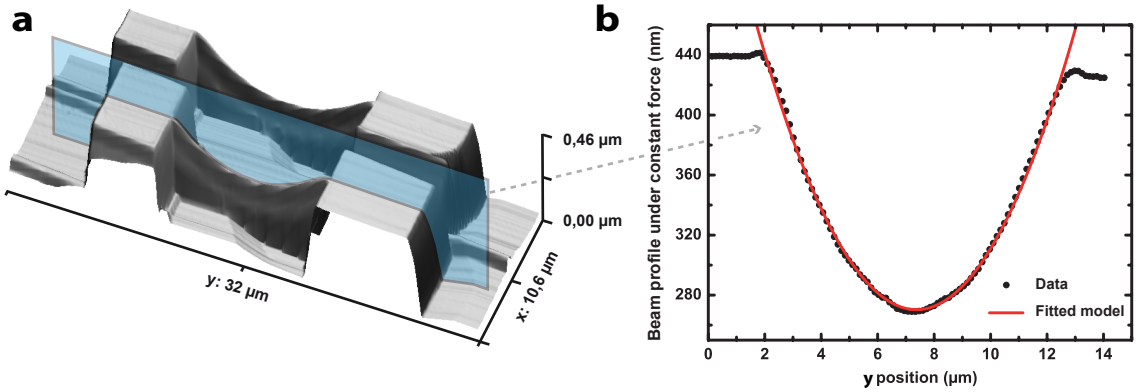


**Figure 2.8:** Constant force measurement on silicon nitride nanostrings. **a** Constant force image acquired using a silicon cantilever with a spring constant of 5.2 N/m. **b** A cut of the data in **a** (black dots) and a fit of the model (red line) yielding a tensile stress $\sigma_0$ of 720 MPa.

of 100 nm × 200 nm. A constant force AFM image of this string and an adjacent string of 15 µm length is displayed in Fig. 2.8a. The image was acquired using a cantilever with a spring constant of 5.2 N/m and a scanning speed of 1 µm /s. The feedback loop of the AFM was set to maintain a constant force of $8.45 \cdot 10^{-7}$ N. Figure 2.8b displays a cut of the data along the light blue plane in Fig. 2.8a and a fit of equation 2.11 to the string profile data. From this fit a tensile stress $\sigma_0$ of 720 MPa can be extracted. This value is in good accordance with the 830 MPa determined from resonant measurements in [Unt10a]. As one can see from Fig. 2.8b, the string can be significantly deflected (more than 150 nm) without breaking. However, the spring constant of the cantilever employed in this measurement is rather large for a contact mode measurement. Contact mode cantilevers with much smaller spring constants of the order of 0.1 N/m are available and were used in the dynamic measurements presented in chapter 3 and chapter 4. The effect of pushing down the string towards the substrate is thus much less pronounced.

### 2.2.2 Sample fabrication

The samples presented in this work are fabricated from 100 nm thick prestressed silicon nitride films that are deposited on 0.5 mm thick fused silica wafers. Fused silica is chosen as the substrate material - instead of the silicon used in [Unt09, Unt10a] - because a microwave cavity is employed for detection of the nanomechanical motion [Fau12a], which will be described in chapter 2.3. The fused silica substrate minimizes Ohmic losses of the microwave circuit originating in the bulk chip supporting the mechanical resonator. However, the non-conductive substrate presents a challenge for electron beam lithography, as electrostatic charges cannot be discharged and distort the electron beam. To circumvent this, a 3 nm chromium layer is evaporated onto the PMMA resist before each lithography step and removed before developing [Zha07]. Other conductive layers have been tested as well (aluminum, gold, polymeric coating SX AR-PC 5000/90.1 by *Allresist*,...), but

chromium has proven to yield the best results in terms of boundary smoothness of the developed resist.

With this method, standard e-beam lithography and lift-off processes can be used to define the sample structures. On the one hand, these are gold electrodes used for actuation, tuning and read-out of the mechanics as described in the following chapter 2.3. On the other hand, a cobalt etch mask is used as a protective layer for patterning the silicon nitride in an anisotropic inductively coupled reactive ion etch using sulfur hexafluoride ($SF_6$) and argon (Ar). The cobalt is then removed with "piranha" (hydrogen peroxide $H_2O_2$ and sulfuric acid $H_2SO_4$ in equal parts). Subsequently, the strings are released by a hydrofluoric wet etch. To ensure that the gold structures survive the liftoff and the hydrofluoric acid, a 3 nm chromium adhesion layer is employed. After blow drying the chips with nitrogen, they are glued onto the sample holder with photoresist (*Shipley Microposit 1813*) and a wire bonder is used to connect the cavity with the chip. An SEM micrograph of a silicon nitride string resonator as well as a photograph of the sample holder with a glued on chip is presented in the next chapter 2.3. A more detailed description of the respective processing steps of the chip fabrication can be found in Appendix B.

## 2.3 Transduction scheme

In order to conduct measurements on nanomechanical resonators in the AFM, a suitable read-out and driving scheme is required. In a first attempt, the AFM had been equipped with an additional optical fiber in order to employ an on-chip interferometric detection technique [Unt10b]. With the advancement of a cavity enhanced heterodyne detection [Fau12a, Kre11] however, a much better suited setup had been developed and the AFM was modified according to the requirements of this scheme as reported in chapter 2.1. Furthermore, the read-out is now combined with a dielectric drive [Unt09]. This ultimately enables tuning of both the resonance frequency and quality factor of the nanomechanical resonance with an applied dc voltage. The following treatment is based on a publication about this frequency and Q-control [Rie12]. It starts with a brief motivation of the presented work followed by a description of the investigated sample geometries and then deals with the frequency and Q factor control.

### 2.3.1 Motivation - state of the art transduction

Resonant micro- and nanoelectromechanical systems (M/NEMS) have both proven themselves technologically viable (frequency filtering in cell phones [Bou05], gyroscopes [Dea09], AFM-cantilevers [Bin86]) as well as shown great promise for next-generation sensor applications (mass sensors [Nai09, Li10, Cha12b], resonant bio sensors [Bur07] and ultra sensitive force sensors [Mam01, Reg08]).

As described in chapter 1, three areas of development are central to realizing the potential of high performance resonant micro- and nanomechanics: advancement of high

Q geometries and materials; improved readout schemes for mechanical motion, including compactness and integrability; and increased control of the resonant behavior of the mechanics. As already mentioned, the material system of choice in this work are high Q silicon nitride string resonators [Ver06, Unt10a]. Efficient integrated drive and read-out schemes have been developed to detect the sub-nanometer motion of small-scale resonant mechanics [Eki05]. Very good tunability of the resonance frequency can be achieved by capacitive coupling of the nanomechanical element to a side electrode [Koz06]. However, the required metalization of the resonant structure reduces the room temperature quality factor significantly [Yu12] via Ohmic losses. In the nanomechanics group of Eva Weig at the chair of Jörg Kotthaus at the LMU München, an efficient, room-temperature microwave mixing scheme based on a $\lambda/4$ copper microstrip cavity has been developed for readout [Fau12a], as well as a dielectric drive mechanism to actuate nanomechanics regardless of their material make-up [Unt09], importantly obviating the necessity to metallize otherwise low-loss dielectrics.

The sample designs introduced in the following present a continuation of this development that enables tuning of both the frequency and quality factor of nanomechanical resonators in the context of this highly applicable and integrable scheme [Fau12a]. Using the combined dielectric actuation and microwave readout schemes allows to controllably raise and lower the resonant frequency of various flexural modes of the mechanics, as well as to broaden the mechanical resonance linewidth. This represents a scheme for in situ Q factor control [Sul00, Rod03, Bhu10], a technique widely used in AFM measurements to increase scan speed by decreasing the mechanical response time [Mer93, Sul02]. In the presented scheme this is achieved by simply applying a dc voltage instead of the normally employed active feedback mechanism and is thus well suited for integration. The theoretical relationship between the design of the electrodes and the resulting control of a given mode is validated both by experiment and simulation. Being fully integrated and positioning free, this transduction scheme is ideally suited for integration with the AFM in the context of this work.

### 2.3.2 Sample geometries

The experimental setup is depicted in Fig. 2.9. The nanomechanical silicon nitride string is situated between a pair of near-lying electrodes (Fig. 2.9a). They are used to dielectrically actuate the mechanical resonance[Unt09] as well as to couple the mechanical resonator to an external microwave cavity. An equivalent circuit diagram is shown in Fig. 2.9b. Deflection of the string translates into a change of the capacitance $\mathrm{C_m(t)}$ between the two electrodes and thereby modulates the cavity transmission signal. The mechanical oscillation can then be detected by demodulating this signal [Fau12a]. To enable direct actuation of the mechanical resonator, a microwave bypass is introduced between ground and one of the electrodes using the single layer capacitor (SLC)[1] $\mathrm{C_{by}}$. Thus a dc

[1] 500U04A182KT4S from Johanson Technology

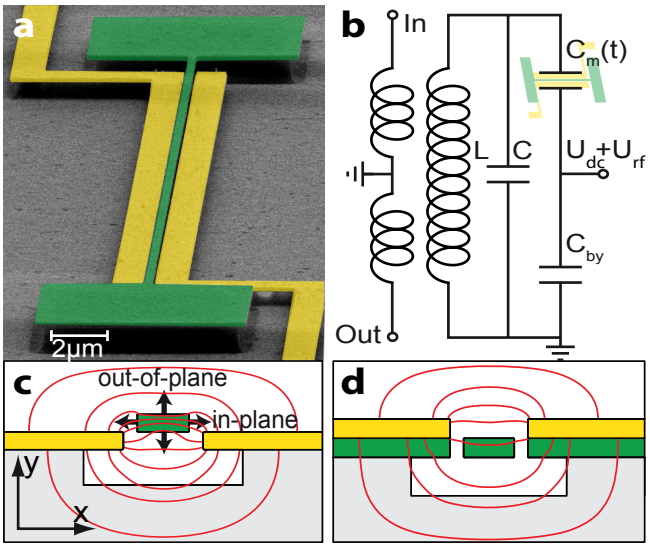


**Figure 2.9:** **a** SEM micrograph of a 55 µm long silicon nitride string resonator in the configuration depicted in **c**. **b** Equivalent circuit diagram of the transduction scheme with an inductively-coupled microwave cavity - represented by the capacitance C and inductance L - for dielectric readout. $\mathrm{C_m(t)}$ is the capacitance of the gold electrodes which is modulated by resonator displacement. The microwave bypass capacitor $\mathrm{C_{by}}$ allows the additional application of a dc and rf voltage. **c,d** Schematic cross section with simulated field lines for the elevated and lowered geometry. The arrows in **c** describe the directions of the in-plane and out-of-plane oscillation.

and rf voltage can be applied to this electrode, whereas the other electrode is grounded via the microstrip cavity (compare Fig. 2.9b).

For this study, two sample geometries for obtaining optimized gradient field coupling for the out-of-plane mode are fabricated from high-stress silicon nitride films deposited on fused silica. The geometries are schematically shown in Fig. 2.9c,d. Referring to the string's position with respect to the electrodes, the two structures will from now on be referenced as "elevated" (Fig. 2.9c) and "lowered" (Fig. 2.9d). The centerpiece of each structure is the 55 µm long silicon nitride string resonator with a rectangular cross section of width 260 nm and height 100 nm. The freely suspended resonator is bordered by two vertically offset gold electrodes, one of which is connected to the microstrip cavity with a resonance frequency of 3.5 GHz and a quality factor of 70, while the other electrode leads to the SLC. The essential difference between the geometries is the vertical positioning of the string with respect to the gold electrodes located on the substrate. This affects the dielectric environment because of the different distances to the substrate and thereby the course of the electric field lines as depicted in Fig. 2.9c,d. The simulated electric field lines for both geometries are obtained from finite element simulations using *COMSOL Multiphysics*, which allow to extract the electric field along the x- and y-direction. These inhomogeneous electric fields cause force gradients for the in- and out-of-plane modes of the resonator. They thus alter the restoring force of the respective mode and thereby its resonance frequency [Unt09]. At the same time, the mechanical quality factor can

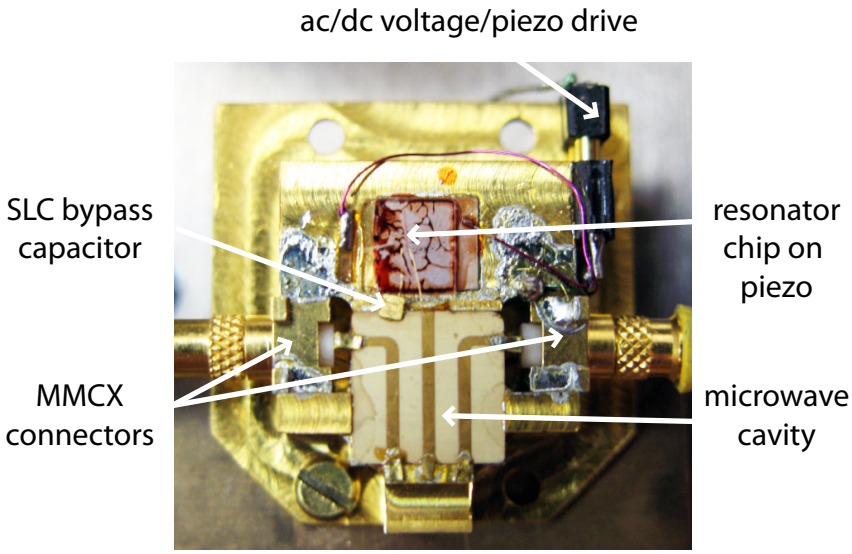


**Figure 2.10:** Photograph of the sample holder. It shows the gold coated brass sample holder with the microstrip cavity, MMCX connectors, the SLC capacitor, the transparent resonator chip glued on the piezo with photoresist (red) and the connector for the drive/tuning voltage.

be altered with the dc voltage, as the strong electric field and high field gradient lead to velocity-dependent dielectric losses in the string material. This frequency and linewidth tuning can be described by a simple model which agrees very well with the experimental findings and finite element simulations. The resonance frequency can be tuned over 5 % and the resonance linewidth can be increased by a factor of 6.

All measurements presented here are conducted at room temperature and a pressure of $< 10^{-4}$ mbar, using a sample holder as the one displayed in Fig. 2.10. The home built holder is CNC milled out of brass and coated with gold. Two MMCX connectors are soldered into the brass body and are used to connect the microwave setup to the cavity (see section 2.4 for a detailed schematic of the measurement setup). The microstrip cavity, a piezo and the SLC capacitor are also soldered to the holder. The resonator chip is glued onto the piezo with photoresist (*Shipley Microposit 1813*). The cavity and the SLC are connected with the resonator chip using wire bonds. The piezo can be employed as an alternative drive of the nanomechanical motion, but is not used in the measurements presented in this chapter.

### 2.3.3 Frequency tuning

The force gradient caused by the inhomogeneous electric field is proportional to the square of the voltage and thus leads to a quadratic dependence of the resonator resonance frequency on the applied dc voltage. This can be derived from the energy of the induced dipolar moment $\vec{p}$ of the dielectric resonator in an external electric field $\vec{E}$. Using

a scalar, complex polarizability $\alpha = \alpha' + i\alpha''$ and introducing a dependence of the electric field on the variable coordinate $\xi$, the energy $W$ reads

$$W = \vec{p} \cdot \vec{E} = pE = \alpha E^2 = \big(E(\xi)\big)^2(\alpha' + i\alpha'') \tag{2.12}$$

Here $\xi$ can be the x- or y-coordinate (compare Fig. 2.9c), so the following considerations apply to both the in- and out-of-plane mode. Assuming $E(\xi) = E_0 + E_1\xi$ for small displacements, the total energy can be separated into a real (stored) and an imaginary (dissipative) part.

$$W_{\text{stored}} = \alpha' \left(E_0^2 + 2E_0E_1\xi + E_1^2\xi^2\right) \tag{2.13}$$

$$W_{\text{loss}} = \alpha'' \left(E_0^2 + 2E_0E_1\xi + E_1^2\xi^2\right) \tag{2.14}$$

The second derivative of the stored energy provides an additional force gradient, i. e. an electrically induced spring constant $k_e$:

$$k_e = -\frac{\partial F_e}{\partial \xi} = \frac{\partial^2 W_{\text{stored}}}{\partial \xi^2} = \alpha' E_1^2 \tag{2.15}$$

The shift in resonance frequency caused by $k_e$ can be expressed as

$$f = \sqrt{\frac{k_0 + k_e}{m}} \approx f_0 + \frac{k_e}{2mf_0} = f_0 + \frac{\beta^2 U_{\text{dc}}^2 \alpha'}{2mf_0} \tag{2.16}$$

with a geometry-dependent proportionality between applied voltage and field gradient $E_1 = \beta U_{\text{dc}}$. Moreover, as predicted by finite-element simulations the sign of the gradient depends on the chosen geometry such that the out-of-plane mode changes its tuning direction between the elevated and the lowered design, which does not occur for the in-plane modes.

The quadratic tuning behavior with dc voltage is found to agree very well with the experimental data, as displayed in Fig. 2.11. For each mode and geometry the mechanical spectrum is taken for different dc voltages and microwave powers. The driving voltage $U_{\text{rf}}$ is kept constant in every measurement. The values for $U_{\text{rf}}$ lie within 80 µV and 1 mV, depending on the particular mode and geometry.

A Lorentzian fit to each mechanical spectrum yields the resonance frequency and the quality factor for each parameter set. The resonance frequencies lie around 6.5 MHz and the highest quality factor is $340\,000$ for the out-of-plane mode in the elevated design. Note that the tuning with microwave power is a result of the effective microwave voltage [Fau12a], and so is analogous to the tuning with a dc voltage. Subsequently, a fit of $f = f_0 + c_{\text{dc}}(U_{\text{dc}} - U_0)^2 + c_{\text{mw}}U_{\text{mw}}^2$ to the tuning curves shown in Fig. 2.11 is executed, using the natural resonance frequency $f_0$ and two tuning parameters for the dc voltage and the effective microwave voltage, as the dc and high frequency polarizability might differ. Additionally, the dc offset $U_0$ is introduced to account for a shift (typically less than 1 V) of the vertex of the tuning parabola, which is most likely caused by trapped charges

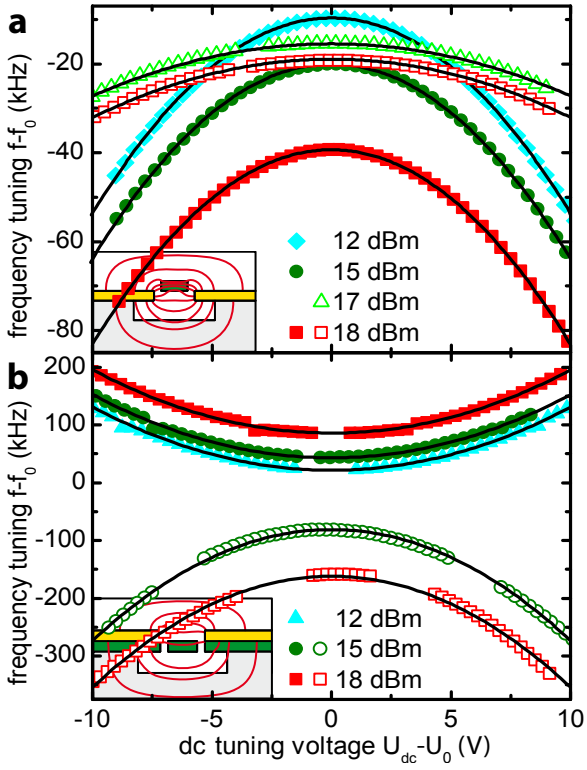


**Figure 2.11:** Quadratic tuning of the mechanical resonance frequency with dc voltage $U_{\mathrm{dc}}$ for the two different geometries. The graphs show the deviation of the resonance frequency $f$ from the natural resonance frequency $f_0$ of the resonator's respective mode (in- or out-of-plane, depicted as open and filled symbols) for different microwave cavity pump powers (in dBm). The solid lines are a fit of the model. **a** The force gradient has the same parity for the in-plane- as well as the out-of-plane mode. **b** With increasing $|U_{\mathrm{dc}} - U_0|$ the out-of-plane mode tunes upwards, the in-plane-mode downwards in frequency.

in the dielectric resonator material. As the influence of the microwave field on static dipoles averages out, there is no such shift resulting from the microwave voltage $U_{\mathrm{mw}}$. Consequently, the tuning parameters for each geometry and oscillation direction can be extracted. With increasing voltage $U_{\mathrm{dc}}$, for the elevated geometry depicted in Fig. 2.11a, both the in- and out-of-plane mode tune to lower frequencies, whereas for the lowered design (Fig. 2.11b), the out-of-plane mode tunes to higher frequencies, as predicted by the finite element simulations. The solid black lines in Fig. 2.11 show the fit of the model with a single set of parameters for each mode in excellent agreement with the data. In the case of opposite frequency tuning, the initial frequency difference of the in- and out-of-plane modes can be evened-out, which leads to an avoided crossing caused by a coupling between the modes [Fau12c]. The coupling of the resonator modes is treated in chapter 4 in detail. As the data points in the coupling region deviate from normal tuning behavior, they have been omitted in Fig. 2.11b (e.g. around $U_{\mathrm{dc}} - U_0 \approx \pm 2.5\,\mathrm{V}$ for the open, red rectangles).

### 2.3.4 Dielectric damping

Altering the dc or effective microwave voltage does not only shift the resonance frequency, but also influences the damping $\gamma = 2\pi f/Q = 2\pi\Delta f$ of the mechanical resonance and thereby the measured linewidth $\Delta f$ by adding a dielectric damping contribution $\gamma_e$. The dielectrically induced damping $\gamma_e$ - like the resonance frequency - varies quadratically with increasing voltage. This can be understood by analyzing the dissipated energy $W_{\mathrm{loss}}$ given by equation 2.14: A time average of this quantity over one period of mechanical vibration $\xi(t) = \xi_0 \cos(\omega t)$ gives

$$\overline{W_{\mathrm{loss}}} = \frac{\alpha''}{T} \int_0^T W_{\mathrm{loss}}(\xi(t))dt = \frac{1}{2}\alpha'' E_1^2 \xi_o^2. \tag{2.17}$$

Here we omit the $E_0^2$ term (as $\alpha''(\omega = 0) = 0$, otherwise static electric fields would lead to dissipation). As the mechanical stored energy $W_{\mathrm{mech}} = \frac{1}{2}m\omega_0^2\xi_0^2$ is much larger than the electrical energy $W_{\mathrm{stored}}$, one can approximate the additional electrical damping to be

$$\gamma_e(U_{\mathrm{dc}}) = \frac{\overline{W_{\mathrm{loss}}}\omega_0}{2\pi W_{\mathrm{mech}}} = \frac{\beta^2 U_{\mathrm{dc}}^2 \alpha''}{2\pi m\omega_0} \tag{2.18}$$

The measured damping versus dc voltage is shown in Fig. 2.12. It displays the quadratic behavior of the damping constant $\gamma = \gamma_0 + \gamma_e(U_{\mathrm{dc}}) = \gamma_0 + c_\gamma U_{\mathrm{dc}}^2$ of the out-of-plane mode in the elevated design for two different microwave powers. Here $\gamma_0$ is the intrinsic damping of the resonator [Unt10a] and $\gamma_e(U_{\mathrm{dc}})$ is given by equation 2.18. Again, the vertical offset between the two curves is explained by the effective microwave voltage acting analogously to a dc voltage. The solid lines in Fig. 2.12 are a fit of the model to the data, from which the curvature $c_\gamma$ can be extracted.

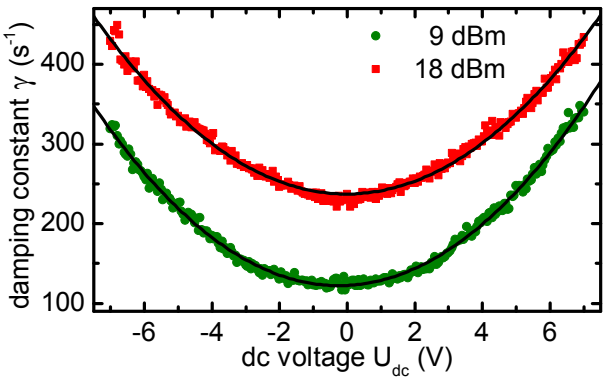


**Figure 2.12:** Damping constant versus dc voltage for two different microwave powers, exhibiting a quadratic behavior. The solid lines are a fit of the model mentioned in the text.

Using this curvature and equation 2.18, the imaginary part of the polarizability can be expressed as $\alpha'' = 2\pi c_\gamma m\omega_0/\beta^2$. Similarly, employing the curvature $c_{\mathrm{dc}}$ of the parabolic frequency shift and using equation 2.16 the real part $\alpha'$ reads $\alpha' = 2c_{\mathrm{dc}}mf_0/\beta^2$. The ratio $\tan(\phi) \coloneqq \alpha''/\alpha' = c_\gamma/2c_{\mathrm{dc}}$ is then independent of all resonator parameters and can be determined from the two curvatures. The measured values for damping and tuning curvatures are $c_\gamma = 5.2\,\frac{1}{\mathrm{V^2s}}$ and $c_{\mathrm{dc}} = 438\,\frac{1}{\mathrm{V^2s}}$, leading to $\tan(\phi) = 0.037$. By using the Clausius-Mossotti-Relation to first calculate the (lossless) $\alpha$ using $\epsilon = 7.5$, one can determine the dielectric loss tangent to be $\tan(\delta) = \epsilon''/\epsilon' = 0.016$, a value well within the range of loss tangents reported for silicon nitride thin films [Gou03]. Note that the time-varying capacitance $\mathrm{C_m(t)}$ induces a dissipative current in the electrodes, which also leads to a quadratically increasing damping [Koz06]. However, using values obtained from FEM simulations for the electrode capacitance and its variation with string deflection [Unt09], we estimate that this damping is three orders of magnitude smaller than that caused by dielectric losses. The relevant effect for the additional damping with increasing dc voltage is thus the dissipative reorientation of the dipoles in the resonator caused by its motion in a static, inhomogeneous electric field described by equation 2.17.

The dc voltage dependence of the mechanical damping $\gamma$ was also measured at zero microwave power using an optical detection technique [Kou05]. The resulting $\gamma_0$ was within a few percent of the value extracted from the 9 dBm curve in Fig. 2.12, demonstrating that a measurement at low microwave powers induces only negligible additional damping to the mechanical resonator.

In conclusion, an all-integrated setup for detecting and driving the vibration of nanomechanical resonators is presented. Dielectric frequency tuning of over 5 % of the natural resonance frequency can be achieved by applying a dc bias. Furthermore, dielectric losses become highly relevant when using nanoscale electrode geometries generating large field gradients providing high tunability. This allows to directly measure the ratio of the real and the imaginary part of the resonator's polarizability by monitoring the mechanical resonance. The resulting loss tangent agrees very well with material properties of silicon nitride. The induced dielectric damping could be used as a Q factor control [Rod03, Sul00, Ven11] that does not require any active electronics such as a phase-locked loop but rather a single dc voltage. Such a Q factor control can be employed to increase the bandwidth of NEMS sensors significantly, leading to much more adaptable devices. Without the need for active electronics this could prove to be very well suited for integrated designs. A full-fledged Q factor control however requires the possibility to also increase the quality factor. A possible realization - again without the need for external, active feedback - is the backaction caused by the read-out microwave cavity. This allows to reduce the mechanical resonance linewidth and even enter the regime of self-oscillation [Fau12a]. Backaction can also be used to broaden the linewidth, but we find the effect of dielectric losses to be more pronounced in our setup (a factor of six in linewidth broadening rather than a factor of two). Thus, together with microwave cavity backaction the mechanical resonance linewidth can be controlled from a few Hz up

to more than 100 Hz, thereby tuning the mechanical bandwidth by about two orders of magnitude.

Furthermore, by careful design of the geometry, one can choose the tuning behavior of the out-of-plane mode to be either upward or downward in frequency and thus tune the two orthogonal resonator modes both in the same or in opposite directions. This allows to observe a coupling between the two modes when they are tuned into resonance, which will be described in chapter 4.

Finally, the presented scheme is particularly suitable for measurements with an AFM tip as a controlled local perturbation as presented in chapter 3. The presented transduction scheme facilitates these experiments, since it obviates the need for peripheral components such as additional optics. Hence, simultaneously controlled AFM manipulation and independent monitoring of the mechanical resonance with high sensitivity is possible.

## 2.4 Electrical setup and devices

To facilitate automated measurements of the nanomechanical system with simultaneous AFM manipulation, the AFM setup and the electrical NEMS setup are combined. All measurement devices are controlled and read out with a computer. Figure 2.13 schematically shows the electrical setup. The individual components are labeled with numbers and listed in Table 2.1. The AFM setup consists of four devices (red frame in Fig. 2.13). A stepper controller provides the driving voltage for the coarse positioning piezo stepper unit as described in section 2.1.1. The scanner controller does the same for the fine positioning piezo scanner unit as well as for the piezo supporting the cantilever. The laser and detector unit houses the 1300 nm wavelength diode laser as well as a photodiode to detect the backreflected light. All of the aforementioned devices are connected to a scanning probe microscopy controller, which contains the feedback loops and acquires the AFM data. This controller is connected to the measurement computer via a USB opto-coupler to provide galvanic isolation between the computer and the measurement devices. This is important, because the power supply of the computer can otherwise lead to significant 50 Hz noise. All measurement devices are connected to the measurement computer via USB or GPIB. In order to use the opto-coupler also for GPIB connections, a USB-GPIB-adapter is employed. National Instruments LabView® is used as the measurement control software. The several LabView programs are coordinated with a sequencer program called LabScript[2]. The sequencer controls all the different LabView programs in a clearly arranged and adaptive manner. Every AFM function and all the functions of the other employed measurement devices are implemented as individual LabView programs, which are then executed sequentially by LabScript. Thus it is possible to address a certain AFM function, then measure the nanomechanical system for a certain set of parameters such as voltage or drive power, address the next AFM function and so forth. The remote

[2]Programmed by Quirin Unterreithmeier, modified by the author

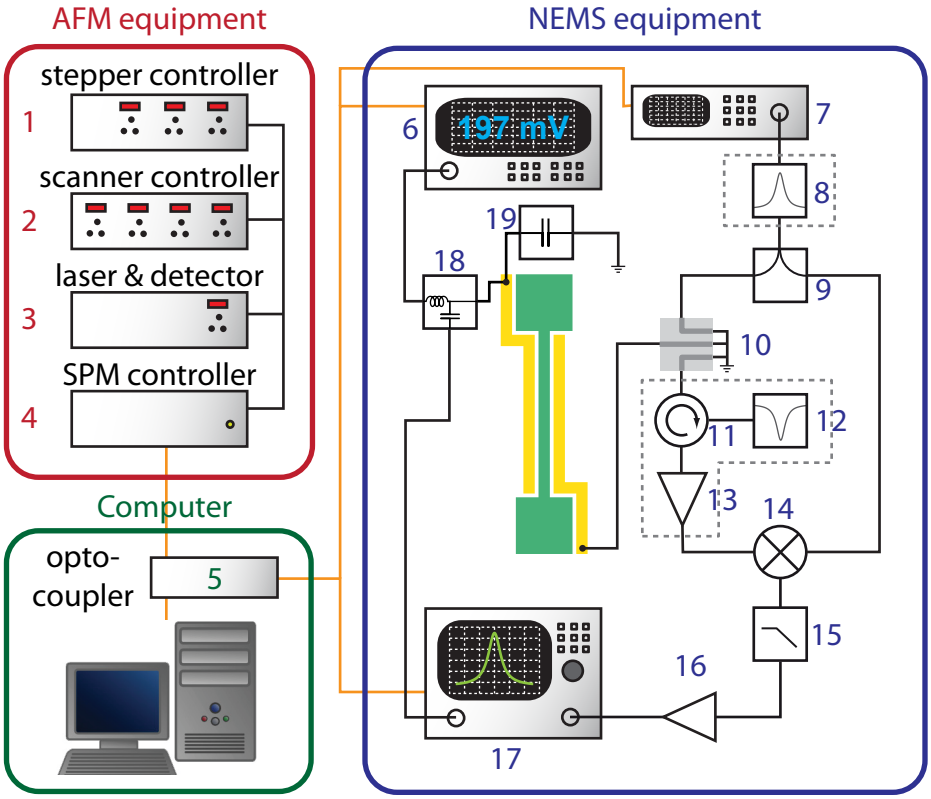


**Figure 2.13:** Scheme of the electrical setup for the AFM and the NEMS system.

control concept allows comfortable and fast adjustment of the measurement procedures and thus enables the automated measurements discussed in chapter 3 and chapter 4.

Figure 2.13 also displays the electrical NEMS setup in detail (blue frame in Fig. 2.13). Two different arrangements are indicated by the gray dashed boxes. For each configuration, the components framed by the dashed lines are either used or omitted. In the setup employing the components within the gray dashed boxes, the microwave signal provided by a signal generator (denoted by the number 7 in Fig. 2.13) is transmitted through a filter cavity [Rat12] to minimize phase noise. The signal is then split in two parts with a power splitter. One part is sent through the microwave cavity (cf. section 2.3), which is connected to one of the gold electrodes on the resonator chip. As discussed in section 2.3, the nanomechanical motion of the resonator modulates the microwave signal (≈3.5 GHz), creating sidebands with a frequency distance equal to the mechanical resonance frequency (≈6.5 MHz). These sidebands thus carry information on the nanomechanical vibration and are to be demodulated, amplified and detected. To this end, the signal coming from the microstrip cavity is first sent through a circulator to a notch filter cavity [Rat12]. This cavity serves the purpose of suppressing the carrier, so that the signal can be amplified before being sent to the RF-input of an IQ-mixer (denoted by the number 14 in Fig. 2.13) without overdriving the amplifier. The other part of the (unmodulated) microwave signal

is fed into the LO-input of the IQ-mixer. Thus the signal is demodulated by a quadrature amplitude demodulation [Fau12a]. After that, the signal is sent through a low pass filter in order to eliminate high frequency noise, amplified and fed to the input of a vector network analyzer and detected there. In the configuration that does not use the components in the gray dashed boxes, the microwave signal is simply sent through the cavity, mixed with the unmodulated signal, filtered with the low pass and amplified thereafter. The reason for amplifying before the IQ mixer is to account for its conversion losses that otherwise decrease the signal strength. In combination with the filter cavity after the microwave source the setup with the additional components leads to a signal enhancement of about 10 dB with respect to the setup that does not use them. The configuration with filter cavities represents the latest development of the electrical setup. The force dependent measurements presented in chapter 3 were measured with this arrangement. The position dependent measurements in chapter 3 as well as the measurements in chapter 4 were conducted with the configuration that first mixes and then amplifies.

To drive the nanomechanics, the output of the network analyzer, combined with a dc voltage via a bias tee is connected to the other gold electrode. In order to provide a ground path for the microwave detection scheme, a microwave bypass capacitor is employed. Alternatively, the mechanics can also be driven with a piezo ceramic transducer (not shown in Fig. 2.13 for the sake of simplicity).

| Number | Manufacturer | Designation | Description |
|---|---|---|---|
| 1 | attocube | ANC150 | piezo stepper controller |
| 2 | attocube | ANC200 | piezo scanner controller/voltage amplifier |
| 3 | attocube | LDM1300 | Laser (1300 nm) and detector module |
| 4 | attocube | ASC500 | SPM controller |
| 5 | icron | USB Ranger 2224 | Four port USB fiber extender |
| 6 | Knick | S 252 | dc voltage source |
| 7 | Rohde&Schwarz | SMA100A | low phase noise microwave signal generator |
| 8 | Sophie Ratcliffe | | microwave filter cavity [Rat12] |
| 9 | Anaren | 42010 | 1-4 GHz power splitter |
| 10 | LPtec | | silver-coated microstrip cavity [Kra12] |
| 11 | Lynx | 15.00479.04.00 | 2-4 GHz circulator |
| 12 | Sophie Racliffe | | Notch filter cavity [Rat12] |
| 13 | Minicircuits | ZX60-3800LN-S+ | 3.3-3.8 GHz amplifier with 20 dB gain |
| 14 | Marki | IQ-0307-LXP | IQ mixer |
| 15 | Stephan Manus | | 100 MHz low pass filter |
| 16 | Miteq | AU-1189 | low noise rf amplifier (35 dB gain) |
| 17 | Rohde&Schwarz | ZVB4 | network analyzer |
| 18 | Minicircuits | ZFBT-4R2GW+ | bias tee |
| 19 | Johanson Tech. | 500U04A182KT4S | 1.8 nF single layer microwave capacitor |
| 20 | National Instruments | NI GPIB-USB-HS | USB-GPIB adaptor |

**Table 2.1:** List of employed components and devices.

# Chapter 3

# Nanoscale mechanical impedance mismatch imaging by contact mode AFM

For nanoelectromechanical (NEMS) resonators, controlling the exchange of vibrational energy between the resonator and its environment is highly desirable: High Q factor resonators are attained by suppressing this energy transfer [Cha12a] which allows to realize ultrasensitive devices [Mam01, Kno03, Rug04, Cha12b]. Conversely, the energy transfer can be engineered to realize integrated resonator devices communicating through phononic waveguides [Hab12]. In terms of integrated NEMS-resonator circuits, it is convenient to think of the resonator's vibrational modes as localized standing waves caused by the mismatch in mechanical impedance between the support and the suspended region. A large impedance mismatch gives rise to a large wave reflection at the interface and a correspondingly highly localized vibrational mode with a large Q factor (neglecting intrinsic losses, such as defect mediated inelastic scattering of high energy thermal phonons from the resonator mode [Unt10a]). On a macroscopic scale, surface impedance meters are commercially available for material characterization [Kle68]. On the nanoscale, the mechanical surface impedance of a substrate has been probed using AFM by either using a vibrating tip or shaking the substrate to be characterized [Gie03, Rad92, Yam94, Sta12].

The mesurements presented in this chapter demonstrate direct in situ manipulation of the mechanical impedance mismatch at the nanoscale. This is accomplished by forming a mechanical point contact between the high Q silicon nitride string resonator used as a precise sensing device and an AFM tip introducing a controlled local perturbation, in analogy to the groundbreaking electronic transport studies reported in ref. [Top00]. In the clamping region of the resonator, its flexural modes induce minute deformations allowing a transfer of vibrational energy into the AFM cantilever. The amount of transferred energy is independently probed by the decrease in Q factor of the resonator using the transduction scheme presented in chapter 2. The energy transfer is controlled by changing the contact position and/or the force applied to the AFM tip. Thus, the passage between a

highly mismatched, high-Q system to a highly matched, low-Q system on a single resonator can be observed. While this method does not address all relevant intrinsic sources of damping [Lif00, Unt10a, Rem12], it allows for local quantification of the contribution coming from vibrational modes radiating into the supports [Cro01, WR08]. As the AFM tip remains in contact with the support at all times, the resulting change in Q factor and resonant frequency is governed by the detailed nature of the microscopic contact dynamics. This is in contrast to other spectroscopy methods using AFM (see for instance ref. [Pla13]) where the AFM operates in non-contact mode.

This chapter starts with a description of the experimental setup, followed by a presentation of position and force dependent measurements. Then, a theoretical model which was developed by Andreas Isacsson from Chalmers University of Technology in Gothenburg in a collaboration is presented, explaining the experimental findings by a modified mechanical impedance mismatch between the resonator and its clamping region. This model is used to fit and analyze the data.

## 3.1 Local probe measurements

The experimental setup consists of a high-Q silicon nitride string resonator as described in chapter 2.3 that is 55 µm long, 270 nm wide and 100 nm thick. The fundamental flexural out-of-plane resonance frequency is $f_0 \approx 6.6$ MHz with room temperature quality factors reaching up to $Q_0 \approx 250\,000$. This corresponds to a damping rate $\gamma_0 = 2\pi f_0/Q_0$ of 166 $s^{-1}$. The resonator is operated in the customized atomic force microscope presented in chapter 2.1 with pressures < $10^{-4}$ mbar at room temperature. Figure 3.1 displays the local probe setup schematically. The AFM in contact mode locally perturbs the resonator's acoustic environment. This leads to a flow of energy from the nanomechanical system into the cantilever, as symbolized by the corrugated arrows in Fig. 3.1a. A topographic image of one resonator clamping region is depicted in Fig. 3.1b. In the measurements reported here, unless stated otherwise, contact mode silicon cantilevers (450 µm long, 50 µm wide and 2 µm thick, model ContAl manufactured by Budget Sensors) were employed.

In a typical measurement, the acquired AFM topography image is used to define the grid for a point by point measurement in the vicinity of the clamp (red rectangle in Fig. 3.1b). The AFM is positioned at the first point of the grid. Hereupon the driven, linear amplitude response of the nanomechanical resonator is measured with a network analyzer using the circuitry recapitulated in Fig. 3.1c (see also Fig. 2.13 in chapter 2.3). Subsequently, the topographic information is read out before the tip is positioned at the next grid point, where the measurement of the resonator's mechanical response is repeated.

Figure 3.2 displays the effect of the presence of the AFM tip on the nanomechanical system in such an experiment. The measurement was conducted on a grid with 40 points in x- and 20 points in y-direction, corresponding to a pixel size of 50 nm times 30 nm. The normalized amplitude spectra of the resonator (Fig. 3.2a) for two tip positions in the clamping region illustrated in the inset, one being close to the resonator (circles) and one

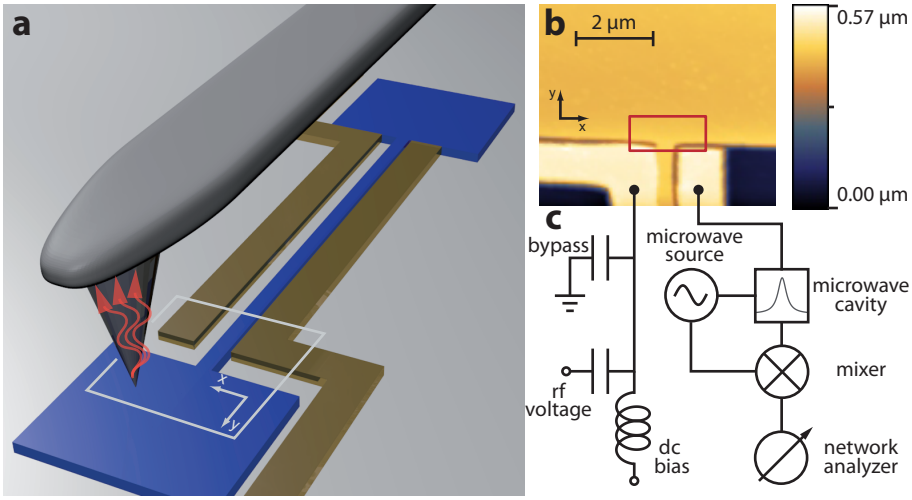


**Figure 3.1:** Local probe setup. **a** Illustration of the nanomechanical system with the AFM tip as a controlled local perturbation of the resonator's acoustic environment. This leads to a flow of energy from the nanomechanical system into the cantilever (gray), as symbolized by the corrugated red arrows. The resonator (blue) is 55 µm long, 250 nm wide and 100 nm thick. It is bordered by two 1 µm wide gold electrodes (yellow) for actuation and detection. The illustration is not to scale in order to provide better visibility of the individual components. **b** AFM image of a resonator clamp as marked by the light gray frame in **a** (rotated by 180°). **c** Electrical setup. One of the electrodes is connected to a microstrip cavity for detection [Fau12a], whereas the other electrode is used for the application of an rf and a dc bias for actuation [Unt09]. The bypass capacitor provides a ground path for the microwave detection [Rie12].

further away (triangles), show a marked shift of the resonance frequency as well as a line broadening. The outlines of the clamp, shown in the inset of Fig. 3.2a, were extracted from the AFM topography data. The seemingly larger resonator width compared to the 270 nm obtained from SEM imaging originates from the unavoidable convolution of tip shape and sample topography [Kel91, Rie12], as described in chapter 2.1.2. With a tip half cone angle of 25°and a string-substrate distance of ≈ 400 nm, one can estimate that the resonator will appear to be $2\,(\tan(25°)\cdot 400)\ \mathrm{nm} + 270\,\mathrm{nm} = 640\,\mathrm{nm}$ wide, which corresponds to the observed width in the inset of Fig. 3.2a. The data presented in Fig. 3.2 were taken for the fundamental out-of-plane mode of a resonator with an unperturbed resonance frequency $f_0$ of 6.61 MHz and quality factor $Q_0 = f_0/\Delta f_0$ of 150 000 where $\Delta f_0$ is the full width at half maximum of the Lorentzian amplitude spectrum, corresponding to a damping rate $\gamma_0 = 2\pi\Delta f_0$ of 277 $\mathrm{s}^{-1}$. For the measurements displayed in Fig. 3.2, the AFM feedback loop was set to maintain a constant force of 9.2 nN. A Lorentzian fit to each mechanical spectrum then yields the respective perturbed resonance frequency $f_{\mathrm{pert}}$ and damping rate $\gamma_{\mathrm{pert}} = 2\pi\Delta f_{\mathrm{pert}}$ for a given tip position.

Both frequency shift $\delta f = f_{\mathrm{pert}} - f_0$ and damping $\gamma_{\mathrm{pert}}$ for tip positions following the three lines depicted in the inset of Fig. 3.2a are displayed in Fig. 3.2b and Fig. 3.2c. The measurements clearly show a position-dependent shift of the resonance frequency to higher frequencies as well as an increase in damping rate as the tip is brought into the vicinity of the clamping region. In the following section 3.2, it will be shown how this can

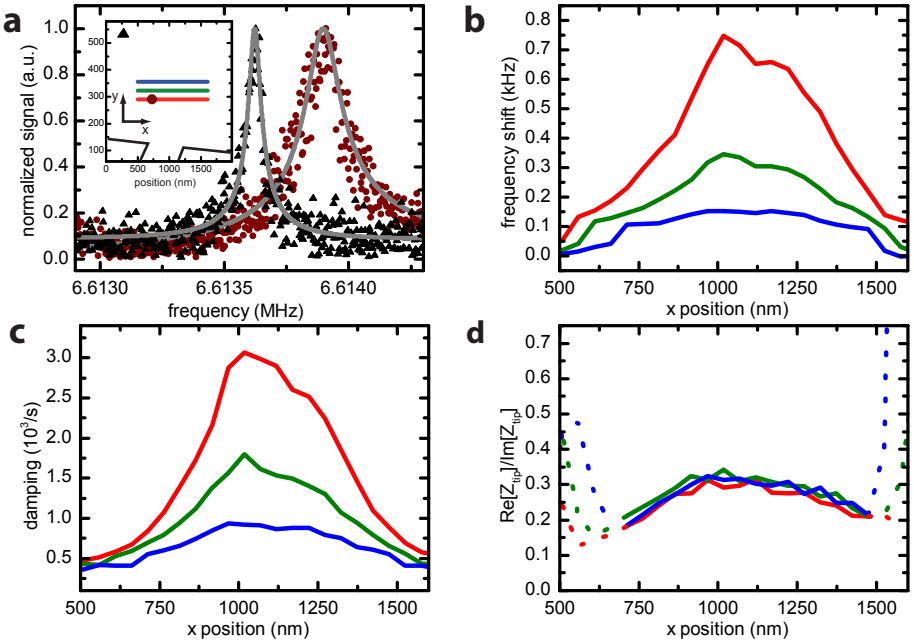


**Figure 3.2:** Tip induced frequency shift and damping. **a** Lorentzian amplitude spectra and fits for two spatially well separated tip positions (tip position marked with the respective plot marker symbol). **b** Shift of the resonance frequency with tip position along three lines specified in the inset of **a**. The data and the respective tip positions are color coordinated. **c** Damping rate versus tip position for the same line cuts. **d** The theoretical model predicts the ratio of real- and imaginary parts of the contact impedance to be an invariant in approximate agreement with the observed values displayed in **d**. This ratio has been computed from the measured frequency shift and damping curves in **b** and **c**. As it is only well defined for non-zero frequency shifts and diverges far from the resonator, the dashed sections lie beyond the validity of the model.

be qualitatively and quantitatively understood by the tip-modified mechanical impedance of the resonator's environment and the resulting change in mechanical impedance mismatch between the resonator and its clamping region. Hence vibrational energy is partly reflected and partly extracted from the resonator and flows into the AFM cantilever, leading to the observed change in resonance frequency and damping. Remarkably, even for the tip at a distance of 150 nm from the freely suspended part of the resonator, i.e. the situation corresponding to the center of the red trace in Fig. 3.2c, the energy extraction already increases the damping rate by more than an order of magnitude.

As the tip moves from the clamp towards the clamp-resonator-interface, the damping rate further increases until the resonance eventually disappears in the noise floor. This demonstrates that by locally changing the mechanical impedance mismatch at the resonator's support, one can observe the passage from a highly mismatched, i.e. high-Q system ($Q = 150\,000$), to a significantly better matched system with a very low quality factor ($Q < 2\,000$) on a single resonator.

## 3.2 Theoretical modeling of the mechanical impedance

### 3.2.1 Assumptions

To explain and fit the experimental data, a minimalistic model for the interaction between the resonator and the AFM cantilever is introduced. In this model, it is assumed that only one flexural mode of the resonator with mode index $n = 0, 1, 2, ...$ is actuated at a time and that this mode has a spatial profile $\vec{u}_n(\vec{x})$ penetrating a certain distance into the clamping region. The cantilever tip, in contact with the substrate at a point on the support $\vec{x}_0$, is assumed to induce a local, delta-function like force at this point. This is valid as long as the radius $R$ of the tip is small compared to the characteristic length scale over which $\vec{u}_n(\vec{x})$ varies. In general, the force is a nonlinear function of the instantaneous surface displacement amplitude $\propto \vec{u}_n(\vec{x})$ and also depends on the net static force externally applied downwards on the cantilever. Here, it is assumed that the vibrations at the position of the mechanical point contact between the AFM and the resonator are so small that the force may be linearized around the stationary equilibrium point and that the tip-surface interaction does not display any significant retardation effects. Of importance is also that there is no slipping motion of the AFM-tip over the substrate during the measurement. No particular assumptions about the normal mode spectrum of the AFM cantilever are made.

Section 3.2.2 turns to the general properties of the resonator interacting with the AFM cantilever tip and measurement data to validate the assumption of linearity of the resonator-cantilever interaction is presented. Then in section 3.2.3 the concept of mechanical impedance is introduced and applied to the resonator-AFM-tip system in section 3.2.4. In section 3.2.5 the equations valid for the case of a single flexural out-of-plane resonant mode are explicitly derived. The modeling of the tip-surface interactions is covered in section 3.2.6.

### 3.2.2 General considerations and linearity

Before going into a more detailed derivation, some introductory observations have to be made. Quite generally, the out-of-plane vibration mode of the resonator with mode index $n = 0, 1, 2, ...$, coordinate $q_n$, damping rate $\gamma_n$ resonance frequency $\omega_n$ and mass $m$ can be described as a driven harmonic oscillator interacting with the cantilever-system

$$\ddot{q}_n + \gamma_n \dot{q}_n + \omega_n^2 q_n = m^{-1}(f_D(t) + g_i[t, q_n(t'), \dot{q}_n(t'), \vec{Q}(t'), \vec{P}(t')]).$$

Here, the vectors $\vec{Q}(t), \vec{P}(t)$ represent the cantilever degrees of freedom in generalized coordinates and momenta. These include all the mechanical degrees of freedom in the AFM cantilever. The force term $f_D(t)$ represents the external drive of the resonator with zero time average. The functional $g_i$ describes the effect of the cantilever-resonator interaction on the resonator. In the absence of other mechanisms that drive the AFM cantilever, the normal mode coordinates $(\vec{Q}(t), \vec{P}(t))$ at a time $t$ must then be functionals of

$(q_n(t), \dot{q}_n(t))$ only. Hence, it is always possible to formally solve for the cantilever degrees of freedom and write down a closed equation of motion for the resonator interacting with the AFM cantilever as

$$\ddot{q}_n + \gamma_n \dot{q}_n + \omega_n^2 q_n = m^{-1}(f_D(t) + f_i[t, q_n(t'), \dot{q}_n(t')]).$$

For the sake of simplicity, the following considerations will be restricted to the fundamental mode with $n = 0$:

$$\ddot{q}_0 + \gamma_0 \dot{q}_0 + \omega_0^2 q_0 = m^{-1}(f_D(t) + f_i[t, q_0(t'), \dot{q}_0(t')]).$$

Note, however, that the following in principle applies to all other resonator modes.

For sufficiently small vibration amplitudes, and for well separated resonator eigenfrequencies, one can linearize the above equation. Expanding around the stationary equilibrium $q_0(t) = \bar{q}_0$ by solving $m\omega_0^2 \bar{q}_0 = f_i[t, q_0(t') = \bar{q}_0, \dot{q}_0(t') = 0]$, setting $q_0 = \bar{q}_0 + \delta q(t)$ and considering the time translational invariance of the AFM cantilever response, the linearized equation of motion becomes

$$\delta\ddot{q} + \gamma_0 \delta\dot{q} + \omega_0^2 \delta q = m^{-1}\left(f_D(t) + \int dt' \left[\chi_1(t-t')\delta q(t') + \chi_2(t-t')\delta\dot{q}(t')\right]\right).$$

where $\chi_{1,2}$ are causal response functions

$$\chi_1(t-t') \equiv \frac{\delta f_i[t, q = \bar{q}_0, \dot{q}_0 = 0]}{\delta q(t')}, \quad \chi_2(t-t') \equiv \frac{\delta f_i[t, q = \bar{q}_0, \dot{q}_0 = 0]}{\delta \dot{q}(t')}.$$

Solving by Fourier transformation yields

$$\delta\hat{q}(\omega) = \frac{\hat{f}_D(\omega)}{m[-\omega^2 - i\gamma_0\omega + \omega_0^2] - \hat{\chi}_1(\omega) + i\omega\hat{\chi}_2(\omega)} = \frac{\hat{f}_D(\omega)}{m[-\omega^2 - i\gamma_0\omega + \omega_0^2 - \hat{\chi}_{\mathrm{tip}}(\omega)]}, \tag{3.1}$$

where in the last equality, dissipative and conservative interactions have been merged into a single response function $\hat{\chi}_{\mathrm{tip}}(\omega) = [\hat{\chi}_1(\omega) + i\omega\hat{\chi}_2(\omega)]/m$. For this quite general expression to be valid, it is necessary that one is operating in the limit where a linearization of the tip-resonator interaction is legitimate.

A simple way to experimentally validate the assumption of linearity is to evaluate the frequency shift $\propto \mathrm{Re}[\hat{\chi}_{\mathrm{tip}}(\omega)]$ and the damping $\propto \mathrm{Im}[\hat{\chi}_{\mathrm{tip}}(\omega)]$ as a function of resonator amplitude. In a linear theory, there should be no influence of the amplitude on these quantities. Therefore, mechanical spectra for varying resonator driving powers with the AFM tip in contact at a fixed position near the clamp-resonator-interface for both the out-of-plane and the in-plane fundamental flexural mode are measured. To additionally check for a potential position dependence, this measurement was conducted on a grid of AFM tip positions spanning the whole clamping region. As can be seen in Fig. 3.3, which displays out-of-plane and in-plane resonances and Q factors for one such measurement point for

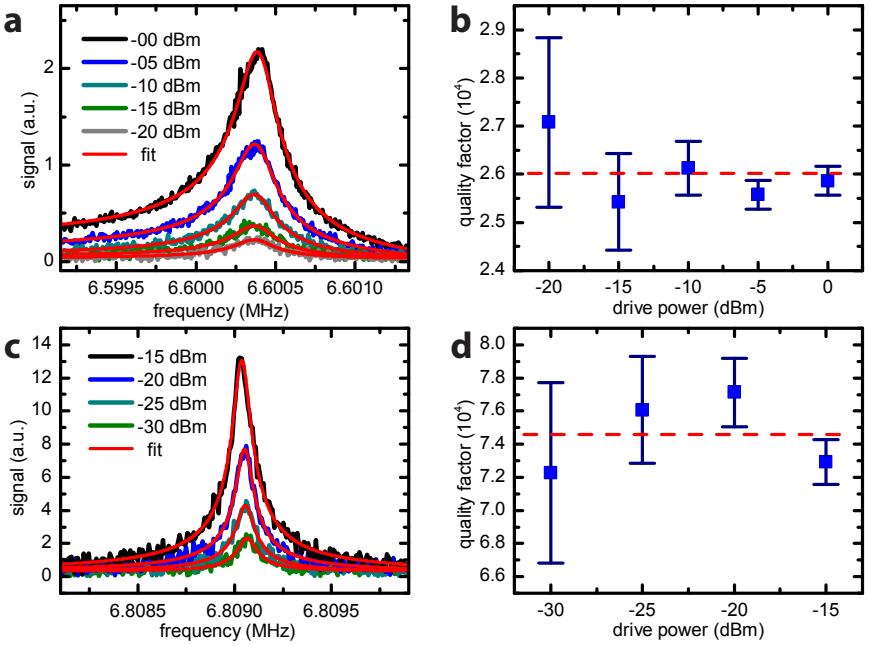


**Figure 3.3:** Linearity of the tip-resonator interaction. All spectra were taken with the AFM-tip at a fixed position close to the clamp-resonator-interface and a constant force of 9.8 nN acting on the AFM tip. **a** Spectra of the fundamental out-of-plane mode of a resonator with an unperturbed quality factor of 175 000 and a resonance frequency of 6.6 MHz. The resonator drive power was swept from -20 dBm to 0 dBm in steps of 5 dBm. The red lines are Lorentzian fits to the spectra. **b** Obtained quality factors versus drive power for the out-of-plane spectra. The red dashed line indicates the mean value. **c** Spectra of the fundamental in-plane resonance with an unperturbed quality factor of 90 000 and a resonance frequency of 6.8 MHz. The drive power was swept from -30 dBm to -15 dBm in steps of 5 dBm. **d** Obtained quality factors versus drive power for the in-plane spectra. The red dashed line again signifies the mean value.

various driving strengths, there is no evidence that a linear theory should not be valid here. The Q factors for both modes show no systematic deviation from the mean value within the error bars. The resonance frequency does not change, either. Also, independence of drive power was found for all other points of the measurement grid.

### 3.2.3 Mechanical impedance

A convenient quantity to describe the effect the AFM tip exerts on the nanomechanical resonator is the mechanical impedance. Therefore this section introduces the concept of mechanical impedance of basic mechanical elements such as a spring or a mass and then treats combinations of such basic elements in lumped element models. An elaborate treatment of mechanical impedance theory as well as a table of the impedances of various combined elements can be found in [Har09].

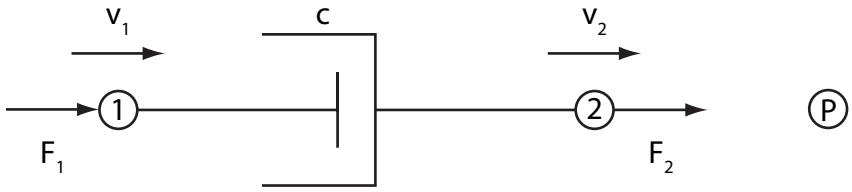


**Figure 3.4:** Schematic illustration of a mechanical resistance, symbolized by a dashpot with damping constant c.

In vibrating systems, the mechanical impedance $Z$ at a given position is defined as the ratio of the applied force $F$ to the velocity $v$ at this position.

$$Z = \frac{F}{v} \tag{3.2}$$

In the following the force $F$ is assumed to vary periodically in time with frequency $\omega$ and magnitude $F_0$, such that

$$F = F_0 e^{i\omega t}. \tag{3.3}$$

Applying this force to a linear mechanical system leads to a velocity

$$v = v_0 e^{i(\omega t+\phi)}. \tag{3.4}$$

Here $v_0$ is the magnitude of the velocity and $\phi$ is a phase between $F$ and $v$. In the following, the mechanical impedance of basic elements that can be used to build lumped element models of mechanical systems is introduced. These elements are mechanical resistances, springs and masses.

### Mechanical Resistance

In a mechanical resistance or damper, the relative velocity between two points is proportional to the applied force. Because this relation is fulfilled by viscous friction, a mechanical damper can be symbolized by a dashpot as depicted in Fig. 3.4. The components comprising this ideal resistance are assumed to be massless and infinitely rigid. The velocity $v_1$ of point 1 with respect to the velocity $v_2$ at point 2 (measured with respect to the stationary point P) is

$$v = (v_1 - v_2) = \frac{F_1}{c} \tag{3.5}$$

where $c$ is the damping constant or mechanical resistance. If the force given by equation 3.3 is applied at point 1 and point 2 is fixed, the velocity $v_1$ becomes

$$v_1 = \frac{F_0 e^{i\omega t}}{c} = v_0 e^{i\omega t} \tag{3.6}$$

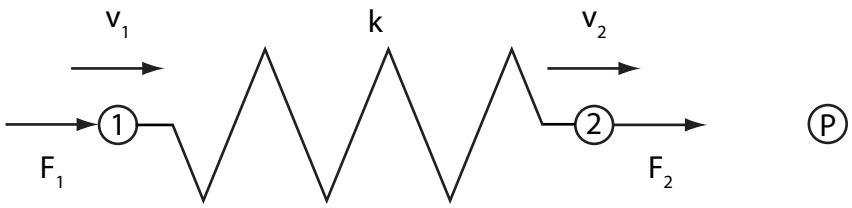


**Figure 3.5:** Schematic illustration of an ideal spring with a spring constant k.

Because the damping coefficient is real, the force and velocity are in phase. The mechanical impedance can then be identified to be equal to the damping coefficient:

$$Z_{\text{res}} = \frac{F}{v} = c \tag{3.7}$$

### Spring

The displacement between the end points of a linear spring is proportional to the applied force (c.f. Fig. 3.5). With $x_1, x_2$ being the displacements at points 1 and 2 relative to the reference point P and a spring constant $k$ this can be written as

$$x_1 - x_2 = \frac{F_1}{k} \tag{3.8}$$

The applied force is transmitted by the spring, so that $F_1 = F_2$. If the force given by equation 3.3 is applied at point 1 and point 2 is fixed, the displacement of point 1 can be expressed as

$$x_1 = \frac{F_0 e^{i\omega t}}{k} = x_0 e^{i\omega t} \tag{3.9}$$

The derivative of this equation with respect to time gives the velocity. Using equation 3.2 one finds the mechanical impedance of a spring to be

$$Z_{\text{spring}} = \frac{-ik}{\omega} \tag{3.10}$$

From this expression one can see that the velocity is 90° ahead of the force in a spring, just as the current in a capacitor is 90° ahead of the applied voltage. In fact, by identifying the spring constant $k$ in the mechanical case with the capacitance $C$ in the electrical case, where the impedance is given by the ratio of voltage to current, one finds that the mechanical impedance of a spring is identical to the electrical impedance of a capacitor.

### Mass

For a mass $m$, the acceleration $\ddot{x}$ is given by

$$\ddot{x} = \frac{F}{m} = \frac{F_0 e^{i\omega t}}{m} \tag{3.11}$$

By integrating equation 3.11 and using equation 3.2, the mechanical impedance is found to be

$$Z_{\mathrm{mass}} = i\omega m \tag{3.12}$$

From this expression one can see that the velocity lags 90° behind the force for a mass, just as the current in an inductor lags 90° behind the applied voltage. By identifying the mass $m$ in the mechanical case with the inductance $L$ in the electrical case one sees that the mechanical impedance of a mass is identical to the electrical impedance of an inductance.

### Parallel and series elements

Just as in the electrical case, the combined impedances of assemblies of basic elements can be easily calculated. Such assemblies can be divided into two basic groups, parallel elements and series elements. In contrast to the electrical case however, the total mechanical impedance for parallel elements is the sum of the impedances of the individual elements [Har09]

$$Z_{\mathrm{par}} = \sum_l Z_l \tag{3.13}$$

and the total impedance for series elements is given by

$$\frac{1}{Z_{\mathrm{ser}}} = \sum_l \frac{1}{Z_l}. \tag{3.14}$$

This inverted behavior with respect to the electrical case comes from the fact that for parallel mechanical elements, the (connected) end points have to have the same velocity. In the electrical case, the voltage is equal for every individual component in a parallel circuit. From the respective definitions of the impedance (mechanical/electrical) one can directly see that this leads to the inversion between the parallel and series element case.

### Reflection at interfaces

As in the electrical realm, an impedance discontinuity causes a reflection of an incident wave. The same applies for the mechanical case, and a reflection coefficient $R$ for waves can be written as [Har09]

$$R = \left| \frac{Z_1 - Z_2}{Z_1 + Z_2} \right|^2, \tag{3.15}$$

where $Z_1$ and $Z_2$ are the different impedance values at the discontinuity.

As an exemplification of such an impedance discontinuity in an elastic system, consider the geometry depicted in Fig. 3.6. A region of width $b$ is interfaced with a region of width $a$. If one assumes a mechanical impedance $z$ per unit length and - as parallel mechanical impedances add - integrates over the width, one obtains the impedance $Z_b = z \cdot b$ at the interface. The same way, the impedance on the other side of the interface is given by

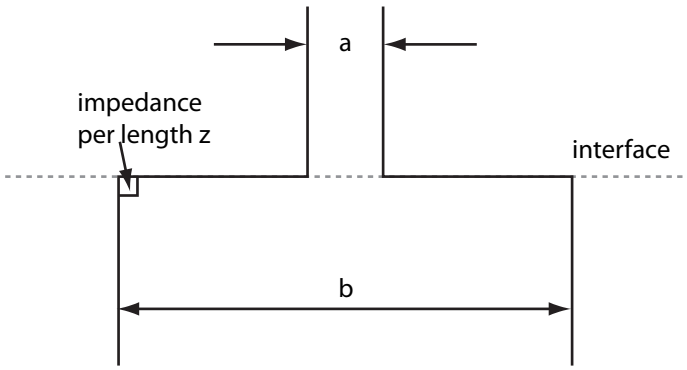


**Figure 3.6:** Schematic illustration of an impedance discontinuity. A region with width b is interfaced with a region of width a.

$Z_a = z \cdot a$. The reflection coefficient is thus only given by the geometric parameters $a$ and $b$:

$$R = \left|\frac{Z_a - Z_b}{Z_a + Z_b}\right|^2 = \left|\frac{a-b}{a+b}\right|^2 \tag{3.16}$$

In the limit $a \to b$, the reflection coefficient becomes zero, and in the limit $a \to 0$, it approaches unity. Identifying a high reflection coefficient with low radiation loss for a resonator comprised of two such junctions, one can see that the resonator width should be small, whereas the clamp should be very wide in order to obtain high reflection. Note however that this is quite an oversimplification of the problem, and much more elaborate calculations are necessary to obtain realistic values for specific resonator geometries [Col11]. Nevertheless, the presented example descriptively shows that such support losses strongly depend on the geometry of the support.

### 3.2.4 Interpretation in terms of mechanical impedance matching

Using the notion of mechanical impedance, one can now describe the effect of applying the cantilever tip to the nanomechanical resonator in terms of varying the mechanical impedance experienced by the resonator. To see how this comes about, first consider the system in the absence of the cantilever tip. If the resonator was ideally and completely rigidly clamped (i.e the clamping region completely immobile), all vibrational energy would be reflected at the clamps. The corresponding response would be

$$\delta\hat{q}(\omega) = \frac{\hat{f}_D(\omega)}{m\left[-\omega^2 - i\tilde{\gamma}_0\omega + \tilde{\omega}_0^2\right]},$$

where the damping $\tilde{\gamma}_0$ and frequency $\tilde{\omega}_0$ are the bare (intrinsic) values for the string resonator. The intrinsic damping $\tilde{\gamma}_0$ is thus entirely due to interactions internal to the beam such as defect mediated inelastic scattering of high energy thermal phonons from the resonator mode.

The equation for the mechanical response is homologous to that of a series RLC-resonator with

$$\delta\hat{Q}(\omega) = \frac{\hat{v}_D(\omega)}{L[-\omega^2 - i(R/L)\omega + (LC)^{-1}]},$$

provided we identify $\hat{q}(\omega)$ with the capacitor charge $\hat{Q}(\omega)$, and $\hat{f}_d(\omega)$ with $\hat{v}_D$ the voltage over the resonator as discussed in chapter 3.2.3. In this case one can identify

$$\tilde{\gamma}_0 \sim R/L,\ \tilde{\omega}_0^2 \sim 1/LC,\ m \sim L.$$

If the coupling to the clamps is linear in oscillator coordinate $\hat{q}$, the effect of coupling to the supports is to allow a certain amount of energy to propagate away as well as to renormalize the frequency. In this case the response would be

$$\delta\hat{q}(\omega) = \frac{\hat{f}_D(\omega)}{m[-\omega^2 - i\gamma_0\omega + \omega_0^2]} = \frac{\hat{f}_D(\omega)}{m[-\omega^2 - i\tilde{\gamma}_0\omega + \tilde{\omega}_0^2 - \chi_0(\omega)]},$$

where $\chi_0(\omega) = -(\omega_0^2 - \tilde{\omega}_0^2) - i\gamma\omega + i\tilde{\gamma}\omega$. Making again the analogy with the RLC-circuit, we see that the effect of coupling to the support is to add the mechanical contact impedance $Z_{\mathrm{m}0} = m\chi_0(\omega)/(i\omega)$ to the oscillator, yielding

$$\delta\hat{q}(\omega) = \frac{\hat{f}_D(\omega)}{m[-\omega^2 - i\gamma_0\omega + \omega_0^2]} = \frac{\hat{f}_D(\omega)}{m[-\omega^2 - i\tilde{\gamma}_0\omega + \tilde{\omega}_0^2] - i\omega Z_{\mathrm{m}0}}. \tag{3.17}$$

When the tip is applied, the response function $\hat{\chi}_{\mathrm{tip}}(\omega)$ which is a function of tip position and force also adds. Under the assumption of linear coupling, the impedances are additive and one can write $Z_{\mathrm{m}}(\omega) = Z_{m0}(\omega) + Z_{\mathrm{tip}}(\omega)$ where $Z_{\mathrm{tip}}(\omega) = m\chi_{\mathrm{tip}}(\omega)/(i\omega)$. Hence,

$$\delta\hat{q}(\omega) = \frac{\hat{f}_D(\omega)}{m[-\omega^2 - i\gamma_0\omega + \omega_0^2] - i\omega Z_{\mathrm{tip}}(\omega)}. \tag{3.18}$$

Figure 3.7 schematically illustrates the different systems mentioned above: A rigidly clamped resonator, an elastically clamped resonator and an elastically clamped resonator with applied AFM tip. Also shown are the respective mechanical lumped element models and their respective electrical counterparts. Note again that the mechanical circuits are parallel elements and the respective electrical circuits are series elements, so that in both cases the impedances are additive.

### 3.2.5 Linear model for deflection perpendicular to the surface

The following treats the explicit case of an out-of-plane flexural resonator mode interacting with the AFM-cantilever. In the simplest scenario, the surface in the clamping region only moves in the direction perpendicular to the cantilever. For simplicity it is assumed that the tip contacts the surface perpendicularly.

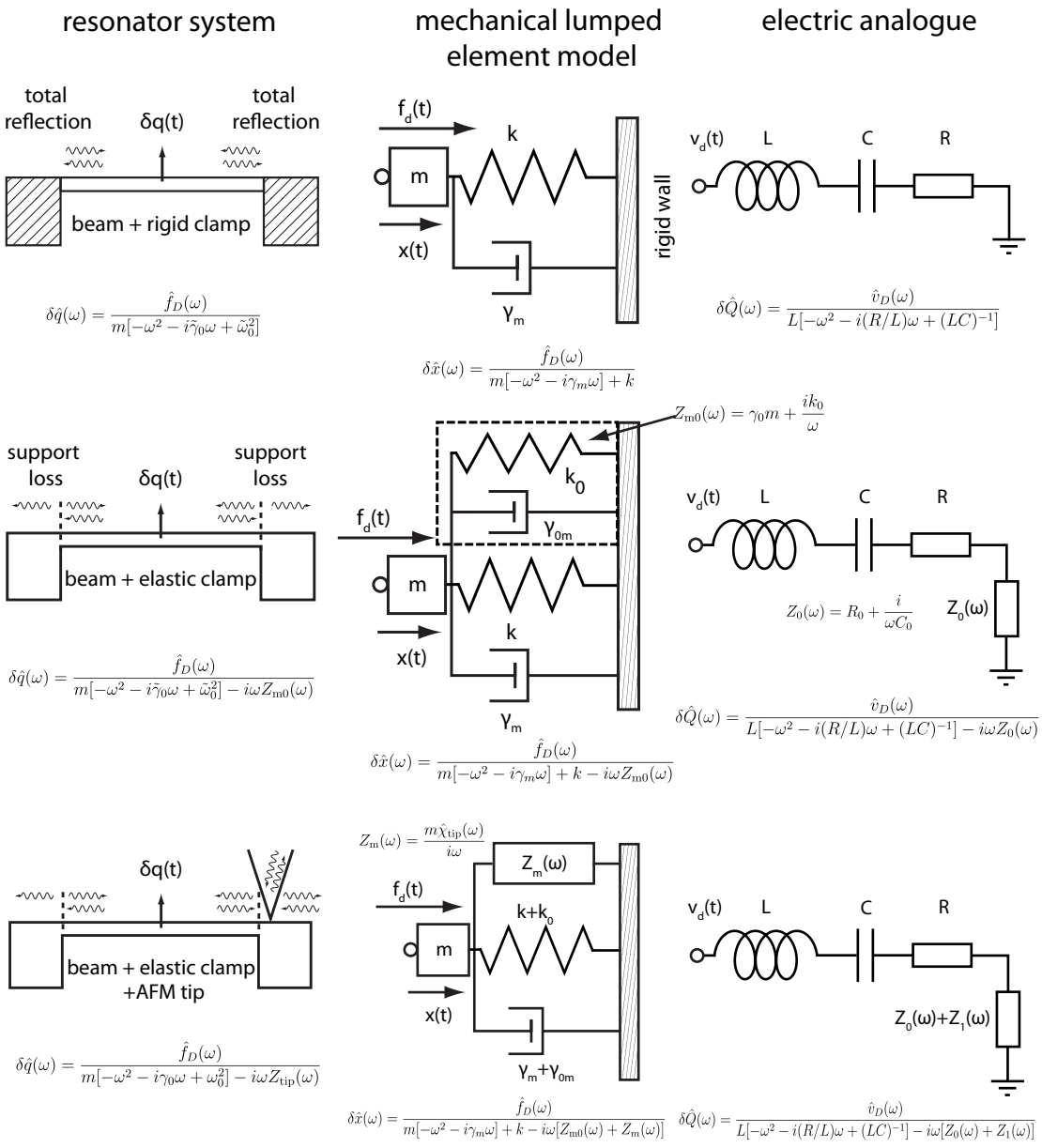


**Figure 3.7:** Illustration of the resonator system, the respective mechanical lumped element model and its electrical analogue.

Quite generally, one expects that for small deformations the dynamic equations describing the motion of the resonator, clamping region and substrate can be described within the framework of linear elasticity. This assumption is valid for vibrational amplitudes which are small, in the sense that geometric nonlinearities leading to Duffing behavior [Ald05] and modal interactions due to nonlinear coupling [Wes10] can be neglected.

Consider, as a starting point that the dynamics of the resonator together with the silicon nitride support are described by Navier's equation, which is a linear equation in the displacement field $\vec{u} = (u, v, w)$,

$$\ddot{\vec{u}} + \hat{\mathcal{L}}\vec{u} = \rho^{-1}\vec{F}_{ext}.$$

The linear operator $\hat{\mathcal{L}}$, representing the time independent part of Navier's equation, obeys the eigenvalue relation

$$\hat{\mathcal{L}}\vec{u}_n = -\omega_n^2\vec{u}_n,$$

where $\vec{u}_n = (u_n, v_n, w_n)$ $(n = 0, 1, 2, ...)$ are orthonormal vibrational mechanical eigenmodes $\langle \vec{u}_n \cdot \vec{u}_m \rangle = \delta_{nm}$. Here the brackets denote the volume integration $\langle ... \rangle = \frac{1}{V}\int ... \, d^3\vec{x}$.

The external force has two components, the first is a body force from the dielectric actuation, $\vec{F}_{\mathrm{ac}}$, while the second comes from the pressure exerted by the AFM tip at the surface (assumed to lie in the plane $z = 0$), $\vec{P}_{\mathrm{tip}}(x, y)\delta(z)$.

Expanding the motion in terms of these eigenmodes, i.e. $\vec{u} = \sum_n q_n(t)\vec{u}_n(x, y, z)$, one finds

$$\left[\ddot{q}_n + \gamma_n\dot{q}_n + \omega_n^2 q_n\right] = f_n(t) - \rho^{-1}\left\langle \vec{u}_n \cdot \vec{P}_{\mathrm{tip}}(x, y)\delta(z)\right\rangle,$$

where $f_n(t) \equiv \rho^{-1}\left\langle \vec{u}_n \cdot \vec{F}_{\mathrm{ac}}\right\rangle$. If the part of the tip interacting with the resonator is small compared to the characteristic length of variations in the mode function $\vec{u}_n$, near the surface, one may assume a $\delta$-function dependence of the interaction. The force from a tip located at $(x_0, y_0)$ is then

$$\left[\ddot{q}_n + \gamma_n\dot{q}_n + \omega_n^2 q_n\right] = f_n(t) - M^{-1}\vec{u}_n(\vec{x}_0) \cdot \vec{F}_{\mathrm{tip}}(\vec{x}_0).$$

The mass $M$ appearing here is the entire physical mass of the resonator including the supports.

If the in-plane components of the mode function $\vec{u}_n$ are small compared to the out-of-plane components, the equation for the resonator becomes

$$\left[\ddot{q}_n + \gamma_n\dot{q}_n + \omega_n^2 q_n\right] = f_n(t) - M^{-1}w_n(\vec{x}_0)F_{\mathrm{tip}}(\vec{x}_0).$$

Here, $w_n(\vec{x}_0)$ is the normal mode vertical displacement of the surface at the position $\vec{x}_0 = (x_0, y_0)$ of the tip.

The mass $M$ occurring in the last equations stems from the choice of normalization of mode functions. For the resonator in the experiments described here, the mode functions

are highly localized and closely resemble those of a string (see e.g. [Unt10a]). For flexural out-of-plane modes $w_n \propto \cos(n\pi x/L)$, the overall normalization will thus ensure that the mass $M$ gets replaced by the effective mode mass (see section 3.2.6 for the full definition) $m_n \approx \rho V_{\mathrm{res}}/2$ where $V_{\mathrm{res}}$ is the volume of the suspended part of the resonator (see section 3.2.6 below).

### 3.2.6 Tip-surface interaction

To find expressions for the frequency shift and additional damping of a resonator mode caused by the tip from the surface forces, assume a model as the one outlined in Fig. 3.8. If the tip-induced indentation into the substrate is $\delta(F_0 + \Delta F(t)) \approx \delta_0 + g^{-1}\Delta F(t)$, one has

$$q_n(t)w_n(\vec{x}_0) + l_0 + R - \delta_0 - g^{-1}\Delta F(t) - \int_{-\infty}^{t} dt'\,\eta(t-t')[F_0 + \Delta F(t')] = \mathrm{const.}$$

Fourier transforming the time varying part gives

$$\hat{q}_n(\omega)w_n(\mathbf{x}_0) - g^{-1}\Delta\hat{F}(\omega) - \hat{\eta}(\omega)\Delta\hat{F}(\omega) = 0.$$

Hence, the response of the beam when in contact with the tip is

$$\hat{q}_n(\omega) = \frac{\hat{f}_n(\omega)}{(\omega_n^2 - \omega^2) - i\gamma_n\omega + \frac{gw_n^2}{M(g\hat{\eta}(\omega)+1)}} \equiv \frac{\hat{f}_D(\omega)}{m_n[-\omega^2 - i\gamma_n\omega + \omega_n^2] - i\omega Z_{\mathrm{tip}}(\omega)}.$$

Using the mode shape of a string one finds $w_n^2/M \approx \left[w_n(\mathbf{x}_0)/w_n^{\max}\right]^2/m_n = \epsilon_n^2(\vec{x}_0)/m_n$, where $w_n^{\max}$ is the displacement at an antinode of the resonator and

$$m_n = \rho\int d^3\vec{x}\,\left|\frac{\vec{u}_n(\vec{x})}{\vec{u}_n^{max}}\right|^2 = \rho\int d^3\vec{x}\,\epsilon_n(\vec{x})^2 \approx \rho V_{\mathrm{res}}/2$$

is the effective resonator mode mass given by integrating over the squared normalized resonator amplitude $\epsilon_n(\vec{x})$, i.e. the amplitude of the local surface deformation divided by its maximum value at an antinode of the string. The harmonics of a string all have an effective mass of half the resonator mass. Hence the effective mass $m_n$ will hereafter be written as $m$ without index for all modes. The new, perturbed resonance frequency $\omega_{\mathrm{pert}}$ is related to the old one as

$$\omega_{\mathrm{pert}}^2 = \omega_n^2 + \mathrm{Re}\left[\frac{g\epsilon_n(\vec{x}_0)^2}{m(g\hat{\eta}(\omega)+1)}\right].$$

Introducing the contact impedance

$$Z_{\mathrm{tip}}(\omega,\vec{x}_0,n) = -\frac{i}{\omega_n}\frac{g\,\epsilon_n^2(\vec{x}_0)}{(g\hat{\eta}(\omega)+1)}, \tag{3.19}$$

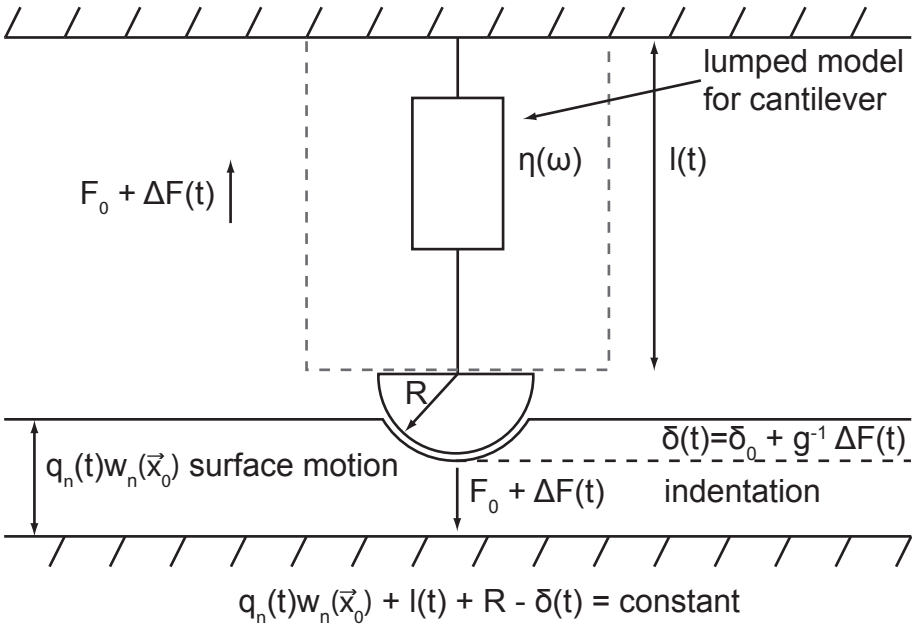


**Figure 3.8:** Sketch of the contact interaction model, visualizing the time varying force $F_0 + \Delta F(t)$, the tip radius R, the tip-induced indentation $\delta(t)$, the surface motion $q_n(t)w_n(\vec{x}_0)$, and the length $l(t) = l_0 - \int_{-\infty}^{t} dt'\,\eta(t-t')[F_0 + \Delta F(t')]$.

the frequency shift $\delta\omega = \omega_{\mathrm{pert}} - \omega_n$ is given by

$$\delta\omega \approx \mathrm{Re}\left[\frac{g\epsilon_n^2(\vec{x}_0)}{2m\omega_n(g\hat{\eta}(\omega_n)+1)}\right] = \frac{\mathrm{Im}[\mathrm{Z_{tip}}]}{2\,m}. \tag{3.20}$$

Correspondingly, the new dissipative part of the response is now given by

$$\gamma_{\mathrm{pert}} \approx \gamma_n - \mathrm{Im}\left[\frac{g\epsilon_n^2(\vec{x}_0)}{m\omega_n(g\hat{\eta}(\omega_n)+1)}\right] = \gamma_n + \frac{\mathrm{Re}[\mathrm{Z_{tip}}]}{m}. \tag{3.21}$$

Thus the real and imaginary parts of $Z_{\mathrm{tip}}$ relate to the additional damping $\delta\gamma = \gamma_{\mathrm{pert}} - \gamma_n$ via $\mathrm{Re}[Z_{\mathrm{tip}}] = m\,\delta\gamma$ and the frequency shift via $\mathrm{Im}[Z_{\mathrm{tip}}] = 2m\,\delta\omega$. The results in eqs. (3.20) and (3.21) rest on the assumptions that the relative shift in frequency is small and that the AFM-cantilever response in this frequency range is constant, i.e. $\hat{\eta}(\omega) \approx \hat{\eta}(\omega_n)$ for $\omega \in [\omega_n, \omega_n + \delta\omega]$.

There are several models for tip surface interaction, see e.g. [But05]. The simplest being the ordinary Hertz-theory where the indentation $\delta$ is related to the applied force $F$ as

$$\delta_{\mathrm{Hz}} = \left(\frac{9F^2}{16RE_{\mathrm{eff}}^2}\right)^{1/3}.$$

The tip radius is denoted by $R$ while the effective Young's modulus is defined as

$$\frac{1}{E_{\mathrm{eff}}} = \frac{1-\nu_1^2}{E_1} + \frac{1-\nu_2^2}{E_2}.$$

Here the $E_i$ are the Young's moduli and the $\nu_i$ are the Poisson's ratios of the materials in contact. Due to the presence of adhesive forces, $F_{\mathrm{ad}}$, the Hertzian theory does not fit well with the measured data. However, both the Johnson-Kendall-Roberts (JKR) as well as the Derjaguin-Muller-Toporov (DMT) model give very good fits. For a more detailed description of these interaction models see e.g. [But05].

Using the DMT theory and introducing $g_0 = (6F_{\mathrm{ad}}E_{\mathrm{eff}}^2R)^{1/3}$ the coupling constant $g$ can be expressed as

$$g = g_0(1 + F/F_{\mathrm{ad}})^{1/3}. \tag{3.22}$$

## 3.3 Force dependent measurements

To confirm the validity of the model equations 3.18 and 3.19, the force dependence of $Z_{\mathrm{tip}}$, contained in the coupling $g$ in equation 3.19 was studied by recording force-distance curves at different tip positions. As the local normalized resonator amplitude $\epsilon_n(\vec{x}_0)$ varies for these positions, so do the frequency shift and induced damping for a given force. However, the linear theory predicts that all curves can be scaled to coincide with each other. Thus an entire dataset of frequency shift and damping for multiple positions can be fitted with a single set of parameters, where $\epsilon_n(\vec{x}_0)$ enters the fit routine as the scaling factor for the respective curve, and the real and imaginary part of the tip response function $\hat{\eta}$ constitute the only two global fitting parameters. Figure 3.9 shows the outcome of such a measurement and the fit of our model for a resonator with an unperturbed resonance frequency of $f_0 = 6.65\,\mathrm{MHz}$ and damping rate of $\gamma_0$ =173 $\mathrm{s}^{-1}$. Here the force-distance curves were measured for three different tip positions in the clamping region, indicated by color. The rescaled data show very good quantitative agreement with the model. The detailed shape of the curves depend on the contact model used and good agreement with the employed DMT-model is found. As described in section 3.2.6, the coupling constant $g$ that enters the frequency shift and damping is given by equation 3.22. The presented data are taken from the retraction part of the force distance curves up to the point where the snap out of contact appears. Very similar results can be obtained with the approach curves, but with a restricted accessible range of forces.

To enable simultaneous fitting of all curves the following procedure is employed: First, the data are aligned sequentially along the force axis. Subsequently, the fitting function is defined as a piecewise function along this axis by shifting the zero-point of the model to the respective minimal force value of each data curve. This way, datasets for multiple measurement points can be adjusted with a single fit. After the nonlinear regression has been executed, the data can be rescaled by the fitted $\epsilon_n(\vec{x}_0)$, and the force axes are restored to the original, actual forces.

The system parameters (obtained idependently, i.e. not fitted) used in this fit routine are as follows:

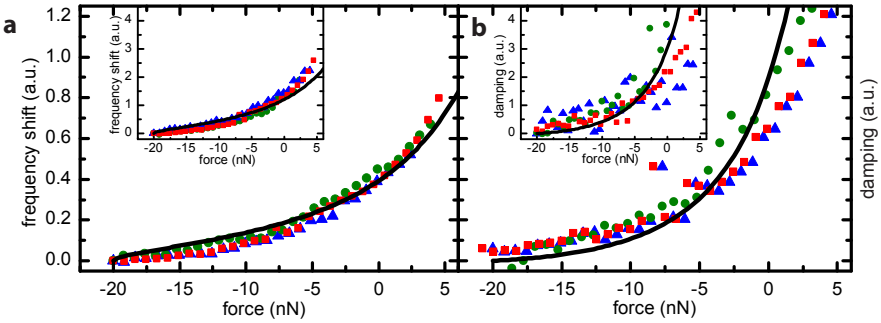


**Figure 3.9:** Force dependence of frequency shift and damping. Force-distance curves are measured at three points in the clamping region (red squares, green dots, blue triangles) with increasing distance to the resonator. Since a linear response theory is valid, all curves can be scaled to coincide with each other. Thus the model can be fitted to the whole dataset, i.e. all frequency shift and damping curves, with one single set of parameters. For clarity, only the retraction curves are shown. In all panels red squares represent the data for the point of highest interaction (closest to the clamp), green dots for an intermediate and blue triangles for the point of lowest interaction. (**a**) Force dependence of the frequency shift of the fundamental out-of-plane mode with a free resonance frequency of 6.65 MHz. The solid black line is a fit of the model. The inset shows the data and fitted model of the third harmonic mode with a free resonance frequency of 20.0 MHz, which was measured simultaneously. (**b**) Force dependence of the tip induced damping for the same modes, including fit as solid line.

| | | |
|---|---|---|
| Effective mass | m | $2.07 \cdot 10^{-15}$ kg |
| Adhesion force (measured) | $F_{ad}$ | 20 nN |
| Young's modulus silicon nitride | $E_{SiN}$ | 250 GPa |
| Young's modulus silicon | $E_{Si}$ | 200 GPa |
| Poisson's ratio silicon nitride | $\nu_{SiN}$ | 0.27 |
| Poisson's ratio silicon | $\nu_{Si}$ | 0.22 |
| Tip radius (measured in SEM) | R | 80 nm |
| Cantilever force constant | $k_{ca}$ | 0.05 nN/nm |

Furthermore, the cantilever spring constant of the silicon contact mode cantilever was calibrated using the procedure described in 2.1.2 and the Young's moduli and Poisson's ratios are literature values [Sha10]. Finally, the fit parameters for the fundamental out-of-plane mode and its third harmonic are the following:

| Mode | $\mathrm{Re}[\hat{\eta}]$ | $\mathrm{Im}[\hat{\eta}]$ | $\epsilon_{n,1}$ | $\epsilon_{n,2}$ | $\epsilon_{n,3}$ |
|---|---|---|---|---|---|
| Fund., $n = 0$ | -510 $(\mathrm{N/m})^{-1}$ | -15 $(\mathrm{N/m})^{-1}$ | $2.1 \cdot 10^{-4}$ | $3.2 \cdot 10^{-4}$ | $3.7 \cdot 10^{-4}$ |
| 3rd harm., $n = 2$ | -518 $(\mathrm{N/m})^{-1}$ | -19 $(\mathrm{N/m})^{-1}$ | $4.0 \cdot 10^{-4}$ | $6.5 \cdot 10^{-4}$ | $6.8 \cdot 10^{-4}$ |

For the three curves of the fundamental resonance presented in Fig. 3.9, the maximal values of the frequency shift are: $\delta f_{0,1} = 220\,\mathrm{Hz}$, $\delta f_{0,2} = 405\,\mathrm{Hz}$, and $\delta f_{0,3} = 799\,\mathrm{Hz}$. In the case of the third harmonic mode, the shifts are $\delta f_{2,1} = 725\,\mathrm{Hz}$, $\delta f_{2,2} = 1484\,\mathrm{Hz}$, and $\delta f_{2,3} = 2600\,\mathrm{Hz}$. The values for the $\epsilon_{n,i}$ are of the order of $10^{-4}$ as predicted by *Comsol* simulations (c.f. section 3.4). As expected from eq. (3.20), the values of the local normalized resonator amplitudes $\epsilon_{n,i}$ increase for the curves with a higher frequency shift.

Moreover, the real and imaginary part of the tip response function do not change for the two modes, signifying that the assumption of a quasi-continuum of cantilever states is justified. This in turn means that the presented method of mechanical impedance mismatch imaging is not restricted to certain frequencies coinciding with cantilever resonances. Thus the procedure is in principle applicable to all kinds of nanomechanical systems.

## 3.4 Position-dependent impedance mismatch

To further investigate the dependence of the contact impedance $Z_{\mathrm{tip}}$ on the local normalized resonator amplitude $\epsilon_n(\vec{x}_0)$ as described by equation 3.19, impedance maps for the fundamental ($n$ = 0) out-of-plane and in-plane mode of the resonator were measured and the obtained data compared with *Comsol* finite element simulations of $\epsilon_0^{\perp}(\vec{x}_0)^2$ (out-of-plane) and $\epsilon_0^{\parallel}(\vec{x}_0)^2$ (in-plane) (Fig. 3.10). Again, the measurements were conducted on a grid in the vicinity of the resonator clamping region with the AFM tip exerting a constant force. The impedances were then calculated from the induced damping $\mathrm{Re}[Z_{\mathrm{tip}}] = m\,\delta\gamma_n$ and the frequency shift $\mathrm{Im}[Z_{\mathrm{tip}}] = 2m\,\delta\omega_n$ as given by equation 3.20 and equation 3.21. The data for the out-of-plane mode in Fig. 3.10a,b stem from the same measurement as the frequency shift and damping presented in Fig. 3.2. The real part of the contact impedance for the in-plane-mode presented in Fig. 3.10c was measured on a different resonator with an unperturbed resonance frequency of 6.82 MHz, a damping rate of 357 $\mathrm{s}^{-1}$ and zero cantilever deflection. Furthermore this measurement was performed using a triangular silicon nitride cantilever.

Comparing the spatial contact impedance profiles with the simulated local resonator amplitudes displayed in Fig. 3.10d-f convincingly shows that the experimental data can be qualitatively well reproduced by the simulations. However, the exact shape of the amplitude profile strongly depends on the microscopic clamping region geometry. As the last step of the fabrication process is an isotropic hydrofluoric wet etch of the fused silica substrate to obtain freely suspended strings [Fau12a], a small part of the rectangular silicon nitride pedestal acting as clamp becomes underetched as well. This in turn has a large effect on the local amplitude, which is demonstrated by the simulated $\epsilon_0^{\perp}(\vec{x}_0)^2$ of the out-of-plane mode for a clamp with a realistic, 500 nm deep undercut in Fig. 3.10d. It shows excellent qualitative agreement with Fig. 3.10b, whereas a clamp with no undercut at all in Fig. 3.10e shows considerably poorer agreement with the data. Fig. 3.10f displays the local amplitude of the in-plane-mode, again in excellent correspondence with the shape of the measured data (Fig. 3.10c). For the in-plane mode, a linear analysis analogous the one performed for the out-of-plane mode can be made, which again results in a local mechanical impedance modification proportional to $\epsilon_0^{\parallel}(\vec{x}_0)^2$.

Mapping of the contact impedance can not only be performed for the fundamental flexural modes ($n$ = 0), but also for higher harmonics. As an example, a measurement for the third harmonic ($n$ = 2, $f_2 \approx 3\ f_0$) out-of-plane mode of a resonator with an unperturbed resonance frequency of $\mathrm{f}_2 = 19.8$ MHz and a quality factor of $\mathrm{Q}_2$ =150 000 is shown in

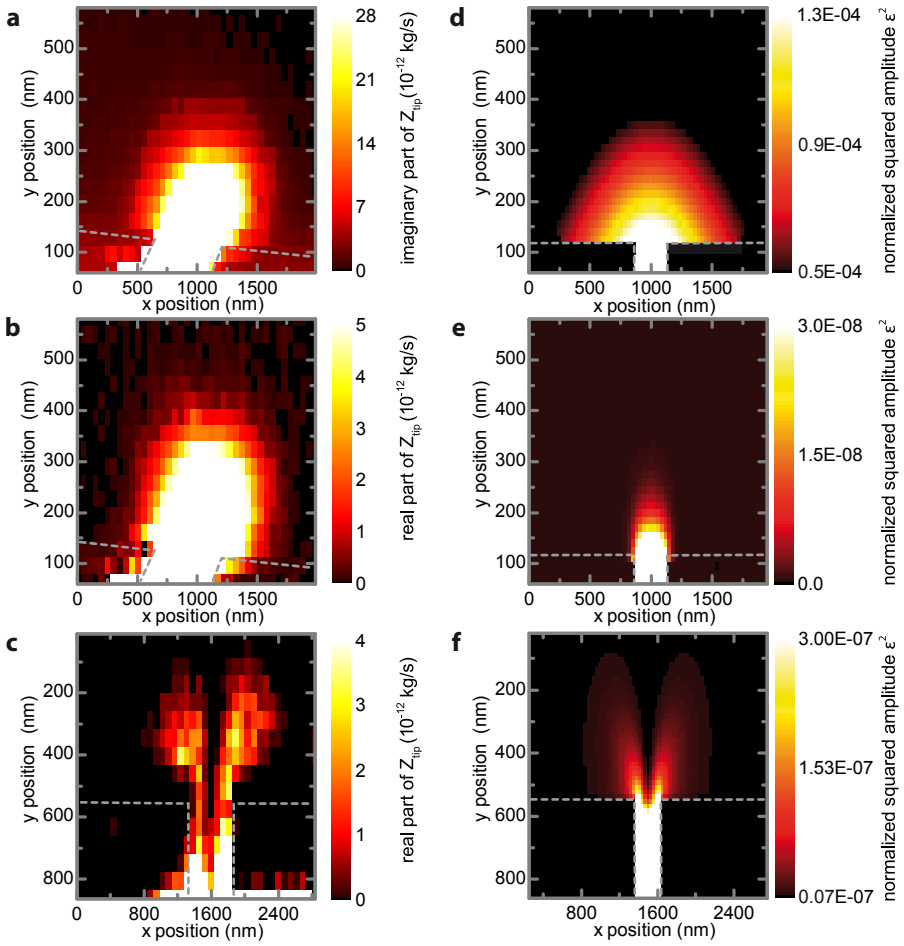


**Figure 3.10:** Experimentally determined contact impedance maps **a-c** and simulated local amplitudes of the clamping region **d-f** for the fundamental out-of-plane (**a,b,d,e**) and in-plane (**c,f**) mode. **a** Imaginary part of the contact impedance $Z_{tip}$for the out-of-plane mode. **b** Real part of the contact impedance for the out-of-plane mode. **c** Real part of the contact impedance for the in-plane mode. **d** Simulated normalized squared amplitude $\epsilon_0^{\perp}(\vec{x}_0)^2$ for the out-of-plane mode. Here the undercut of the silicon nitride pedestal has been set to a realistic value of 500 nm. **e** The same simulation for a clamp with no undercut. **f** Simulated $\epsilon_0^{\parallel}(\vec{x}_0)^2$ for the fundamental in-plane-mode with 500 nm undercut.

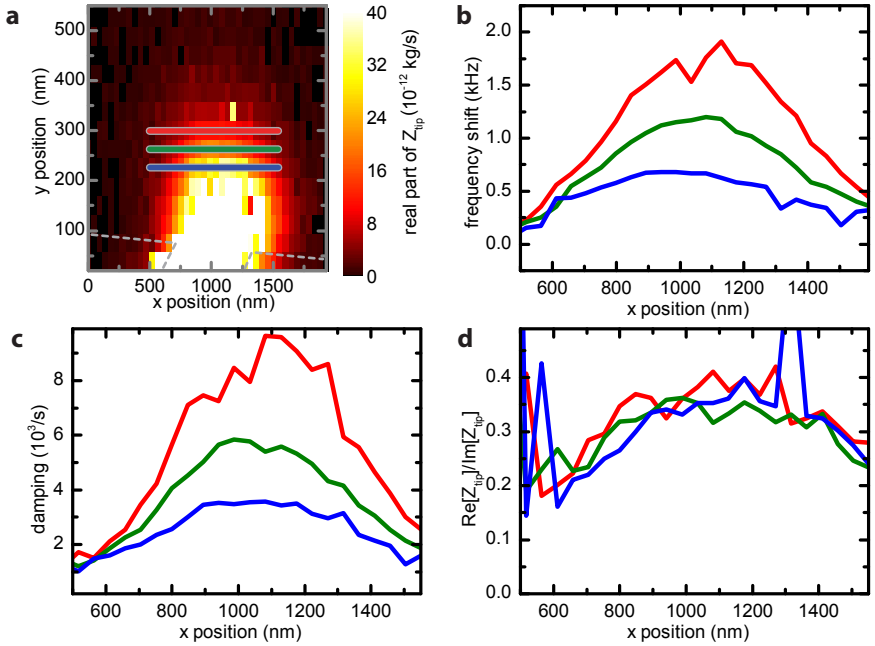


**Figure 3.11:** Contact impedance measurement for the third harmonic out-of-plane mode as well as tip induced frequency shift and damping. **a** Real part of the contact impedance. The resonator outlines are depicted as gray dashed lines. **b** Shift of the resonance frequency with tip position along three lines specified in **a**. The data and the respective tip positions are color coordinated. **c** Damping rate versus tip position for the same line cuts. **d** The theoretical model predicts the ratio of real- and imaginary part of the contact impedance to be an invariant. This ratio has been computed from the measured frequency shift and damping curves in **b** and **c**. As theoretically predicted, the numerical values agree with the ones found for the fundamental mode.

Fig. 3.11. A constant force of 9.2 nN was applied to the AFM-tip, which is the same force as in the constant force measurements on the fundamental out-of-plane mode in Fig. 3.2 and Fig. 3.10a. The results presented in Fig. 3.11 show that a very similar outcome as for the fundamental mode is obtained. However, the effect of absolute frequency shift and damping and thereby the contact impedance for a given force is larger for a mode with a higher frequency. Note that the relative frequency shift for the different modes stays the same, since the tip response function does not change with frequency as shown in the force dependent measurements in section 3.3. Furthermore, the ratio of real- and imaginary part of the contact impedance is not only independent of position, but also has the same numerical value as for the fundamental mode. This is consistent with the theoretical description of eqs. (3.20) and (3.21), because $\mathrm{Re}[Z_{\mathrm{tip}}]/\mathrm{Im}[Z_{\mathrm{tip}}]$ does not depend on frequency for a constant $\hat{\eta}$ and the same force was applied in both measurements. In addition, an estimate of this ratio with the parameters obtained from the force measurements gives a value of 0.2 for the fundamental and the third harmonic, in accordance with the experimental results.

## 3.5 Impedance mismatch and dissipation in nanomechanical systems

Quite generally, one can discriminate between two types of energy loss mechanisms in nanomechanical systems. On the one hand there is the effect of internal friction, which solely depends on the material make-up of the resonator. On the other hand, energy can be radiated into the support structure of the resonator, i.e. the substrate. This dissipation channel is referred to as clamping losses [WR08] and strongly depends on the resonator geometry [WR11]. In the phonon tunneling approach that is used to model this dissipation [Col11], it is assumed that a phonon residing on the resonator is converted into a propagating substrate phonon of equal frequency.

As discussed in chapter 2.2, the silicon nitride string resonators exhibit higher quality factors than unstressed resonators, because the stored elastic energy is increased by the tensile stress, whereas the damping remains approximately constant [Unt10a]. This damping due to internal friction can be phenomenologically understood within a Zener model [Zen38], where the displacement induced strain and stress are not in phase and the out-of-phase component is modeled by an imaginary Young's modulus. Such a complex Young's modulus can be introduced in any system that features relaxation processes caused by point defects [Now65]. Interestingly, this inelastic and the dielectric relaxation can be treated within the framework of this model. For the dielectric case, this leads to a complex polarizability as used in chapter 2.3 to model the dielectric damping. The defect states causing the internal mechanical friction in (amorphous) silicon nitride strings as presented in Ref. [Unt10a] can indeed not be related to a specific microscopic model up to now, but are identified to be the most significant source of damping in this system. Other damping mechanisms, such as thermoelastic damping [Lif00] and Akhiezer damping [Kis08, Kun11] can be safely neglected.

Also, the clamping losses mentioned above are found to be of no significance for the silicon nitride resonators investigated in Ref. [Unt10a]. In a more recent study, mode dependent clamping losses of silicon nitride membranes subject to tensile stress could be identified [WR11]. For the one dimensional case of the reasoning presented there, the clamping loss limit for the Q factor is given by the formula [WR12]

$$Q_{\mathrm{clamp}} = 0.07\sqrt{\frac{\rho_{\mathrm{res}}}{\rho_{\mathrm{sub}}}}\left(\frac{E_{\mathrm{sub}}}{\sigma_0}\right)\frac{L^2}{wt}, \tag{3.23}$$

where $\rho_{\mathrm{res}}$ and $\rho_{\mathrm{sub}}$ are the densities of the resonator and the substrate, $E_{\mathrm{res}}$ and $\sigma_0$ designate the Young's modulus and the tensile stress of the resonator and $L$, $w$ and $t$ are the length, width and thickness of the resonator. For the resonators used in this work, equation 3.23 gives a value of $Q_{\mathrm{clamp}} = 2.9 \cdot 10^6$ for the clamping loss limited Q factor. With a value of 350 000, the highest achieved Q factors are still one order of magnitude smaller as to be limited by this dissipation mechanism.

In the terminology of impedance mismatch, clamping losses can be described by adding a mechanical impedance $Z_{0\mathrm{m}}$ as discussed in chapter 3.2.4 and illustrated in

Fig. 3.7. Even though these "internal" clamping losses are not the dominant dissipation mechanism in the nanomechanical resonators used in this work, so that $Z_{0\mathrm{m}}$ is not experimentally accessible, energy radiation quickly becomes highly relevant when applying the AFM tip and thereby adding the contact impedance $Z_{\mathrm{tip}}$. By position and force dependent measurements as presented in chapter 3.4 and 3.3, one can observe the transition of a high-Q to a low-Q resonator. As the respective resonator does not change in these measurements, the intrinsic damping remains constant, and the additional damping is only caused by energy radiated into the AFM cantilever, showing that elastic energy radiation can be an extremely significant dissipation mechanism.

In terms of intrinsic friction, the impedance matching of the resonator can also be of importance. The heat caused by internal friction has to be able to flow out of the resonator. High frequency phonons are responsible for this heat conduction. One can now interpret the annihilation of a resonator phonon as a defect mediated inelastic scattering process with a high frequency phonon. This scattering has to conserve energy and momentum. Energy conservation leads to a final frequency $\omega_p + \omega_{\mathrm{res}}$ of the scattered phonon with an initial frequency $\omega_p$. Here the resonator mode frequency is $\omega_{\mathrm{res}}$. Momentum conservation can be lifted by a scattering process which is mediated by a (delta like) point defect. High frequency phonons, i.e. phonons with much smaller wavelength than propagating phonons with the resonator frequency (at the sound velocity in quartz glass of $\approx 5000$ m/s at a frequeny of 10 MHz this wavelength is $\approx 500\,\mu$m) do not experience a high impedance mismatch and can leave the resonator much more easily.

# Chapter 4

# Coupled systems and AFM manipulation

As described in chapter 2.3, in the "elevated" electrode geometry, the out-of-plane and the in-plane mode can be tuned in different directions in frequency space. When applying a dc voltage, the in-plane mode tunes downwards in frequency, whereas the out-of-plane mode tunes upwards. Initially, i.e. for zero dc bias, the in-plane mode has a higher resonance frequency than the out-of-plane mode for a 260 nm wide and 100 nm thick string. This is a consequence of the rectangular cross section of the string resulting in a higher rigidity for the in-plane oscillation direction. Thus the two modes can be tuned into resonance at a common frequency. Around the zero detuning point, a pronounced avoided crossing due to a coupling of the two modes can be observed. This chapter describes the coupling mechanism, and the basic differential equations governing the system dynamics. The mode shapes resulting from the solutions of these equations in the avoided crossing are discussed for realistic parameters. Then, position dependent AFM measurements are presented that visualize the change of the mode shapes when the modes are tuned through the avoided crossing. Finally, tuning speed dependent measurements, which represent the classical analogon of Landau-Zener transitions are discussed.

## 4.1 Coupling of in- and out-of-plane modes

To commence the analysis of coupled nanomechanical resonator modes, consider the differential equations for two linearly coupled, damped harmonic oscillators. For the displacements $q_n$ (n=1,2) these are:

$$m\frac{d^2q_1}{dt^2} + m\gamma_1\frac{dq_1}{dt} + k_1q_1 + k_c(q_1 - q_2) = 0 \tag{4.1}$$

$$m\frac{d^2q_2}{dt^2} + m\gamma_2\frac{dq_2}{dt} + k_2q_2 + k_c(q_2 - q_1) = 0, \tag{4.2}$$

with the effective mass $m$, the spring constants $k_n$, the coupling constant $k_c$ and the two different damping constants $\gamma_n$. The coupling constant can be expressed as the derivative of the force $F_n$ along one coordinate with respect to the other.

$$\frac{\partial F_1}{\partial q_2} = \frac{\partial F_2}{\partial q_1} = k_c. \tag{4.3}$$

The force on a (dielectric) nanomechanical resonator caused by an external electric field $\vec{E}$ is determined by the gradient of the energy (cf. chapter 2.3):

$$\vec{F}_{\mathrm{el}} = -\vec{\nabla} W = -\vec{\nabla}\left(\vec{p}\cdot\vec{E}\right) = -\vec{\nabla}\left(\alpha E^2\right) \tag{4.4}$$

Here $\alpha$ is the polarizability, and $\vec{p}$ the dipolar moment. As stated in chapter 2.3, the silicon nitride string resonators exhibit two orthogonal, almost frequency degenerate flexural modes. These are the out-of-plane oscillation perpendicular to the substrate and the in-plane oscillation parallel to it. Taking the out-of-plane direction as the y-axis, and the in-plane direction as the x-axis, the derivative of the x (or y) component of $\vec{F}_{\mathrm{el}}$ with respect to y (or x) results in a dielectric coupling term

$$\frac{\partial}{\partial y}\left(-\frac{\partial \alpha E^2}{\partial x}\right) = -\alpha\frac{\partial^2 E^2}{\partial y \partial x} = -\alpha\frac{\partial^2 E^2}{\partial x \partial y} = k_{c,el} \tag{4.5}$$

Thus non vanishing mixed partial derivatives of the electric field lead to a coupling of the out-of-plane and the in-plane mode. As there is a gradient of the electric field in y direction (the electrodes are above the beam) and in x direction (from asymmetry, otherwise the in-plane mode would not tune with the applied dc voltage), $k_{c,el}$ is not zero. This is visualized in Fig. 4.1, which shows equipotential lines along the resonator cross section obtained from *COMSOL* finite element simulations. If the beam is not perfectly aligned between the two electrodes, the resulting effective electric field exhibits a gradient in x and y direction.

In chapter 2.3 it is shown that in the elevated electrode design, the out-of-plane mode tunes to higher frequencies with increasing dc bias, whereas the in-plane mode tunes to lower frequencies. At zero dc voltage, the resonance frequency of the in-plane mode is slightly higher than the resonance frequency of the out-of-plane mode. This frequency difference is of the order of ≈100 kHz. It is a consequence of the rectangular cross section of the beam (270 nm x 100 nm), resulting in a higher rigidity for the in-plane direction. Despite the resonance frequency being dominated by the tensile stress [Unt10a], this bending contribution leads to the slight frequency difference. So with this initial situation, by increasing the dc bias, the two modes can be tuned into resonance at a common frequency.

As the modes are tuned through the zero detuning point, a characteristic avoided crossing can be observed. A typical measurement of such an avoided crossing around a frequency of 6.63 MHz is shown in Fig. 4.2. Here, the driven response of the two modes was measured for increasing dc voltage. By a Lorentzian fit to each of the branches, the

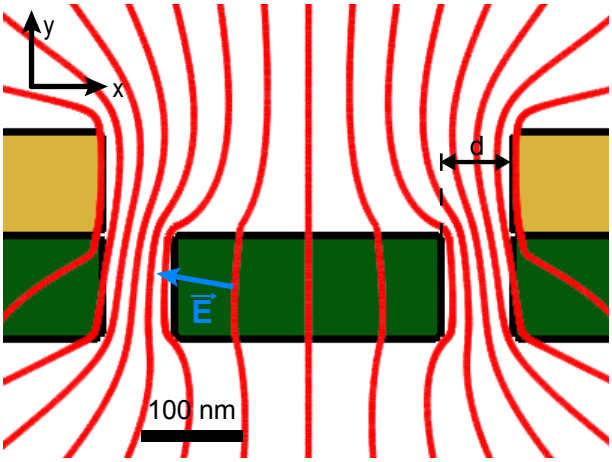


**Figure 4.1:** The red lines of equal electric potential between the two electrodes (calculated using *COMSOL* finite element simulation) demonstrate the inhomogeneous electric field (blue arrow) in x as well as y direction for an "elevated" electrode configuration (cf. chapter 2.3).

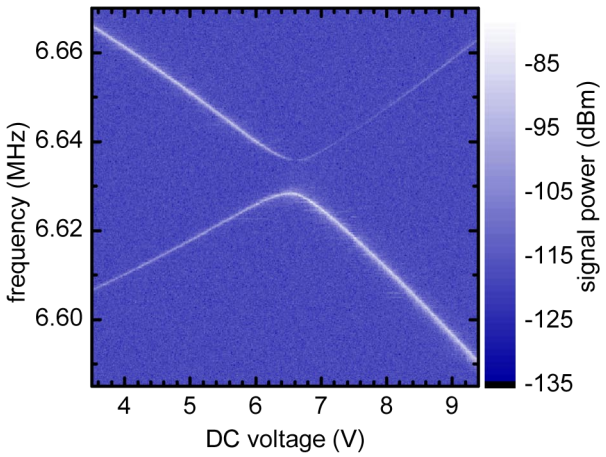


**Figure 4.2:** The two mechanical modes are tuned in opposite direction as the dc voltage that is applied to the electrodes is increased. The signal power is displayed in a color-coded plot versus dc voltage and drive frequency. A pronounced avoided crossing between the two modes is clearly visible.

resonance frequencies and quality factors for each dc voltage can be extracted.

To theoretically model the frequency and damping behavior of the two branches in the avoided crossing region, the differential equations 4.1 and 4.2 have to be solved. This can be accomplished by using an oscillatory ansatz $q_n = a_n e^{i\omega t}$. Inserting this ansatz into equations 4.1 and 4.2 yields

$$-\omega^2 m a_1 + k_1 a_1 + k_c(a_1 - a_2) + im\omega\gamma_1 a_1 = 0 \tag{4.6}$$
$$-\omega^2 m a_2 + k_2 a_2 + k_c(a_2 - a_1) + im\omega\gamma_2 a_2 = 0. \tag{4.7}$$

This can be rewritten as

$$\begin{pmatrix} -\omega^2 m + im\omega\gamma_1 & 0 \\ 0 & -\omega^2 m + im\omega\gamma_2 \end{pmatrix}\vec{a} + \begin{pmatrix} k_1 + k_c & -k_c \\ -k_c & k_2 + k_c \end{pmatrix}\vec{a} = 0 \tag{4.8}$$
$$\boldsymbol{\Omega}\vec{a} + \boldsymbol{K}\vec{a} = 0 \tag{4.9}$$

using $\vec{a} = \begin{pmatrix} a_1 \\ a_2 \end{pmatrix}$ and by defining the two matrices $\boldsymbol{\Omega}$ and $\mathbf{K}$. By solving the eigenvalue problem

$$\boldsymbol{\Omega}^{-1}\boldsymbol{K}\vec{a} = \lambda\vec{a} \tag{4.10}$$

one can obtain two (rather complicated) analytical solutions. The real part of the eigenvalues contains the frequencies while the imaginary part describes the damping constants of the two branches. The eigenvalue problem is solved using Wolfram mathematica.

By employing the described ansatz one effectively diagonalizes the problem, i.e. transforms to a coordinate system in which the equations 4.1 and 4.2 decouple. The corresponding matrix is then diagonal in the basis given by the eigenvectors. These eigenvectors thus represent the normal coordinates of the problem. For the case of zero detuning without damping, the normal coordinates are well known and are obtained by simply adding or subtracting the initial coordinates [Nov10]: $N_1 = x + y$ and $N_2 = x - y$. Thereby one obtains an in-phase and an out-of-phase combination of the original coordinates with frequencies $\omega_1 = \sqrt{\frac{k}{m}}$ and $\omega_2 = \sqrt{\frac{k+2k_c}{m}}$. In the general case described by the eigenvalue problem in equation 4.10, i.e. the case of different damping and spring constants, the normal coordinates are also linear combinations of the original coordinates $n_i = \alpha_i x + \beta_i y$ $(i = 1, 2)$. In the presence of damping, the constants $\alpha_i$ and $\beta_i$ are generally complex numbers and are given by the components of the eigenvectors which have to be normalized so that $|\alpha_i|^2 + |\beta_i|^2 = 1$. The normal coordinates are thus a combination of the original out-of-plane (y) and in-plane (x) direction with different magnitude and phase. Consequently the mode shapes when regarded along the cross section of the beam (cf. Fig. 4.1) are Lissajous figures as shown below. Solving the eigenvalue problem and transforming to the momentary normal coordinates is done with Wolfram mathematica. A commented mathematica notebook describing this procedure can be found in Appendix C.

The two solutions of equation 4.10 can be simultaneously fitted to the frequencies and quality factors obtained from the measurement of the avoided crossing. The spring

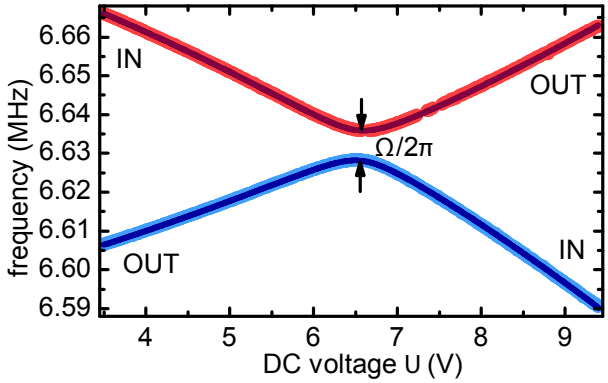


**Figure 4.3:** The frequency of the upper (red) and lower (blue) branch of the avoided crossing versus dc voltage U. Each data point represents a value extracted from a Lorentzian fit of the data shown in Fig. 4.2. The solid lines are a fit of the model, i.e. the frequencies corresponding to the real part of the eigenvalues obtained from the eigenvalue problem described by equation 4.10. IN and OUT denote the in- and out-of-plane mode of the beam.

constants are approximated by $k_n = k_0 + \kappa_n(U - U_0) + \lambda_n(U - U_0)^2$. This is a second order series expansion of the parabolic frequency tuning [Unt09, Rie12] (cf. chapter 2.3) around the crossing voltage $U_0$. The eigenfrequencies extracted from the avoided crossing in Fig. 4.2 as well as a fit of the model are shown in Fig. 4.3. It yields the following values for the fit parameters: $k_0 = 3.2\,\frac{\mathrm{N}}{\mathrm{m}}$, $\kappa_1 = 9.3 \cdot 10^{-3}\,\frac{\mathrm{N}}{\mathrm{Vm}}$, $\kappa_2 = -12.5 \cdot 10^{-3}\,\frac{\mathrm{N}}{\mathrm{Vm}}$, $\lambda_1 = 0.41 \cdot 10^{-3}\,\frac{\mathrm{N}}{\mathrm{V^2m}}$, $\lambda_2 = -0.57 \cdot 10^{-3}\,\frac{\mathrm{N}}{\mathrm{V^2m}}$, $k_c = 3.76 \cdot 10^{-3}\,\frac{\mathrm{N}}{\mathrm{m}}$ and $U_0 = 6.547\,\mathrm{V}$ using an effective mass of $m = 1.85 \cdot 10^{-15}$g. As $|U - U_0|$ is always less than 3 V in the experiment, the maximal relative influence of the quadratic term $\frac{|U-U_0|\lambda_n}{\kappa_n}$ is below 15 %. The fit in Fig. 4.3 shows only the measured frequencies, because the quality factors of the out-of-plane and the in-plane mode of the employed resonator are nearly identical (≈ 80 000). But it shows that the model agrees excellently with the measured data over a large tuning range. Moreover, the extracted frequency splitting $\Omega = \omega_1 - \omega_2 = 7.77\,\mathrm{kHz}$ at $U_0 = 6.547\,\mathrm{V}$ is much larger than the linewidth of $\gamma/2\pi \approx 80\,\mathrm{Hz}$ whereby the system is clearly in the strong-coupling regime. A resonator on a different chip which was tuned using the microwave power (i.e. an effective voltage as described in chapter 2.3) instead of the dc voltage [Fau12a] exhibits higher, dissimilar quality factors and thus allows a simultaneous fit of the resonance frequency and quality factor. The resulting graph is shown in Fig. 4.4. One can clearly see how the quality factors of the red and blue branch interchange as the system is tuned through the coupling region.

The obtained fit parameters can be used to carry out the transformation to the momentary normal coordinates and calculate the shape of the Lissajous figures mentioned above. For the parameter set acquired from the fit in Fig. 4.4 the mode shapes are displayed in Fig. 4.5a at the two positions on the branches marked by the dashed and solid black lines in Fig. 4.4. Fig. 4.5b displays the calculated mode shapes for the same set of parameters, except for the damping, which has deliberately been increased by a factor of ten for both modes. At a microwave power of 129 mW, i.e. the position marked by the

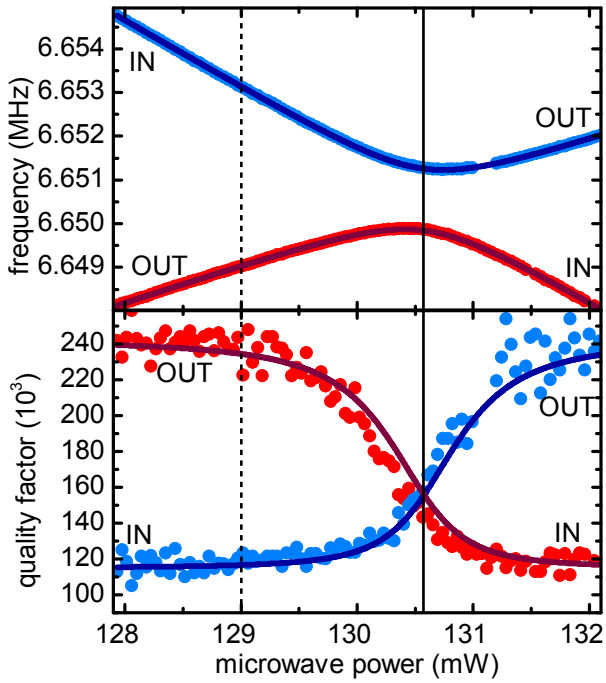


**Figure 4.4:** Avoided crossing data and corresponding fit of a resonator tuned via the microwave power, showing the coupling behavior of both frequency and quality factor. As the resonator modes are swept through the coupling region, the two branches transform from the high quality factor of the out-of-plane mode to the lower quality factor of the in-plane mode and vice versa.

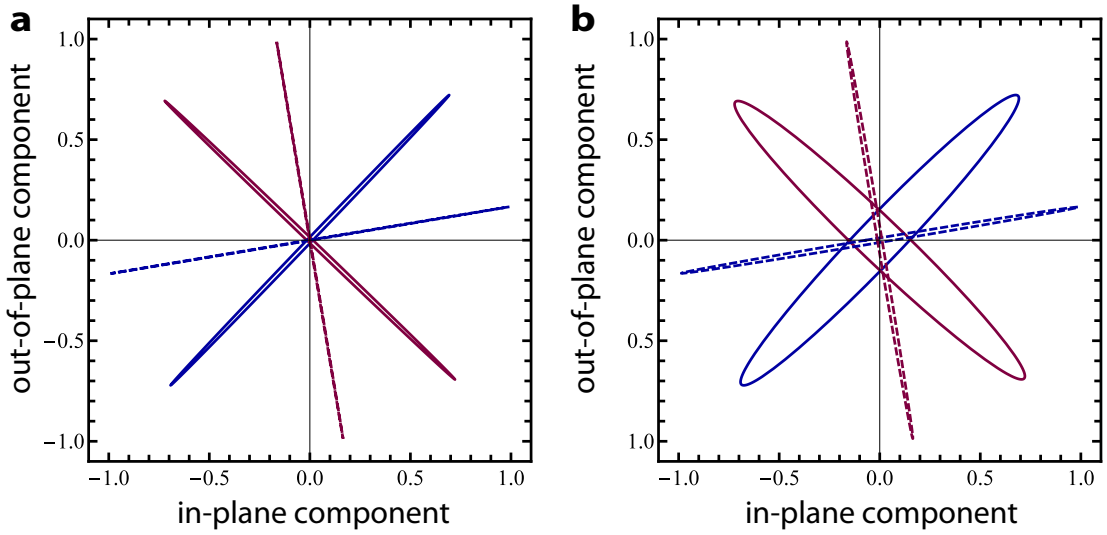


**Figure 4.5:** Mode shapes for two positions in the avoided crossing region. These positions are marked in Fig. 4.4 by a dashed and a solid black line. The corresponding mode shapes are plotted with dashed and solid lines. The mode shapes for the lower branch are plotted in red, those for the upper one in blue. **a** The mode shapes calculated with the parameter set obtained from the fit in Fig. 4.4. At the zero detuning point, the modes are diagonal and almost linear. **b** Idem with a tenfold increased damping for each mode.

dashed black line in Fig. 4.4, the modes (dashed lines in Fig. 4.5) are still predominantly out-of-plane and in-plane modes. They are however already slightly tilted away from the pure out-of-plane and in-plane shapes. At the zero detuning point marked by the solid black line in Fig. 4.4, the modes are then diagonal hybridizations of the out-of-plane and in-plane modes. If one continues tuning through the avoided crossing, the modes continue tilting until far away from the crossing the modes become pure out-of-plane and in-plane modes again. For clarity this is not plotted in Fig. 4.5. The passage through the avoided crossing along one of the branches thus transforms an out-of-plane to an in-plane oscillation and vice versa. Furthermore, at the zero detuning point one can observe a slight eccentricity in the curves. The modes are thus not purely diagonal, but have an - albeit not very pronounced - elliptical shape. This is a consequence of the additional phase shift caused by the damping. If the calculations are carried out without damping, the modes stay completely linear. If the damping is increased as done for the plot in Fig. 4.5b the eccentricity is augmented substantially. However, with such a parameter set, one leaves the regime of strong coupling and enters a regime where the frequency splitting $\Omega$ is no longer much larger than the linewidth of the resonances. In the coupled systems studied in this work, this is therefore not significant, and the mode shapes can be assumed to be linear throughout the avoided crossing.

The strong coupling between the orthogonal flexural modes has been observed on a variety of different resonator chips. To increase the mixed partial derivatives of the electrical field between the electrodes and thereby the coupling between the modes (cf. equation 4.5), resonators with an asymmetric lateral positioning of the string with respect to the electrodes (≈20 nm offset) were fabricated. These resonators showed larger couplings with frequency splittings of up to $\Omega \approx 80\,\mathrm{kHz}$. This is a strong indication that the coupling is predominantly caused by the electric field and not by mechanical coupling at the supports or stress mediated coupling. As the observed coupling strengths lie between 1 kHz and 80 kHz for different electrode designs, and properties such as resonance frequency and quality factors are quite robustly reproduced for all resonator chips, a possible purely mechanical contribution to the coupling seems to play an insignificant role in these systems. Moreover, a mechanical resonator chip with different gaps between the side electrodes and each beam exhibits different coupling constants $\Omega$ for each resonator. The smallest gap (of about 60 to 70 nm) yields $\Omega = 7.77\,\mathrm{kHz}$ (as shown in Fig. 4.3). Fitting the frequencies of the other beams in their respective coupling region gives a $\Omega$ of $7.27 \pm 0.09\,\mathrm{kHz}$, $6.10 \pm 0.02\,\mathrm{kHz}$ and $5.31 \pm 0.03\,\mathrm{kHz}$ with increasing gap size up to roughly 150 nm. Since the electric field between the electrodes decreases with their increasing separation (and the voltage is approximately constant), the coupling is shown to be mediated by the electric field, even though the exact gap sizes are unknown and thus a quantitative relation can not be established.

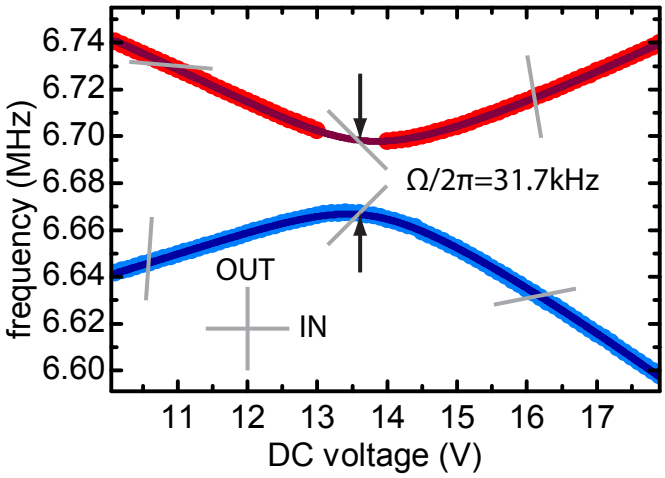


**Figure 4.6:** Avoided crossing with a coupling strength of $\Omega/2\pi$ = 31.7 kHz at a dc bias voltage of 13.6 V. The gray lines schematically symbolize the mode shapes at the respective voltages.

## 4.2 AFM visualization of the mode polarization

As shown in the preceding section, when the modes are tuned through the avoided crossing their polarization changes. Thereby the local normalized resonator amplitude $\epsilon$, as introduced in chapter 3 should be affected in the clamping region. Consequently, a position dependent AFM measurement analogous to the ones presented in chapter 3.4 should reveal this effect when tuning the mode polarization. A resonator with an avoided crossing exhibiting a coupling strength of $\Omega/2\pi$ = 31.7 kHz at a dc bias voltage of 13.6 V was used to carry out such measurements. The corresponding avoided crossing is depicted in Fig. 4.6. It also schematically shows the mode polarization for the two frequency branches as gray lines at the respective dc voltages.

To study the effect of mode polarization tuning, position dependent AFM measurements are conducted for different dc voltages, corresponding to different locations on the avoided crossing branches. All measurements are conducted with a constant force of ≈31 nN exerted on the sample by a triangular silicon nitride cantilever (see Appendix A for details). The resulting quality factors as a function of tip position for four dc bias values of 10 V, 12 V, 13.5 V and 16 V are shown in Fig. 4.7. Because of drifts during the measurements, the images for different values of the dc voltage are not completely congruent with each other. But one can clearly see that the local resonator amplitude in the clamping region changes as the mode polarization is varied. For a dc bias of 10 V, (Fig. 4.7a,e), the imaged shape of the local resonator amplitude, reflected in the Q factor, already differs from the pure out-of-plane and in-plane shape as depicted in the measurements and simulations in Fig. 3.10 in chapter 3.4, quite drastically. Especially the former in-plane mode shows a strong deviation (Fig. 4.7e). Instead of the once symmetric form, the local resonator amplitude is clearly asymmetrically shaped with a predominant lateral

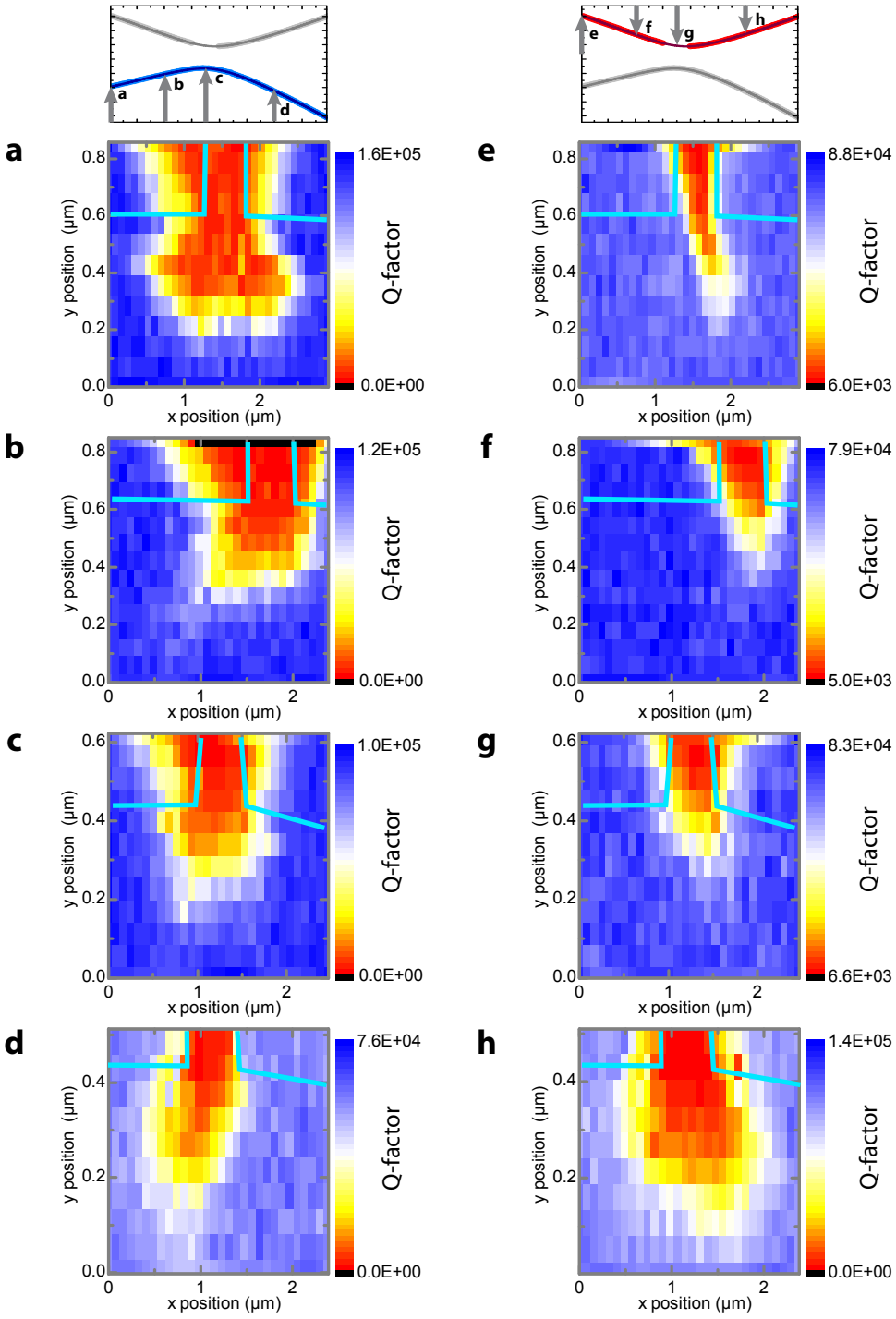


**Figure 4.7:** Q factor maps resulting from position dependent AFM measurements. **a-d** for the lower branch. The corresponding points on the anticrossing are marked in the panel above **a**. **e-h** idem for the upper branch. In all panels **a-h**, the underlying resonator topology is shown by light blue lines.

direction of the strain field to one side of the resonator clamp. Note that the out-of-plane mode gets damped much more efficiently by the tip than the in-plane mode and thus the out-of-plane contribution is more pronounced in Fig. 4.7. As the modes are tuned further through the avoided crossing, the imaged shape of the local resonator amplitude changes even more (cf. Fig. 4.7b,f for a voltage of 12 V). At the zero detuning point both modes are diagonal hybrid modes composed of equal parts of out-of-plane and in-plane modes as displayed in Fig. 4.5. Accordingly, the obtained images for the two modes at this point are very similar and one finds a mirror symmetry along the beam axis between the images acquired for this dc voltage, as can be seen in Fig. 4.7c,g. Here, the image of the local resonator amplitude is again dominated by the out-of-plane component, as the tip-induced damping is larger for this oscillation direction. Going to even higher voltages, the mode polarization is tilted further and by comparing Fig. 4.7a,e with Fig. 4.7d,h, one can identify a mirrored image of the modes' local amplitude shapes on either side of the avoided crossing. The position dependent AFM measurements thus clearly confirm the theoretical calculations of the mode polarization change as the modes are tuned through the avoided crossing and the out-of-plane mode is transformed into the in-plane mode and vice versa.

Additionally, the unperturbed Q factors of the modes change along the two branches, as was also shown in Fig. 4.4. The fact that the two modes do not exhibit completely equal quality factors at the zero detuning point can be explained by the dielectric damping as described in chapter 2.3. As the voltages are quite high for these measurements ($\geq$10 V), the dielectric damping is very significant. The out-of-plane and the in-plane mode experience different strengths of dielectric damping and thereby the point of zero detuning is no longer necessarily the point of equal damping for the two branches for resonators with a high coupling strength $\Omega$. A detailed analysis of this effect can be found in ref. [Fau12b].

## 4.3 Nonadiabatic dynamics of the coupled modes

In the preceding sections of this chapter, it has been shown how the out-of-plane and the in-plane mode are coupled by cross derivatives of the electric field, and how the mode polarization changes along the branches of the avoided crossing between the two modes. All the observations made there rest on the assumption that the tuning speed is slow (adiabatic) compared to the time scale given by the coupling strength. This chapter presents results on tuning speed dependent measurements that have been published in ref. [Fau12c].

When slowly (adiabatically) tuning the system through the coupling region, the system energy will remain in the branch in which it was initialized, thereby transforming an out-of-plane oscillation to an in-plane motion (and vice-versa for the other mode) as shown in chapter 4.1. At high tuning speeds, the diabatic behavior dominates and there is no mixing between the modes. This classical behaviour [Nov10] is analogous to the

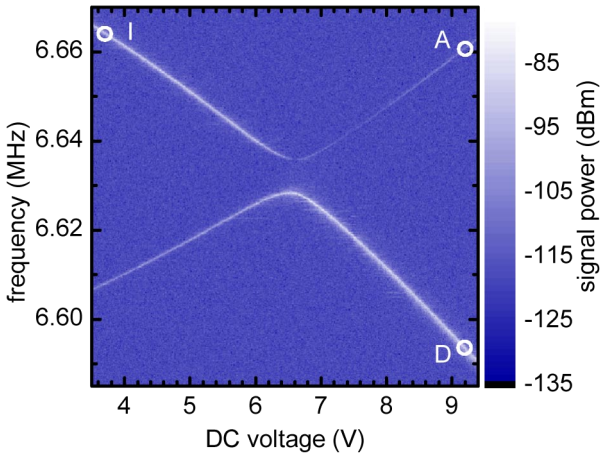


**Figure 4.8:** Avoided crossing. The signal power of the driven resonances is shown color-coded versus DC voltage and drive frequency. The three circles denote the initial state (I) and two possible final states after an adiabatic (A) or diabatic (D) transition through the coupling region, as described in the text.

well-known quantum mechanical Landau-Zener transition. The transition probabilities are identical in the quantum and classical case:

$$P_{\text{dia}} = \exp\left(-\frac{\pi\Omega^2}{2\alpha}\right), \; P_{\text{adia}} = 1 - P_{\text{dia}} \tag{4.11}$$

where the change of the frequency difference between the two modes in time

$$\alpha = \frac{\partial(\omega_1 - \omega_2)}{\partial t} \text{ using } \omega_j = \sqrt{\frac{k_0 + k_j}{m}} \tag{4.12}$$

denotes the tuning speed.

The measurement sequence is depicted in Fig. 4.9a: The system is initialized at point I (see Fig. 4.8) by applying a 6.6647 MHz tone and a dc bias voltage of 3.6 V to the electrodes. At $t = 0$, the voltage (blue line) is now ramped up to 9.1 V within time $\tau$. As the start and stop frequencies are kept constant throughout the experiment, changing $\tau$ changes the tuning speed $\alpha$ and therefore the transition probability. Thus, the system's energy is distributed between point A or D (see Fig. 4.8), depending on the ramp time $\tau$. At $t = 0$, the mechanical resonator gets detuned from the constant drive frequency. Therefore its energy starts to decay as reflected by the decreasing signal power (green dashed line in Fig. 4.9a). After a short additional delay of $\delta$ (to avoid transient artifacts in the measurement), the decay of the mechanical oscillation is recorded with a spectrum analyzer. An exponential fit to the signal power, symbolized by the dotted black line in Fig. 4.9a allows the extraction of the oscillation magnitude at $t = \tau$ which is normalized to the magnitude measured before the transition at point I to account for slight variations in the initialization. This experiment is repeated with many different ramp times $\tau$ and with the detection frequency of the spectrum analyzer set to monitor either point A or D. The results of these measurements are shown in Fig. 4.9b. The data clearly shows the expected

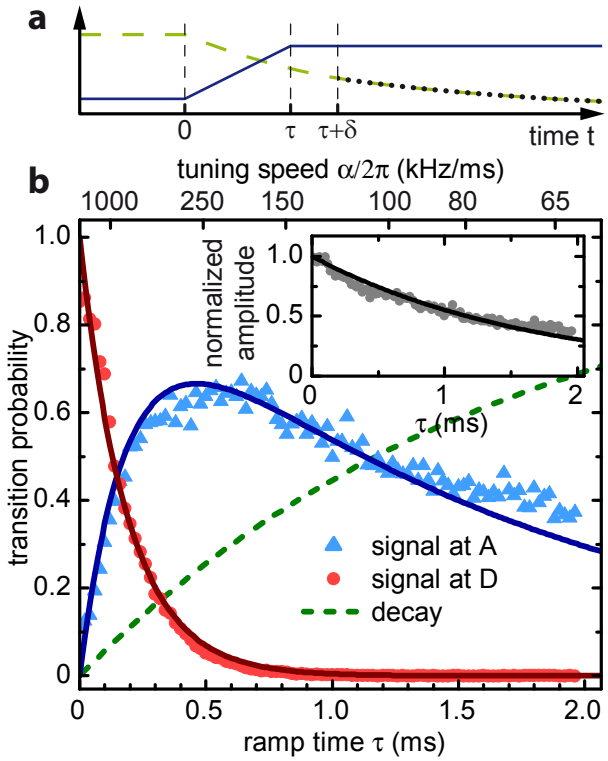


**Figure 4.9:** . The measurement sequence of the time-resolved experiment is shown in **a**. At $t = 0$, the dc bias voltage (blue line) is ramped up in the timespan $\tau$, after the delay $\delta$ the measurement of the mechanical signal power (green dashed line) starts at point A or D in Fig. 4.8 and a fit (black dotted line) is used to extract the magnitude of the beam oscillation at $t = \tau$. The normalized signal power at $t = \tau$ and thus the transition probability obtained for different ramp times $\tau$ measured at point A in Fig. 4.8 (blue triangles) or point D (red dots) is plotted in **b** together with the theoretical model described in the text (solid lines). The inset shows the sum of both measurements and displays a clear exponential decay. The corresponding decay probability is represented by a green dashed line in the main plot.

behaviour: For short ramp times below 0.2 ms, the diabatic behaviour dominates. For long ramp times, the adiabatic transition prevails, even though mechanical damping decreases the signal for large $\tau$.

As can be seen in the inset of Fig. 4.9b, the sum of the two curves perfectly follows the exponential decay of the mechanical energy (solid line). This decay in amplitude between $t = 0$ and $t = \tau$ has to be accounted for in the theoretical model and therefore an additional decay term $e^{-\gamma t}$ is introduced to equations (4.11). The solid lines in Fig. 4.9b show the resulting transition probabilities to point A and D and are calculated by using the $\alpha$ and $\Omega$ obtained from the data in Fig. 4.3. The measured data was rescaled by a constant factor with no free parameters to represent the probability distribution of the resonator's energy after a transition. This is done by rewriting the change of the frequency difference between the two unperturbed states $\omega_j(U) = \sqrt{\frac{k_0+k_j(U)}{m}}$

$$\alpha = \frac{\partial(\omega_1 - \omega_2)}{\partial t} = \frac{(\omega_1(U_i) - \omega_2(U_i)) - (\omega_1(U_f) - \omega_2(U_f))}{\tau} = \frac{\Delta\omega}{\tau}, \tag{4.13}$$

so that $P_{\mathrm{diab}}$ can be expressed as a function of the ramp time $\tau$ and the measured frequency differences $\Delta\omega$ between the initial voltage $U_i$ and the final voltage $U_f$, as the two voltages are kept constant throughout the experiment and only $\tau$ is varied. By introducing the mechanical damping term $e^{-\gamma t}$ at $t = \tau$, the probability is transformed into a normalized state population

$$S_{\mathrm{dia}}(\tau) = e^{\frac{-\pi\Omega^2\tau}{2\Delta\omega} - \gamma\tau} \tag{4.14}$$

$$S_{\mathrm{adia}}(\tau) = \left(1 - e^{\frac{-\pi\Omega^2\tau}{2\Delta\omega}}\right) e^{-\gamma\tau}. \tag{4.15}$$

The amplitudes of the two datasets $S_0^A(\tau)$ and $S_0^D(\tau)$ are then rescaled to fit these two equations. Both are shown in Fig. 4.9b along with the theoretical curves given by (4.14 and 4.15). Note that $\Omega$, $\gamma$ and $\Delta\omega$ are already known from previous measurements and are no fit parameters.

A third state, representing the probability that the mechanical energy decays, is required to keep the sum of the probabilites at one. It is determined from the inset and shown as a dashed green line in Fig. 4.9. The corresponding decay constant $1/\gamma = 1.92\,\mathrm{ms}$ is identical to the one extracted from the spectrally measured quality factor. Note that dynamics with a time constant much smaller than $1/\gamma$ are observed, enabling coherent control of the system.

# Chapter 5

# Conclusion and outlook

This thesis presents the results of several experiments on high-Q silicon nitride string resonators. The initial idea of the project is to use an AFM tip as a local perturbation acting on the nanomechanical resonator and thereby gain insight into the damping behavior of the system. To this end, an experiment combining a customized AFM and a sensitive detection scheme for the nanomechanical motion was devised. The specifics of the AFM and the necessary calibration procedures are given in chapter 2. It also contains static AFM measurements of silicon nitride nanostrings, which can be used to extract material properties such as the tensile stress.

A detailed description of the employed transduction scheme for dynamical measurements of the nanomechanical motion is presented thereafter. The nanomechanical resonator is dielectrically coupled to a microwave cavity, enabling sensitive electrical readout of the vibrational motion [Fau12a]. Additionally, introducing a microwave bypass capacitor allows the application of dc and rf voltages to employ a dielectric driving technique [Unt09]. This ultimately allows tuning of both the resonance frequency and the quality factor of the mechanical resonance with an applied dc voltage. A simple model for altering these quantities is derived, incorporating the resonator's complex electric polarizability and position in an inhomogeneous electric field, which agrees very well with the experimental findings and finite element simulations. Comparing two sample geometries demonstrates that electrode design determines the direction of frequency tuning of the flexural modes of the string resonator. The experiments demonstrate that dielectric losses become highly relevant when using nanoscale electrode geometries generating large field gradients which provide high tunability. This allows to directly measure the ratio of the real and the imaginary part of the resonator's polarizability by monitoring the mechanical resonance. The resulting loss tangent agrees very well with material properties of silicon nitride. The induced dielectric losses could be used as a means to achieve a Q factor control [Rod03, Sul00, Ven11] that does not require any active electronics such as a phase-locked loop but rather a single dc voltage. Such a Q factor control could be employed to increase the bandwidth of NEMS sensors significantly, leading to much more adaptable devices.

In chapter 3 the presented transduction scheme is then used to independently probe the nanomechanical motion of silicon nitride string resonators while introducing a local perturbation of the system via the AFM tip. The presented measurements demonstrate manipulation of the mechanical impedance mismatch of the resonator on the nanoscale, which is accomplished by forming a mechanical point contact between the string resonator and the AFM tip. In the clamping region of the resonator, its flexural modes induce minute deformations in the sub-picometer regime, allowing to transfer vibrational energy into the AFM cantilever via the mechanical point contact. The amount of transferred energy is probed by the decrease in Q factor of the resonator. The energy transfer can be controlled by changing the contact position or the force applied to the AFM tip at a given location. Thereby the passage between a highly mismatched, high-Q system (with quality factors of up to $\mathrm{Q} = 250\,000$) to a highly matched, low-Q system ($\mathrm{Q} \leq 2\,000$) can be induced and observed on a single resonator. As the internal friction of the resonator does not change, this allows for a quantification of the damping contribution coming from the vibrational modes radiating into the supports [Cro01, WR08]. A theoretical model which was specifically developed by Andreas Isacsson from Chalmers University of Technology in Gothenburg in a collaborative effort is presented. The effect of the AFM tip is modeled as an additional mechanical contact impedance, which modifies the impedance mismatch between the resonator and its environment. This contact impedance depends on the applied force as well as on position through the local normalized resonator amplitude. Fitting and analyzing the experimental data with this model yields an excellent quantitative agreement. The results demonstrate that high-Q nanomechanical resonators are enabled by a large mechanical impedance mismatch between the suspended resonator and its clamping region, which suppresses the radiation of energy into the support structure.

In chapter 4, the AFM measurement technique is used to study coupled modes of the nanomechanical resonator. These are composed of the fundamental flexural out-of-plane and in-plane modes, i.e. orthogonal modes with oscillation directions perpendicular and parallel to the substrate. With the appropriate electrode design, these modes can be tuned into resonance and a pronounced avoided crossing is observed [Fau12c]. The coupling is shown to be mediated by the inhomogeneous electric field rather than a mechanical contribution via the shared clamping region or a stress-mediated coupling. The frequencies and quality factors of the two branches of the avoided crossing are calculated using the model of two linearly coupled, damped harmonic oscillators. A fit of the obtained solutions to the data shows excellent agreement, and the extracted fit parameters can be used to calculate the mode shapes during the passage through the avoided crossing. It is demonstrated that the passage through the avoided crossing along one branch continuously rotates the oscillation direction and transforms the out-of-plane to an in-plane oscillation and vice versa. This changes the local resonator amplitude in the clamping region and can be mapped out in position dependent AFM measurements. The resulting data confirm the theoretically calculated mode shapes. Also, in tuning speed dependent measurements

classical Landau-Zener transitions between the two modes can be observed, which agree very well with a theoretical model [Nov10, Fau12c].

The experiments presented here employ the AFM in constant force mode, where the tip is in contact with the sample surface at all times. The contact impedance and the accompanying change in Q factor is governed by the detailed nature of the microscopic contact dynamics. As the surface deformations in the clamping region lie in the sub-picometer regime, one can in principal investigate tip sample-interactions in a linear response regime while pushing on the sample with substantial forces. However, for quantitative studies of tip-sample interactions, future experiments will have to be carried out in an ultra high vacuum environment [Got99], to avoid the influence of residual water films. Additionally, the AFM-cantilever could be equipped with another piezo to drive the mechanical motion of the resonator through the tip. Thus one could see whether the energy flow is indeed invariant under time reversal, i.e. if one cannot only extract, but also insert energy via the mechanical point contact. Moreover, using dynamic modes of AFM operation opens up possibilities for a variety of future experiments. Recently it has been demonstrated that the parametric coupling of two resonator modes can be used to cool down one of the modes, using the other mode as a phonon cavity [Mah12]. A similar scheme had also been achieved slightly earlier with a microcantilever [Ven11]. By approaching an oscillating AFM cantilever to a silicon nitride string resonator one could realize such an experiment with adjustable, potentially very large coupling. Furthermore, the dielectric coupling of the resonator to a microwave cavity enables optomechanical backaction [Fau12a]. By coupling the resonator to an AFM cantilever one could realize an optomechanical system, which is coupled to another mechanical degree of freedom with independently tunable coupling strength. Such a system could be used for studying synchronization effects in both the weak and the strong coupling regime. Cooling down one of the modes in the phonon cavity configuration (with the silicon nitride resonator acting as the cavity) could be much more efficient than in previous experiments. As the achievable quality factors of the phonon cavity are larger, and the frequencies can be increased by orders of magnitude with respect to the values reported in ref. [Mah12], the cooling efficiency could greatly exceed existing schemes.

To increase long term stability and profit from enhanced mechanical quality factors it would also be very interesting to cool the system to cryogenic temperatures. The AFM setup is suited for operation in a low temperature environment and with a sample holder that includes thermometry such experiments could readily be conducted.

# Appendix A

# Employed cantilevers

- Budget Sensors ContAl contact mode cantilever - employed for all measurements unless those stated below for the other cantilevers.

| | |
|---|---|
| Force constant | $0.07$ N/m to $0.4$ N/m |
| Resonance frequency | 9 kHz-17 kHz |
| Length | $450 \pm 10$ µm |
| Width | $50 \pm 5$ µm |
| Thickness | $2 \pm 1$ µm |
| Tip Height | $17 \pm 2$ µm |
| Tip Radius | 10 nm |
| Half Cone Angle | $20° - 30°$ |
| Reflex coating | Aluminium |

- Budget Sensors Multi75Al-G force modulation mode cantilever - used for the static measurements in chapter 2.2.1.

| | |
|---|---|
| Force constant | 1 N/m to 7 N/m |
| Resonance frequency | 60 kHz-90 kHz |
| Length | $225 \pm 10$ µm |
| Width | $28 \pm 5$ µm |
| Thickness | $3 \pm 1$ µm |
| Tip Height | $17 \pm 2$ µm |
| Tip Radius | 10 nm |
| Half Cone Angle | $20° - 30°$ |
| Reflex coating | Aluminium |

- Veeco DNP-S10 silicon nitride triangular cantilever shape D - used for the modeshape-measurements in chapter 4 and for the in-plane-mode measurements in Fig. 3.10 in chapter 3.4

| | |
|---|---|
| Force constant | $0.03$ N/m to $0.12$ N/m |
| Resonance frequency | $12$ kHz-$24$ kHz |
| Length | $200 \pm 5$ µm |
| Width | $20 \pm 5$ µm |
| Thickness | $0.6 \pm 0.05$ µm |
| Tip Height | $2.5 - 8$ µm |
| Tip Radius | $40$ nm (Max) |
| Half Cone Angle | $15° - 20°$ |
| Reflex coating | Aluminium |

# Appendix B

# Sample fabrication

The following section is (almost) identical to Appendix A.1 of [Sei12] (as the samples used in chapters 2.3, 3, and 4 were fabricated by my master student M. Seitner), as well as Appendix B of [Fau13]. The different evolution steps of the fabrication are not described (see [Kre11] for the initial development of the process), but only the most recent recipe is presented here.

The processing starts with commercially available quartz wafers coated with a 100 nm thick silicon nitride layer, already diced in $5 \cdot 5\,\mathrm{mm}^2$ chips.

- Cleaning and preparation

| **step** | **description** |
|---|---|
| cleaning | sonificate for 3 minutes in aceton<br>rinse in isopropanol and blow-dry with nitrogen |
| protective coating[1] | spin-coat with Shipley Microposit 1813 resist |
| marking | small scratch on top side, number on the bottom |
| remove coating | sonificate for 2 minutes in aceton<br>rinse in isopropanol and blow-dry with nitrogen |

- Defining the gold electrodes

| **step** | **description** |
|---|---|
| deposit resist | spin-coat PMMA 950k A6<br>1 s 800 rpm, 30 s 5000 rpm<br>bake for at least 60 min at 120° |
| conductive layer | evaporate 3 nm of chromium onto the resist |
| SEM lithography | 10 kV acceleration voltage, 20 µm aperture<br>100 µC/cm$^2$ dose |
| chromium etch | 30 s in *Merck Selectipur 111547* chromium etchant[2]<br>rinse in water |

[1] If not already applied prior to dicing the wafer ^_^ .

[2] It is important to use a chromium etchant based on nitric acid, as solutions based on perchloric acid attack the resist layer and lead to over-exposed structures.

| step | description |
|---|---|
| develop | 50 s in isopropanol:MIBK 3:1<br>rinse in isopropanol, blow-dry with nitrogen |
| evaporation | 3 nm chromium (adhesion layer)<br>140 nm gold |
| lift-off | bathe in aceton (or in 100° DMSO over night in case of liftoff problems)<br>rinse in isopropanol, blow-dry with nitrogen |

- Defining the beam

| step | description |
|---|---|
| deposit resist | spin-coat PMMA 950k A6<br>1 s 800 rpm, 30 s 5000 rpm<br>bake for at least 60 min at 120° |
| conductive layer | evaporate 3 nm of chromium onto the resist |
| SEM lithography | 10 kV acceleration voltage, 20 µm aperture<br>140 µC/cm$^2$ dose |
| chromium etch | 30 s in *Selectipur 111547* chromium etchant<br>rinse in water |
| develop | 50 s in isopropanol:MIBK 3:1<br>rinse in isopropanol, blow-dry with nitrogen |
| evaporation | 30 nm cobalt |
| lift-off | bathe in aceton<br>rinse in isopropanol, blow-dry with nitrogen |

- Dry&wet etch

| step | description |
|---|---|
| ICPRIE dry etch | 4 sccm Ar and 2 sccm $SF_6$ at 2 mTorr with an ICP power of 70 W and an RF power of 35 W, duration 9 min |
| mask removal | 90 s in "piranha" ($H_2SO_4 : H_2O_2$ 1:1) |
| underetching | 160 s in buffered HF |
| drying | rinse in water<br>remove from hot isopropanol and immediately blow-dry with nitrogen |

# Appendix C

# Modeling of the avoided crossing with mathematica

## The DGLs for two linearly coupled oscillators

For an undamped system, the equations read:

$m x_1'' + k_1 x + k_c (x_1 - x_2) == 0$

$m x_2'' + k_2 x + k_c (x_2 - x_1) == 0$

And can be written in matrix form:

$m_{ik} x_i'' + k_{jl} x_j = 0$

where

$m_{ik}$ = {{m, 0}, {0, m}}//MatrixForm

$k_{jl}$ = {{$k_1 + k_c$, $-k_c$}, {$-k_c$, $k_2 + k_c$}} //MatrixForm

$$\begin{pmatrix} m & 0 \\ 0 & m \end{pmatrix}$$

$$\begin{pmatrix} k_1 + k_c & -k_c \\ -k_c & k_2 + k_c \end{pmatrix}$$

With additional linear damping, another matrix can be introduced:

$\gamma_{ik}$ = {{$\gamma_1$, 0}, {0, $\gamma_2$}} //MatrixForm

$$\begin{pmatrix} \gamma_1 & 0 \\ 0 & \gamma_2 \end{pmatrix}$$

The Ansatz

$x_i = a_i e^{i\omega t}$

leads to following equations for the amplitudes a:

$-\omega^2 m_{ik} a_i + k_{ik} a_i = \Gamma_{ik} a_i$

with

$\Gamma_{ik} = -i\omega\gamma_{ik}$

## Example: coupled identical oscillators no damping

kmat = {{k + kc, −kc}, {−kc, k + kc}};

mmat = {{$\omega^2 m$, 0}, {0, $\omega^2 m$}};

gesmat = Inverse[mmat].kmat;

MatrixForm@kmat

MatrixForm@mmat

MatrixForm@gesmat

$$\begin{pmatrix} k + \text{kc} & -\text{kc} \\ -\text{kc} & k + \text{kc} \end{pmatrix}$$

$$\begin{pmatrix} m\omega^2 & 0 \\ 0 & m\omega^2 \end{pmatrix}$$

$$\begin{pmatrix} \frac{k+\text{kc}}{m\omega^2} & -\frac{\text{kc}}{m\omega^2} \\ -\frac{\text{kc}}{m\omega^2} & \frac{k+\text{kc}}{m\omega^2} \end{pmatrix}$$

```
eugenex = Eigensystem[gesmat]
```

$$\left\{\left\{\frac{k}{m\omega^2}, \frac{k+2\text{kc}}{m\omega^2}\right\}, \{\{1,1\},\{-1,1\}\}\right\}$$

The Eigenvalues give the frequencies of the coupled system

```
solu1 = Solve[eugenex[[1,1]] == 1, ω]
```

```
solu2 = Solve[eugenex[[1,2]] == 1, ω]
```

$$\left\{\left\{\omega \to -\frac{\sqrt{k}}{\sqrt{m}}\right\}, \left\{\omega \to \frac{\sqrt{k}}{\sqrt{m}}\right\}\right\}$$

$$\left\{\left\{\omega \to -\frac{\sqrt{k+2\text{kc}}}{\sqrt{m}}\right\}, \left\{\omega \to \frac{\sqrt{k+2\text{kc}}}{\sqrt{m}}\right\}\right\}$$

```
neugenex = eugenex/.{ω → solu1[[1,1,2]]}
```

$$\left\{\left\{1, \frac{k+2\text{kc}}{k}\right\}, \{\{1,1\},\{-1,1\}\}\right\}$$

Additional damping leads to imaginary frequencies. The imaginary part then gives the damping for the coupled modes.
In the case above, one can also easily find the normal coordinates:

```
trafmat = neugenex[[2]]
```

```
MatrixForm@trafmat
```

```
diagmat = Simplify[trafmat.gesmat.Inverse[trafmat]];
```

```
MatrixForm@diagmat/.{k → 1, k1 → 1, kc → 0.5}
```

```
trafvec = trafmat.{x, y}/.{k → 1, k1 → 1, kc → 0.5};
```

```
MatrixForm@trafvec
```

$$\{\{1,1\},\{-1,1\}\}$$

$$\begin{pmatrix} 1 & 1 \\ -1 & 1 \end{pmatrix}$$

$$\begin{pmatrix} \frac{1}{m\omega^2} & 0 \\ 0 & \frac{2.}{m\omega^2} \end{pmatrix}$$

$$\begin{pmatrix} x+y \\ -x+y \end{pmatrix}$$

With the well known normal coordinates. Note that plugging the $\omega$-solution into the Eigensystem does rescale the Eigenvalues, but not the Eigenvectors. This will be important later.

## Two coupled oscillators with different damping and force constants

**kmat = {{k1 + kc, kc}, {kc, k2 + kc}};**

**digmat = {{$\omega^2 m - i\gamma 1\omega$, 0}, {0, $\omega^2 m - i\gamma 2\omega$}};**

**wmat = Inverse[digmat].kmat;**

**MatrixForm@wmat**

**eugen = Eigensystem[wmat];**

**eq1 = eugen[[1, 1]] == 1;**

**eq2 = eugen[[1, 2]] == 1;**

**sol1 = Solve[eq1, $\omega$];**

**sol2 = Solve[eq2, $\omega$];**

$$\begin{pmatrix} \frac{(\text{k1+kc})\left(-i\gamma 2\omega+m\omega^2\right)}{-\gamma 1\gamma 2\omega^2-im\gamma 1\omega^3-im\gamma 2\omega^3+m^2\omega^4} & \frac{\text{kc}\left(-i\gamma 2\omega+m\omega^2\right)}{-\gamma 1\gamma 2\omega^2-im\gamma 1\omega^3-im\gamma 2\omega^3+m^2\omega^4} \\ \frac{\text{kc}\left(-i\gamma 1\omega+m\omega^2\right)}{-\gamma 1\gamma 2\omega^2-im\gamma 1\omega^3-im\gamma 2\omega^3+m^2\omega^4} & \frac{(\text{k2+kc})\left(-i\gamma 1\omega+m\omega^2\right)}{-\gamma 1\gamma 2\omega^2-im\gamma 1\omega^3-im\gamma 2\omega^3+m^2\omega^4} \end{pmatrix}$$

Let's plot with typical parameters

sol 3 is the lower branch, sol 4 the upper one

**meff = 0.5 * 3.7*^-15;**

**fitparams = {k10 → "3.229844053452912",**

**k20 → "3.229525491154551",**

$a \to -$"0.0015182378034149 11",

$b \to$ "0.0008605726790928819",

kc $\to$ "0.0006866234005317669",

p0 $\to$ "130.4424309044919",

$\gamma 2 \to$ "1347.338900836815"};

params = {k1 $\to$ k10 + $a * (p$ - p0), k2 $\to$ k20 + $b * (p$ - p0), $\gamma 1 \to 0, \gamma 2 \to 0, m \to$ meff};

upperf = Re[sol1[[4, 1, 2]]]/.params/.fitparams;

lowerf = Re[sol1[[3, 1, 2]]]/.params/.fitparams;

freqplot = Plot[{upperf, lowerf}, $\{p, 120, 140\}$, PlotRange $\to$ All,

PlotStyle $\to$ {{Red, Thick}, {Blue, Thick}}]

meff = 0.5 * 3.7*^-15;

params = {k1 $\to$ k10 + $a * (p$ - p0), k2 $\to$ k20 + $b * (p$ - p0),

$\gamma 1 \to$ 6.377341400210903323384038552758985101822365552 16.*^-13,

$\gamma 2 \to$ 1.347338900836814595923438609633190237457383079516.*^-12, $m \to$ meff};

upper$\gamma$ = Im[sol1[[4, 1, 2]]]/.params/.fitparams;

lower$\gamma$ = Im[sol1[[3, 1, 2]]]/.params/.fitparams;

freqplot = Plot[{upper$\gamma$, lower$\gamma$}, $\{p, 120, 140\}$, PlotRange $\to$ All,

PlotStyle $\to$ {{Red, Thick}, {Blue, Thick}}]

An interesting question is how do the modes actually look like. In the case of the coupling between in- and out-of-plane mode, are they simply diagonal, or elliptic, etc. To find out about this mode polarization, we transform to the momentary normal coordinates, which we do by creating our transformation matrix from our Eigensystem:
Note, that we plug in the $\omega$-solution, so that we can use our old fitparameters and get numerical values. The script for the fitparameters is in the Weig Group Folder.

neugen = eugen/.$\omega \to$ sol1[[4, 1, 2]];

fitparams = {k10 $\to$ "3.229844053452912",

k20 $\to$ "3.229525491154551",

```
a → -"0.0015182378034149 11",
b → "0.0008605726790928819",
kc → "0.0006866234005317669",
p0 → "130.4424309044919",
γ2 → "1347.338900836815"};

Clear[trafmat]
trafmat[x_]:=neugen[[2]]/.params/.fitparams/.p → x
trafvec = trafmat[#].{x, y}&/@Range[120, 140, 0.1];
coeff1x = normal1(Coefficient[trafvec[[1, 1]], x]);
coeff1y = normal1(1/Sqrt[2]);
coeffxlist1 = (Sqrt[1/(Abs[Coefficient[#[[1]], x]]^2 + 1)]&/@trafvec)*
(Coefficient[#[[1, 1]], x]&/@trafvec);
coeffylist1 = (Sqrt[1/(Abs[Coefficient[#[[1]], x]]^2 + 1)]&/@trafvec)*
(Coefficient[#[[1, 2]], y]&/@trafvec);
coeffxlist2 = (Sqrt[1/(Abs[Coefficient[#[[2]], x]]^2 + 1)]&/@trafvec)*
(Coefficient[#[[2, 1]], x]&/@trafvec);
coeffylist2 = (Sqrt[1/(Abs[Coefficient[#[[2]], x]]^2 + 1)]&/@trafvec)*
(Coefficient[#[[2, 2]], y]&/@trafvec);
```

So here is the transformation to the momentary normal coordinates, (Sqrt[1/(Abs[Coefficient[#[[1]],x]]^2+1)] is a normalization constant ensuring that in $\alpha$ x+ $\beta$ y Abs[$\alpha$]^2+Abs[$\beta$]^2==1.
Next will be a nice Plot and some animations, no comment on these ^_^;; Executing the code below will also produce a nice video.

```
pl1 =
Table[
ParametricPlot[
{{Abs[coeffxlist1[[p]]]Sin[x + Arg[coeffxlist1[[p]]]], coeffylist1[[p]]Sin[x]},
```

```
{Abs[coeffxlist2[[p]]]Sin[x + Arg[coeffxlist2[[p]]]], coeffylist2[[p]]Sin[x]}},
{x, 0, 2π}, PlotRange → 1.1, Frame → True, PlotStyle → {Red, Blue},
FrameStyle → Directive[AbsoluteThickness[2]],
FrameLabel → {"in-plane component", "out-of-plane component"},
LabelStyle → Directive[FontSize → 16]], {p, 1, 201, 1}];

listan = ListAnimate[pl1]

meff = 0.5 * 3.7*^-15;
params = {k1 → k10 + a * (p - p0), k2 → k20 + b * (p - p0), γ1 → 0, γ2 → 0, m → meff};
upperf = Re[sol1[[4, 1, 2]]]/.params/.fitparams;
lowerf = Re[sol1[[3, 1, 2]]]/.params/.fitparams;
freqplot = Plot[{upperf, lowerf}, {p, 120, 140},
PlotRange → {{120, 140}, {4.170 * 10^7, 4.19 * 10^7}},
PlotStyle → {{Red, Thick}, {Blue, Thick}}, Frame → True,
FrameStyle → Directive[AbsoluteThickness[2]], AspectRatio → 1,
FrameTicks → {Range[120, 140, 5], Range[4.175, 4.185, 0.005]10^7, None, None} ,
FrameLabel → {"micro wave power (mW)", "angular frequency ω (1/s)"},
LabelStyle → Directive[FontSize → 16]];

freqpointplot =
Table[ListPlot[{{{a, upperf}}/.p → a, {{a, lowerf}}/.p → a},
PlotRange → {{120, 140}, {4.170 * 10^7, 4.19 * 10^7}}, Frame → False,
AspectRatio → 1, PlotStyle->{{Red}, {Blue}},
PlotMarkers → {Graphics[{Circle[]}], 0.07}], {a, 120, 140, 0.1}];

crosslist = Table[Show[freqplot, freqpointplot[[a]]], {a, 1, Length[freqpointplot], 1}];
```

```
crossan = ListAnimate[crosslist]

Show[crosslist[[1]], ImageSize → 350]

Show[pl1[[1]], ImageSize → 350]

lala =
GraphicsRow[{Show[crosslist[[#]], ImageSize → {384}], Show[pl1[[#]], ImageSize → 350]},
Spacings → {0, 0}, ImageSize → 1200, Alignment → Top]&/@Range[Length[pl1]];

ListAnimate[lala]
```

# Bibliography


[Ald05] J. S. Aldridge and A. N. Cleland. Noise-Enabled Precision Measurements of a Duffing Nanomechanical Resonator. *Phys. Rev. Lett.* **94**, 156403 (2005).

[Ale05] A. Alessandrini and P. Facci. AFM: a versatile tool in biophysics. *Meas. Sci. Technol.* **16**, R65 (2005).

[Ben10] S. D. Bennett, L. Cockins, Y. Miyahara, P. Grütter, and A. A. Clerk. Strong Electromechanical Coupling of an Atomic Force Microscope Cantilever to a Quantum Dot. *Phys. Rev. Lett.* **104**, 017203 (2010).

[Bhu10] B. Bhushan, editor. *Springer Handbook of Nanotechnology*. Springer (2010).

[Bin82] G. Binnig, H. Rohrer, C. Gerber, and E. Weibel. Surface Studies by Scanning Tunneling Microscopy. *Phys. Rev. Lett.* **49**, 57 (1982).

[Bin86] G. Binnig, C. F. Quate, and C. Gerber. Atomic Force Microscope. *Phys. Rev. Lett.* **56**, 930 (1986).

[Bou05] J. Bouchaud and H. Wicht. RF MEMS: status of the industry and roadmaps. In *Society of Photo-Optical Instrumentation Engineers (SPIE) Conference Series*, volume 5717, pages 50–54 (2005).

[Bur03] N. A. Burnham, X. Chen, C. S. Hodges, G. A. Matei, E. J. Thoreson, C. J. Roberts, M. C. Davies, and S. J. B. Tendler. Comparison of calibration methods for atomic-force microscopy cantilevers. *Nanotechnology* **14**, 1 (2003).

[Bur07] T. P. Burg, M. Godin, S. M. Knudsen, W. Shen, G. Carlson, J. S. Foster, K. Babcock, and S. R. Manalis. Weighing of biomolecules, single cells and single nanoparticles in fluid. *Nature* **446**, 1066 (2007).

[But05] H.-J. Butt, B. Cappella, and M. Kappl. Force measurements with the atomic force microscope: Technique, interpretation and applications. *Surf. Sci. Rep.* **59**, 1 (2005).

[Cap99] B. Cappella and G. Dietler. Force-distance curves by atomic force microscopy. *Surf. Sci. Rep.* **34**, 1 (1999).

[Cha11] J. Chan, T. P. M. Alegre, A. H. Safavi-Naeini, J. T. Hill, A. Krause, S. Groblacher, M. Aspelmeyer, and O. Painter. Laser cooling of a nanomechanical oscillator into its quantum ground state. *Nature* **478**, 89 (2011).

[Cha12a] J. Chan, A. H. Safavi-Naeini, J. T. Hill, S. Meenehan, and O. Painter. Optimized optomechanical crystal cavity with acoustic radiation shield. *Appl. Phys. Lett.* **101**, 081115 (2012).

[Cha12b] J. Chaste, A. Eichler, J. Moser, G. Ceballos, R. Rurali, and A. Bachtold. A nanomechanical mass sensor with yoctogram resolution. *Nat Nano* **7**, 301 (2012).

[Cli09] C. A. Clifford and M. P. Seah. Improved methods and uncertainty analysis in the calibration of the spring constant of an atomic force microscope cantilever using static experimental methods. *Meas. Sci. Technol.* **20**, 125501 (2009).

[Col11] G. D. Cole, I. Wilson-Rae, K. Werbach, M. R. Vanner, and M. Aspelmeyer. Phonon-tunnelling dissipation in mechanical resonators. *Nat Commun* **2**, 231 (2011).

[Cra00] H. G. Craighead. Nanoelectromechanical Systems. *Science* **290**, 1532 (2000).

[Cro01] M. C. Cross and R. Lifshitz. Elastic wave transmission at an abrupt junction in a thin plate with application to heat transport and vibrations in mesoscopic systems. *Phys. Rev. B* **64**, 085324 (2001).

[Dea09] R. Dean and A. Luque. Applications of Microelectromechanical Systems in Industrial Processes and Services. *Industrial Electronics, IEEE Transactions on* **56**, 913 (2009).

[Eki05] K. Ekinci. Electromechanical Transducers at the Nanoscale: Actuation and Sensing of Motion in Nanoelectromechanical Systems (NEMS). *Small* **1**, 786 (2005).

[Fau12a] T. Faust, P. Krenn, S. Manus, J. P. Kotthaus, and E. M. Weig. Microwave cavity-enhanced transduction for plug and play nanomechanics at room temperature. *Nat Commun* **3**, 728 (2012).

[Fau12b] T. Faust, J. Rieger, M. J. Seitner, J. P. Kotthaus, and E. M. Weig. Coherent control of a nanomechanical two-level system. *ArXiv e-prints* **1212.3172** (2012).

[Fau12c] T. Faust, J. Rieger, M. J. Seitner, P. Krenn, J. P. Kotthaus, and E. M. Weig. Nonadiabatic Dynamics of Two Strongly Coupled Nanomechanical Resonator Modes. *Phys. Rev. Lett.* **109**, 037205 (2012).

[Fau13] T. Faust. Damping, on-chip transduction, and coherent control of nanomechanical resonators. *unv. Diss. LMU München* (2013).

[Gar07] D. Garcia-Sanchez, A. San Paulo, M. J. Esplandiu, F. Perez-Murano, L. Forró, A. Aguasca, and A. Bachtold. Mechanical Detection of Carbon Nanotube Resonator Vibrations. *Phys. Rev. Lett.* **99**, 085501 (2007).

[Gau99] M. Gauthier and M. Tsukada. Theory of noncontact dissipation force microscopy. *Phys. Rev. B* **60**, 11716 (1999).

[Gie95] F. J. Giessibl. Atomic Resolution of the Silicon (111)-(7x7) Surface by Atomic Force Microscopy. *Science* **267**, 68 (1995).

[Gie03] F. J. Giessibl. Advances in atomic force microscopy. *Rev. Mod. Phys.* **75**, 949 (2003).

[Gil96] D. T. Gillespie. The mathematics of Brownian motion and Johnson noise. *Am J Phys* **64**, 225 (1996).

[Got99] B. Gotsmann, C. Seidel, B. Anczykowski, and H. Fuchs. Conservative and dissipative tip-sample interaction forces probed with dynamic AFM. *Phys. Rev. B* **60**, 11051 (1999).

[Gou03] R. Gould. Dielectric properties of RF-sputtered silicon nitride thin films with gold electrodes. *Thin Solid Films* **433**, 309 (2003).

[Gra99] M. Grandbois, M. Beyer, M. Rief, H. Clausen-Schaumann, and H. E. Gaub. How Strong Is a Covalent Bond? *Science* **283**, 1727 (1999).

[Gra00] K. T. V. Grattan and T. Sun. Fiber optic sensor technology: an overview. *Sensors and Actuators A: Physical* **82**, 40 (2000).

[Gre55] E. I. Green. THE STORY OF Q. *Amer. Sci.* **43**, pp. 584 (1955).

[Hab12] S. J. M. Habraken, K. Stannigel, M. D. Lukin, P. Zoller, and P. Rabl. Continuous mode cooling and phonon routers for phononic quantum networks. *New Journal of Physics* **14**, 115004 (2012).

[Har99] U. Hartmann. MAGNETIC FORCE MICROSCOPY. *Annual Review of Materials Science* **29**, 53 (1999).

[Har09] C. Harris, A. Piersol, and T. Paez. *Shock and Vibrations Handbook*. McGraw-Hill handbooks. McGraw-Hill Education (2009).

[Her81] H. Hertz. Über die Berührung fester elastischer Körper. *J. Reine, Angew. Math.* **92**, 156 (1881).

[Hug01] H. J. Hug, M. A. Lantz, A. Abdurixit, P. J. A. v. Schendel, R. Hoffmann, P. Kappenberger, and A. Baratoff. Subatomic Features in Atomic Force Microscopy Images. *Science* **291**, 2509 (2001).

[Hut93] J. L. Hutter and J. Bechhoefer. Calibration of atomic-force microscope tips. *Rev. Sci. Instrum.* **64**, 1868 (1993).

[Jos09] J. D. Jost, J. P. Home, J. M. Amini, D. Hanneke, R. Ozeri, C. Langer, J. J. Bollinger, D. Leibfried, and D. J. Wineland. Entangled mechanical oscillators. *Nature* **459**, 683 (2009).

[Kel91] D. Keller. Reconstruction of STM and AFM images distorted by finite-size tips. *Surf. Sci.* **253**, 353 (1991).

[Kis08] A. A. Kiselev and G. J. Iafrate. Phonon dynamics and phonon assisted losses in Euler-Bernoulli nanobeams. *Phys. Rev. B* **77**, 205436 (2008).

[Kle68] C. Kleesattel and G. Gladwell. The contact - impedance meter-1. *Ultrasonics* **6**, 175 (1968).

[Kno03] R. G. Knobel and A. N. Cleland. Nanometre-scale displacement sensing using a single electron transistor. *Nature* **424**, 291 (2003).

[Kou05] T. Kouh, D. Karabacak, D. H. Kim, and K. L. Ekinci. Diffraction effects in optical interferometric displacement detection in nanoelectromechanical systems. *Appl. Phys. Lett.* **86**, 013106 (2005).

[Koz06] I. Kozinsky, H. W. C. Postma, I. Bargatin, and M. L. Roukes. Tuning nonlinearity, dynamic range, and frequency of nanomechanical resonators. *Appl. Phys. Lett.* **88**, 253101 (2006).

[Kra12] T. Krastev. Entwicklung und Optimierung von Mikrowellenresonatoren zur dielektrischen Detektion von schwingenden SiN-Nanobalken. *Bachelor thesis, LMU München* (2012).

[Kre11] P. Krenn. Heterodyne dielektrische Detektion von nanomechanischen Resonatoren. *Master's thesis, LMU München* (2011).

[Kun11] K. Kunal and N. R. Aluru. Akhiezer damping in nanostructures. *Phys. Rev. B* **84**, 245450 (2011).

[Li07] M. Li, H. X. Tang, and M. L. Roukes. Ultra-sensitive NEMS-based cantilevers for sensing, scanned probe and very high-frequency applications. *Nature Nanotechnology* **2**, 114 (2007).

[Li10] M. Li, E. B. Myers, H. X. Tang, S. J. Aldridge, H. C. McCaig, J. J. Whiting, R. J. Simonson, N. S. Lewis, and M. L. Roukes. Nanoelectromechanical Resonator Arrays for Ultrafast, Gas-Phase Chromatographic Chemical Analysis. *Nano Lett.* **10**, 3899 (2010).

[Lif00] R. Lifshitz and M. L. Roukes. Thermoelastic damping in micro- and nanomechanical systems. *Phys. Rev. B* **61**, 5600 (2000).

[Mah12] I. Mahboob, K. Nishiguchi, H. Okamoto, and H. Yamaguchi. Phonon-cavity electromechanics. *Nat Phys* **8**, 387 (2012).

[Mam01] H. J. Mamin and D. Rugar. Sub-attonewton force detection at millikelvin temperatures. *Appl. Phys. Lett.* **79**, 3358 (2001).

[Men06] D. Mendels, M. Lowe, A. Cuenat, M. G. Cain, E. Vallejo, D. Ellis, and F. Mendels. Dynamic properties of AFM cantilevers and the calibration of their spring constants. *J. Micromech. Microeng.* **16**, 1720 (2006).

[Mer93] J. Mertz, O. Marti, and J. Mlynek. Regulation of a microcantilever response by force feedback. *Appl. Phys. Lett.* **62**, 2344 (1993).

[Nai09] A. K. Naik, M. S. Hanay, W. K. Hiebert, X. L. Feng, and M. L. Roukes. Towards single-molecule nanomechanical mass spectrometry. *Nature Nanotechnology* **4**, 445 (2009).

[Nov10] L. Novotny. Strong coupling, energy splitting, and level crossings: A classical perspective. *Am J Phys* **78**, 1199 (2010).

[Now65] A. Nowick and W. Heller. Dielectric and anelastic relaxation of crystals containing point defects. *Advances in Physics* **14**, 101 (1965).

[O'C10] A. D. O'Connell, M. Hofheinz, M. Ansmann, R. C. Bialczak, M. Lenander, E. Lucero, M. Neeley, D. Sank, H. Wang, M. Weides, J. Wenner, J. M. Martinis, and A. N. Cleland. Quantum ground state and single-phonon control of a mechanical resonator. *Nature* **464**, 697 (2010).

[Pla13] D. Platz, D. Forchheimer, E. A. Tholén, and D. B. Haviland. Interaction imaging with amplitude-dependence force spectroscopy. *Nat Commun* **4**, 1360 (2013).

[Rad92] M. Radmacher, R. Tillmann, M. Fritz, and H. Gaub. From molecules to cells: imaging soft samples with the atomic force microscope. *Science* **257**, 1900 (1992).

[Rat12] S. Ratcliffe. Developing a resonant waveguide cavity as a notch filter. *Bachelor thesis, LMU München* (2012).

[Reg08] C. A. Regal, J. D. Teufel, and K. W. Lehnert. Measuring nanomechanical motion with a microwave cavity interferometer. *Nat Phys* **4**, 555 (2008).

[Rem12] L. G. Remus and M. P. Blencowe. Damping and decoherence of Fock states in a nanomechanical resonator due to two-level systems. *Phys. Rev. B* **86**, 205419 (2012).

[Rie12] J. Rieger, T. Faust, M. J. Seitner, J. P. Kotthaus, and E. M. Weig. Frequency and Q factor control of nanomechanical resonators. *Appl. Phys. Lett.* **101**, 103110 (2012).

[Rod03] T. R. Rodriguez and R. Garcia. Theory of Q control in atomic force microscopy. *Appl. Phys. Lett.* **82**, 4821 (2003).

[Rug88] D. Rugar, H. J. Mamin, R. Erlandsson, J. E. Stern, and B. D. Terris. Force microscope using a fiber-optic displacement sensor. *Rev. Sci. Instrum.* **59**, 2337 (1988).

[Rug04] D. Rugar, R. Budakian, H. J. Mamin, and B. W. Chui. Single spin detection by magnetic resonance force microscopy. *Nature* **430**, 329 (2004).

[Sei12] M. J. Seitner. Mechanische und dielektrische Manipulation nanomechanischer Resonatoren. *Master's thesis, LMU München* (2012).

[Sha10] J. Shackelford and W. Alexander. *CRC Materials Science and Engineering Handbook, Third Edition*. Taylor & Francis (2010).

[Sou09] D. R. Southworth, R. A. Barton, S. S. Verbridge, B. Ilic, A. D. Fefferman, H. G. Craighead, and J. M. Parpia. Stress and Silicon Nitride: A Crack in the Universal Dissipation of Glasses. *Phys. Rev. Lett.* **102**, 225503 (2009).

[Sta12] G. Stan, S. W. King, and R. F. Cook. Nanoscale mapping of contact stiffness and damping by contact resonance atomic force microscopy. *Nanotechnology* **23**, 215703 (2012).

[Sul00] T. Sulchek, R. Hsieh, J. D. Adams, G. G. Yaralioglu, S. C. Minne, C. F. Quate, J. P. Cleveland, A. Atalar, and D. M. Adderton. High-speed tapping mode imaging with active Q control for atomic force microscopy. *Appl. Phys. Lett.* **76**, 1473 (2000).

[Sul02] T. Sulchek, G. G. Yaralioglu, C. F. Quate, and S. C. Minne. Characterization and optimization of scan speed for tapping-mode atomic force microscopy. *Rev. Sci. Instrum.* **73**, 2928 (2002).

[Tet10] TetardL., PassianA., and ThundatT. New modes for subsurface atomic force microscopy through nanomechanical coupling. *Nat Nano* **5**, 105 (2010).

[Teu11] J. D. Teufel, T. Donner, D. Li, J. W. Harlow, M. S. Allman, K. Cicak, A. J. Sirois, J. D. Whittaker, K. W. Lehnert, and R. W. Simmonds. Sideband cooling of micromechanical motion to the quantum ground state. *Nature* **475**, 359 (2011).

[Top00] M. A. Topinka, B. J. LeRoy, S. E. J. Shaw, E. J. Heller, R. M. Westervelt, K. D. Maranowski, and A. C. Gossard. Imaging Coherent Electron Flow from a Quantum Point Contact. *Science* **289**, 2323 (2000).

[Unt09] Q. P. Unterreithmeier, E. M. Weig, and J. P. Kotthaus. Universal transduction scheme for nanomechanical systems based on dielectric forces. *Nature* **458**, 1001 (2009).

[Unt10a] Q. P. Unterreithmeier, T. Faust, and J. P. Kotthaus. Damping of Nanomechanical Resonators. *Phys. Rev. Lett.* **105**, 027205 (2010).

[Unt10b] Q. P. Unterreithmeier, T. Faust, S. Manus, and J. P. Kotthaus. On-Chip Interferometric Detection of Nanomechanical Motion. *Nano Lett.* **10**, 887 (2010).

[Ven11] W. J. Venstra, H. J. R. Westra, and H. S. J. van der Zant. Q-factor control of a microcantilever by mechanical sideband excitation. *Appl. Phys. Lett.* **99**, 151904 (2011).

[Ver06] S. S. Verbridge, J. M. Parpia, R. B. Reichenbach, L. M. Bellan, and H. G. Craighead. High quality factor resonance at room temperature with nanostrings under high tensile stress. *J. Appl. Phys.* **99**, 124304 (2006).

[Ver08] S. S. Verbridge, R. Ilic, H. G. Craighead, and J. M. Parpia. Size and frequency dependent gas damping of nanomechanical resonators. *Appl. Phys. Lett.* **93**, 013101 (2008).

[Vig06] J. F. Vignola, J. A. Judge, J. Jarzynski, M. Zalalutdinov, B. H. Houston, and J. W. Baldwin. Effect of viscous loss on mechanical resonators designed for mass detection. *Appl. Phys. Lett.* **88**, 041921 (2006).

[Wes10] H. J. R. Westra, M. Poot, H. S. J. van der Zant, and W. J. Venstra. Nonlinear Modal Interactions in Clamped-Clamped Mechanical Resonators. *Phys. Rev. Lett.* **105**, 117205 (2010).

[WR08] I. Wilson-Rae. Intrinsic dissipation in nanomechanical resonators due to phonon tunneling. *Phys. Rev. B* **77**, 245418 (2008).

[WR11] I. Wilson-Rae, R. A. Barton, S. S. Verbridge, D. R. Southworth, B. Ilic, H. G. Craighead, and J. M. Parpia. High-Q Nanomechanics via Destructive Interference of Elastic Waves. *Phys. Rev. Lett.* **106**, 047205 (2011).

[WR12] I. Wilson-Rae. Private communication (2012).

[Yam94] K. Yamanaka, H. Ogiso, and O. Kolosov. Ultrasonic force microscopy for nanometer resolution subsurface imaging. *Appl. Phys. Lett.* **64**, 178 (1994).

[Yu12] P.-L. Yu, T. P. Purdy, and C. A. Regal. Control of Material Damping in High-Q Membrane Microresonators. *Phys. Rev. Lett.* **108**, 083603 (2012).

[Zen38] C. Zener. Internal Friction in Solids II. General Theory of Thermoelastic Internal Friction. *Phys. Rev.* **53**, 90 (1938).

[Zha07] W. Zhang, A. Potts, D. Bagnall, and B. Davidson. High-resolution electron beam lithography for the fabrication of high-density dielectric metamaterials. *Thin Solid Films* **515**, 3714 (2007).

# List of Publications

- Thomas Faust, Johannes Rieger, Maximilian J. Seitner, Peter Krenn, Jörg P. Kotthaus, and Eva M. Weig. Nonadiabatic Dynamics of Two Strongly Coupled Nanomechanical Resonator Modes. *Phys. Rev. Lett.* **109**, 037205 (2012).

- Johannes Rieger, Thomas Faust, Maximilian J. Seitner, Jörg P. Kotthaus, and Eva M. Weig. Frequency and Q factor control of nanomechanical resonators. *Appl. Phys. Lett.* **101**, 103110 (2012).

- Thomas Faust, Johannes Rieger, Maximilian J. Seitner, Jörg P. Kotthaus, Eva M. Weig. Coherent control of a nanomechanical two-level system. *arXiv*:1212.3172 [cond-mat.mes-hall] (2012) and Nat Phys in press.

- Johannes Rieger, Andreas Isacsson, Maximilian J. Seitner, Jörg P. Kotthaus, and Eva M. Weig. Nanoscale acoustic impedance mismatch imaging with a mechanical point contact. *In preparation.*

# Vielen Dank

Es folgt nun eine Auflistung großartiger Leute, die zum Gelingen dieser Arbeit beigetragen haben. Es werden typischerweise zuerst deren Namen genannt, gefolgt von einer kurzen Begründung der Großartigkeit der jeweiligen Person. Dies ist nicht nur üblich, sondern auch gut so.

Jörg Kotthaus danke ich für die Möglichkeit, an seinem Lehrstuhl meine Doktorarbeit anzufertigen, an dem er durch seine unnachahmliche Art für großartige Stimmung sorgt(e). Er war während der gesamten Zeit ein hervorragender Betreuer, der sich immer Zeit genommen hat Ergebnisse zu diskutieren und viele Erklärungen und Anregungen geliefert hat. Er hatte auch die von ihm so bezeichnete "Schnapsidee" mit dem AFM die Nanomechanik zu malträtieren. Danke dafür. Ich wünsche ihm außerdem viel Spaß in seinem wohlverdienten "Ruhestand".

Auch Eva Weig möchte ich für die Betreuung während der letzten Jahre danken. Ich war in ihrem Nanophysik-Seminar, habe bei ihr Diplomarbeit und Doktorarbeit gemacht. Dabei habe ich von ihr extrem viel gelernt. Allein wenn ich zum Beispiel meinen ersten Seminarvortrag mit meinem Abschlussvortrag vergleiche kann ich eine gewisse Lernkurve erkennen... Eva konnte mir bei Problemen aller Art immer weiterhelfen und ich glaube in der Nanomechanik-Gruppe sind sich alle einig, dass sie eine großartige Gruppenleiterin war. Viel Spaß und Erfolg in Konstanz.

I would like to thank Andreas Isacsson for his calculations and modeling. We had great fun when he was visiting and when we went to Gothenburg. Gunnar coined the term Brofessor...

I would also like to thank Ignacio Wilson-Rae for great discussions.

Thomas Faust danke ich für die großartige Zusammenarbeit. Ohne die Mikrowellendetektion wäre es wohl schwierig geworden. Auch ansonsten hat er mir viel geholfen. Oftmals haben wir außerdem unsere Zusammenarbeit auch außerhalb der Uni überaus erfolgreich betrieben ☺

Meinem Masterstudenten Max Seitner danke ich ebenfalls für die Zusammenarbeit und vor allem für die vielen Weltklasse-Proben (bzw. Champions League-Proben). Auch ihm wünsche ich viel Spaß in Konstanz.

Stephan Manus danke ich für die Konstruktion von Verstärkern in allen Frequenzbereichen. Ohne sein elektrotechnisches know-how wäre der Lehrstuhl diesbezüglich verloren. Ein Besuch bei ihm ist immer lustig. Manchmal dauert's dann auch etwas länger...

Peter Krenn danke ich ebenfalls für die Mikrowellendetektion und das Rezept zur Herstellung der Saiten, das ich erfolgreich an Max Seitner weitergeben konnte. Wir hatten eine Mordsgaudi im Labor und die Musikauswahl war immer hervorragend.

Bei Max Mühlbacher möchte ich mich für den Aufbau des Michelson-Interferometers bedanken, bei Thomas Bachelorstudenten Todor Krastev und Sophie Ratcliffe für die Entwicklung von Mikrowellen-Kavitäten.

Philipp Altpeter und Reinhold Rath für den exzellenten Betrieb des Reinraums, den Pumpstand und noch wichtiger: Notfallkaffee, wenn die Maschine in der Küche kaputt war.

Wir machen Nanomechanik. Anton Heindl und Wolfgang Kurpass halfen immer gerne und kompetent bei der Makromechanik.

Martina Jüttner und Bert Lorenz wissen bei bürokratischen Problemen stets zu helfen, auch wenn ein solches Problem klar selbst verschuldet ist. Danke dafür.

Man sollte auch Onur Basarir mal danken.

Eric Hoffmann von dem selbst der Quirin in mathematica noch viel lernen könnte.

Dank meinen Zimmerkollegen Enrico Schubert, Jens Repp, Thomas Faust und Matthias Hofmann war bei uns im Büro immer gute Stimmung. Es wurde gelacht und gesungen.

Danke auch an verflossene Zimmerkollegen:

- Quirin Unterreithmeier danke ich für den LabScript sequencer. Und für Schultern auf die couch!
- Der Seehausener Xaver Vögele hat alles immer so wunderbar kommentiert.
- Philipp Paulitschke, der aus allem einen Wettbewerb gemacht hat. Kannst du das auf dem Fuß balancieren...

Den lieben Kollegen ein Dank. Damit sich keiner benachteiligt fühlt in zufälliger Reihenfolge. Ich hoffe inständig, ich vergesse niemand:

- Sebastian Stapfner, weil er so ausgeglichen und immer hiflsbereit ist.
- Jan Glückert, weil er unbestritten weltweit der lustigste Münchner ist.
- Danke ich Florian Seilmeier? Nein! Doch!
- Andre Neumann, weil.
- Matthias Hauck geh heast.
- Matthias Hofmann meinem schweigsam groovenden Gegenüber und Desktophintergrund.
- Jens Repp die alte Stimmungskanone.
- Gunnar - Bocuse - Petersen.
- Enrico Schubert. It's nice to meet you! Gimme your...

- Thomas Faust - Wacken!!! wenigstens hört einer metal.
- Florian Flof Forster. Is schön hier in Bayern geh!
- Daniel Harbusch der beste und schwärzeste Kaffeetrinker.
- Sergey Platonov.
- Nooshin Yvarinia.
- Daniela Taubert die nerdigste von uns allen. Nerdig ist ein Kompliment.
- Georg Schinner - Whoarrr! Maschin!
- Matthias Fiebig. Ach, ja mei, geh, so is' es halt.
- Der Nasenmann.
- Xaver Vögele für's Chopin anstellen beim Raufen mit dem Nasenmann.

Meinen Mitbewohnern Darren und Cornelius danke ich für die beste Nerd-WG. Darren, danke für's Korrekturlesen diverser Manuskripte. Cornelius danke für theoretische und codierte Unterstützung.

Ich danke dem gesamten Lehrstuhl für die ausgezeichnete Arbeitsatmosphäre und die gute Zusammenarbeit.